

2D Layered Heterojunctions for Photoelectrocatalysis

Mengjiao Wang*, Michal Langer, Roberto Altieri, Matteo Crisci, Silvio Osella* and Teresa Gatti*

KEYWORDS: 2D layered nanostructures, heterojunctions, photoelectrocatalysis, light energy conversion

ABSTRACT: Two-dimensional (2D) layered nanomaterials heterostructures, arising from the combination of 2D materials with other low-dimensional species, feature large surface area to volume ratio, which provides a high density of active sites for catalytic applications and in particular for (photo)electrocatalysis (PEC). Meanwhile, their unique electronic band structure and high electrical conductivity enable efficient charge transfer (CT) between the active material and the substrate, which is essential for catalytic activity. In recent years, researchers have demonstrated the potential of a range of 2D material interfaces, such as graphene, graphitic carbon nitride (g-C₃N₄), metal chalcogenides (MCs), and MXenes, for (photo)electrocatalytic applications. For instance, MCs such as MoS₂ and WS₂ have shown excellent catalytic activity for hydrogen evolution, while graphene and MXenes have been used for the reduction of carbon dioxide to higher value chemicals. However, despite their great potential, there are still major challenges that need to be addressed in order to fully realize the potential of 2D materials for PEC. For example, their stability under harsh reaction conditions, as well as their scalability for large-scale production are important factors to be considered. Generating heterojunctions (HJs) by combining 2D layered structures with other nanomaterials is a promising method to improve the photoelectrocatalytic properties of the former. In this review, we inspect thoroughly the recent literature, to demonstrate the significant potential that arises from utilizing 2D layered heterostructures in PEC processes across a broad spectrum of applications, from energy conversion and storage to environmental remediation. With the ongoing research and development, it is likely that the potential of these materials will be fully expressed in the near future.

1. Introduction

Electrocatalysis constitutes one of the most important branches in the modern chemical industry. It enables chemical reactions that generate few by-products and require low amounts of starting materials, leading to cleaner and more sustainable chemical processes. In this field, electric power is converted into an energy source to trigger a variety of chemical reactions, such as water splitting,¹ nitrogen reduction,² CO₂ reduction,³ treatment of pollutants⁴ and much more. However, to replace the traditional thermal catalysis with an eco-friendly electrocatalysis, the efficiency and the cost of the whole electrocatalytic system still remain a problem. For example, in the field of H₂ production, the H₂ generated through water splitting accounts only ~ 3.9% of the total output due to its double cost compared to the thermal catalysis method, which still relies on fossil fuels as the primary H₂ source.⁵ There are two main strategies to decrease the cost and improve the catalytic system: one is to make use of alternative clean and cheap energy sources to promote the chemical reactions, and another one is to develop more efficient catalysts at lower costs. In this context, the introduction of light as an energy source and the development of cheap catalysts have become interesting directions. After Fujishima and Honda firstly split water by resorting to a combination of electricity and solar light, scientists found that specific kinds of electrocatalysts are able to convert photo energy into the energy for chemical reactions.⁶ While relying entirely on solar energy for the catalytic reactions represents the most eco-friendly approach and eliminates the need for electricity consumption, the current efficiency of pure photocatalysis falls short of meeting the practical application requirements. Therefore, photoelectrocatalysis (PEC) turns out as a more versatile strategy that combines a clean energy source while also ensuring high reaction efficiency.

A proper photoelectrocatalyst is an essential component in a PEC reaction, as it should be able to absorb light and use the energy from photons to drive the chemical reaction, while also serving as a classical catalyst to increase the reaction speed. As shown in Figure 1, in PEC, a photoelectrode is used to generate electron-hole pairs upon illumination. Specifically, when photons with sufficient energy are absorbed by the photoelectrocatalyst on a photocathode, they can excite electrons inside the catalyst and drive specific reduction reactions with the excited electrons. Similarly, a photoanode is able to accumulate photo-generated holes and catalyze oxidation reactions. Based on the above mechanism, the choice of photoelectrocatalyst is crucial in determining the efficiency and selectivity of the PEC reaction. Ideally, a photoelectrocatalyst requires the following criteria: i) a suitable bandgap (smaller than the energy of the incident light) to have a high absorption coefficient for the relevant wavelengths of light; ii) a suitable band alignment to ensure the PEC, meaning that the conduction band (CB) should be more negative than the reduction potential of the desired reaction, while the valence band should be more positive than the oxidation potential of the reaction. This ensures that the generated electrons and holes have enough energy to participate in the specific reaction; iii) stability under the reaction conditions, including light exposure, strong pH, and high bias. Stability is critical to ensure the material maintains its photoactivity and catalytic activity over time; iv) high mobility of charge carriers to facilitate a charge transfer (CT) to the surface of the catalyst and improve the catalytic activity.

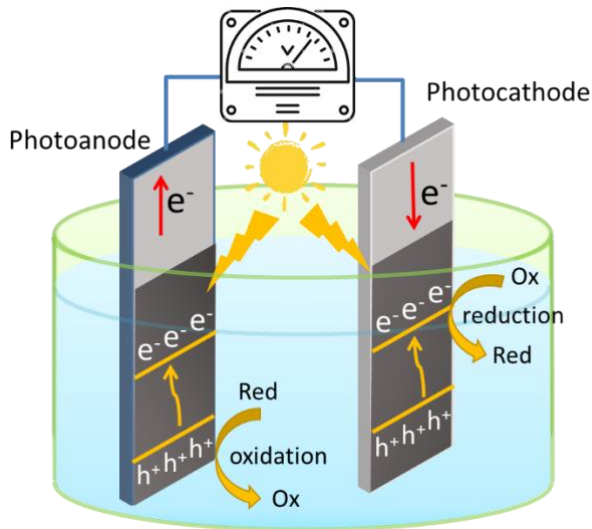


Figure 1. General mechanism of PEC reactions.

Two-dimensional (2D) materials are characterized by strong in-plane covalent bonds and weak van der Waals (vdWs) interactions between layers, resulting in atomically thin materials with unique electric and optical properties. The most well-known 2D materials include graphene, graphitic carbon nitride (g-C₃N₄), metal chalcogenides (MCs), layered double hydroxides (LDHs), MXenes, bismuth oxyhalides (BiOX, X=Cl, Br or I), hexagonal boron nitride (h-BN), Pd₃(PS₄)₂, transition metal oxides, 2D metal organic frameworks (MOFs), Xenes, metal phosphorous trichalcogenides (MPCh₃), and other materials with 2D structure on atomic level (Figure 2).⁷⁻¹² 2D materials have been extensively studied in PEC, where they

serve various roles, including functioning as photoelectrocatalysts, co-catalysts for bandgap tuning, CT mediators or supporting matrices for catalysts.¹³⁻¹⁶ Usually, 2D materials are mainly selected for PEC due to the following properties:

- i) Large surface area. As a catalyst, high surface area of 2D materials can increase the density of active sites (surface defects, unsaturated atoms, and/or active edges et al.) and improve the efficiency of the catalytic reaction. As a supporting matrix, the large surface area enables a wide distribution of the real catalysts. Meanwhile, interior atoms could be brought closer to the surface in thinner atomic layers, thereby facilitating the contact between the catalysts and reactants.
- ii) Strong interaction with light. Due to their thin nature, 2D materials can strongly interact with light, leading to efficient generation of charge carriers under illumination.
- iii) Good CT properties. 2D materials have excellent CT properties, which allow for efficient transport of charge carriers to and from the catalyst. This can improve the overall efficiency of the photoelectrocatalytic reaction.
- iv) Tunable properties. The properties of 2D materials can be tuned by adjusting their composition, thickness, and surface chemistry. This allows for precise control over their electronic and optical properties, which can be optimized for specific applications.
- v) Chemical stability. Many materials are still chemically stable after nanosized into 2D layered structures, even under harsh reaction conditions like high voltage, strong irradiation, and extreme pH. This can improve the stability and longevity of the photoelectrocatalyst.

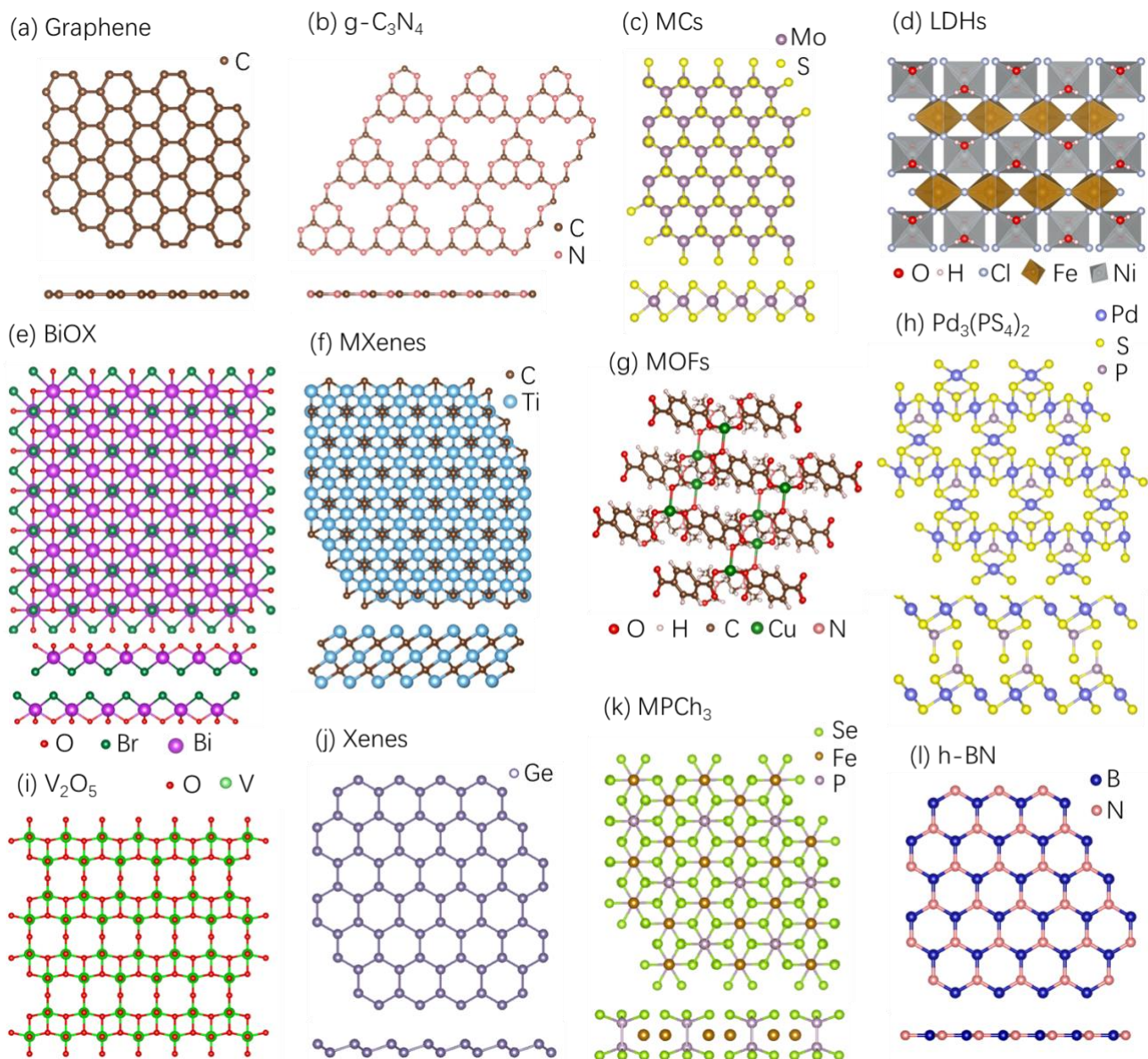


Figure 2. For each group of 2D layered materials, the structures of a representative material are shown. (a) Graphene. (b) g-C₃N₄. (c) MCs, with MoS₂ as an example. (d) LDHs, with NiFe-LDH as an example. (e) BiOX, with BiOBr as an example. (f) MXenes, with Ti₃C₂ as an example. (g) MOFs, with Cu(II) catena-((μ₄-terephthalato)-(N,N-dimethylformamide)) as an example. (h) Pd₃(PS₄)₂. (i) V₂O₅. (j) Xenes, with germanene as an example. (k) MPCh₃, with FePSe₃ as an example. (l) h-BN.

Based on this background knowledge, this review discusses up to date 2D material heterojunctions (HJs) applied in PEC. The content focuses on the introduction of different HJs based on 2D materials (Section 2). Then the methods of synthesis of 2D HJs are introduced in Section 3, the computational methods describing (photo)electrocatalysis in Section 4 and the applications of 2D HJs in PEC are summarized in Section 5, including water splitting, organic degradation, N₂ reduction reaction, CO₂ reduction reaction, antimicrobial reaction, metal ion detoxification reaction and other new reactions under PEC conditions. Finally, we conclude and provide a prospective on the potential development of 2D material HJs for PEC in the near future.

2. Heterojunctions based on 2D materials

HJs with 2D materials are interfaces between 2D materials and other nanomaterials. On one side, the large surface area of 2D materials provides enough space to combine with other nanomaterials, and the strong interaction between 2D materials and other materials can lead to enhanced charge transfer, which can be exploited for PEC. On the other side, the band alignment and bandgap of the HJs can be tuned by the 2D compounds. In fact, the 2D semiconductors HJs can interact with the surface of other components and modify the energy levels. This interaction can lead to changes in the bandgap of both the components, which affects the optical and electronic properties of the whole HJs. For example, after the introduction of MoS₂, there is a red shift in the absorption band edge of SnO₂ from 380 nm to 500 nm, indicating an enhancement in light response; the peak intensity of the PL decreases as well, showing that the

electron and hole are effectively separated (Figure 3a and 3b).¹⁷ Combining the granular SnO₂ with MoS₂ can not only expand the specific surface area of the composite and increase the surface adsorption sites of the reagents, but also allow for full

use of the optical performance of 2D MoS₂ to increase the light conversion efficiency, which is proved by the increased photocurrent of a MoS₂/SnO₂ HJ compared to pure SnO₂ (Figure 3c).

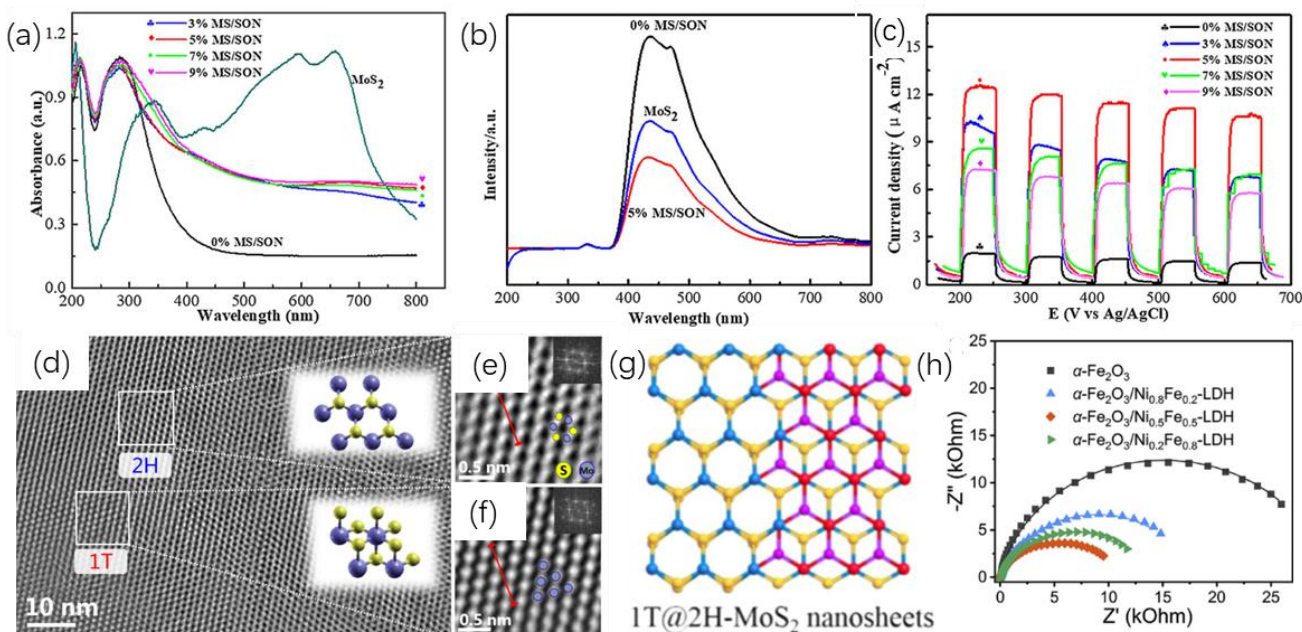


Figure 3. (a) UV-vis absorption spectra of MoS₂/SnO₂ composites with different MoS₂ weight ratios. (b) PL spectra of 0.5 % MoS₂/SnO₂ and pure MoS₂. (c) Transient photocurrent density versus time of MoS₂/SnO₂ composites in CO₂ atmosphere.¹⁷ © 2019 Wiley-VCH Verlag GmbH & Co.KGaA, Weinheim. (d) High-resolution transmission electron microscopy (HRTEM) image of the lateral HJ of MoS₂. Inset: Schematic structures of the unit cells of 1T and 2H phase. (e, f) Two filtered images of the region enclosed by the white square of (d) to show the reversed contrast. (g) Schematic of the top view of 1T/2H MoS₂ HJ.¹⁸ © 2016 American Chemical Society. (h) Nyquist plots of electrochemical impedance spectroscopy measured under AM 1.5G (100 mW/cm²) illumination.¹⁹ © 2018 Elsevier B.V.

The following 2D materials have been studied to construct the HJs for PEC: graphene, g-C₃N₄, metal chalcogenides (MCs), layered double hydroxides (LDHs), MXenes, bismuth oxyhalides and 2D MOF material. Novel 2D materials such as h-BN, Xenes, Pd₃(PS₄)₂ and MPCh₃ have been reported as promising photoelectrocatalysts, but the HJs combined with them have not been reported yet.

Graphene is an isolated 2D material consisting of a single layer of carbon atoms arranged in a hexagonal pattern, forming a honeycomb lattice (Figure 2a). It was first exfoliated in 2004, since when a plenty of applications have been discovered on 2D layered graphene.²⁰ This unique arrangement allows the electrons in graphene to move freely across its surface, giving it an exceptional electrical conductivity. In the field of PEC, graphene oxide is commonly used as well because the functional groups enhance dispersibility in solvents like water, allowing for easier integration into various matrices or coatings. For graphene oxide (GO), the introduced oxygen-containing groups make it insulate, while reduced graphene oxide (rGO) is more frequently used because the reduction of functional groups can recover the electrical conductivity. Therefore, compared with graphene, rGO are promising candidates to function as co-catalyst together with other photoelectrocatalysts for enhancing the charge separation and charge transfer.

G-C₃N₄ is a semiconducting material with a unique 2D layered structure consisting of nitrogen-containing aromatic rings, which is similar to graphene (Figure 2b). The electronic properties of g-C₃N₄ depend on its composition and structure,

which influence its band structure and the distribution of electronic states. g-C₃N₄ is classified as an n-type semiconductor because it has excess electrons as majority charge carriers, which can contribute to electrical conductivity. Apart from its unique electrical property, g-C₃N₄ exhibits good stability, unique electronic property, strong light absorption and photocatalytic activity, which makes it a promising material for applications in PEC. Except g-C₃N₄, g-C₃N₅ is used as photoelectrocatalyst as well. Studies show that g-C₃N₅ with extended conjugation via the introduction of extra nitrogen into the triazine units possesses higher thermodynamic stability, better electronic properties, and narrower band gap (2.2 eV) compared with g-C₃N₄ (2.7 eV).²¹

2D MCs are a vast class of interesting and novel material. The most popular 2D materials in this group are the transition metal dichalcogenides (TMDCs), which are denoted as MX₂ (M: metals; X: S, Se, Te), and with a general layered structure of stacked X-M-X layers (Figure 2c). Some examples are MoS₂,²² WS₂,²³ and MoSe₂²⁴ that are semiconductors in their most stable thermodynamic phase, while other TMDCs present semi-metallic (WTe₂, VS₂) or metallic properties instead (TaS₂, NbS₂).²⁵ Naturally, only the semiconducting materials have been studied for PEC applications and therefore we will take a closer look at the state-of-the-art of mainly sulfides and selenides of Mo and W. Specifically, there are two different phases of MoS₂: 1T-MoS₂ and 2H-MoS₂. 1T-MoS₂ has been synthesized by converting 2H-MoS₂.¹⁸ One notable distinction is its metallic behavior, meaning it can conduct electricity,

while the 2H- phase is typically semiconducting. This metallic nature of 1T-MoS₂ makes it particularly interesting as a charge separator and mediator in the HJ photocatalysts. For instance, in the 2H/1T HJ, the electrical coupling and synergistic effect between 2H and 1T phases can greatly facilitate the efficient electron transfer from the active sites of MoS₂, which significantly improves the HJ photocatalytic performance (Figure 3d-g).

LDHs are a class of inorganic compounds with a layered structure that consists of positively charged metal hydroxide layers and exchangeable anions between these layers. The LDH structure consists of infinite sheets with brucite-like layers with interlamellar ions (Figure 2d). In brucite-like layer, the metal hydroxide layers are composed of divalent or trivalent metal cations and OH⁻ species, where metal cations in the sheets are present at the centers of the edge-sharing octahedra constructed by OH⁻ species. There are different kinds of metal cation combinations in the structures used for PEC, such as Co/Mn²⁶, Ni/Mn²⁷, Zn/Cr²⁸, Ni/Co²⁹, Co/Fe³⁰, Co/V³¹, Cu/Ti³⁰ and Ni/Fe^{19,32} et al. The interlayer anions are typically negatively charged and can be mono- or polyatomic, such as CH₃COO⁻, Cl⁻, CO₃²⁻, NO₃⁻ and SO₄²⁻. These anions are held in place by electrostatic forces and hydrogen bonding with the metal hydroxide layers. The layers of LDHs are generally held together by weak vdWs forces, making them suitable for intercalation. As a result, they are employed as co-catalysts to enhance PEC efficiency. For example, by tuning the Ni/Fe molar ratio to 1:1, the α -Fe₂O₃/NiFe-LDH composite photoanode is able to obtain an optimized photocurrent of almost 150 μ A/cm², which is higher than α -Fe₂O₃/NiFe-LDH photoanode with other Ni/Fe ratios and ~3 times higher than pristine α -Fe₂O₃ as well.¹⁹ As illustrated in Figure 3h, the α -Fe₂O₃/Ni_{0.5}Fe_{0.5}-LDH photoanode shows the smallest electron transfer resistance (10.6 k Ω cm²) among these four samples. This reveals the fast CT kinetics that occur in the system.

As a series of 2D layered inorganic semiconductor materials, bismuth oxyhalides (BiOX, X = Cl, Br, and I) have received great research interest in various photo(electro)catalytic applications, due to their suitable band gaps, chemical stability, absence of toxicity, and corrosion resistance. Among the BiOX catalysts (Figure 2e), BiOI is the most efficient visible light harvesting photocatalyst because of its narrow bandgap (1.7 eV).³³ However, the pure BiOI is not efficient enough for PEC, thus it is commonly used as a component in hybrid photoelectrocatalysts. For instance, Pt/BiOI has been reported as good photoelectrocatalysts for various reactions.³⁴

2D MXenes are a family of 2D transition metal carbides, nitrides, and carbonitrides that have attracted significant attention in the field of PEC.³⁵ MXenes have a layered structure consisting of transition metal atoms sandwiched between two or more layers of carbon or nitrogen, resulting in a high surface area and high electrical conductivity (Figure 2f). However, the metallic nature of most kinds of MXenes do not make them capable of having an optical response ability, which greatly hinders their application in PEC as a pure photoelectrocatalyst.³³ MXenes have shown promising potential as a component for HJs due to their nature as a 2D material, including high surface area, tunable electronic properties, and chemical stability.

MOFs are a class of crystalline materials consisting of metal ions or clusters linked together by organic ligands (Figure 2g).³³ They have a highly ordered, porous structure with high surface

area and can be synthesized in a wide variety of structures and compositions. The combination of their tunable pore size, high surface area, and chemical functionality makes MOFs useful for a wide range of catalysis applications. Compared with three-dimensional MOFs, 2D MOFs can provide more coordinatively unsaturated metal sites, which is helpful to the mass transfer and electron transfer processes.¹¹ 2D-MOFs can be considered as having defective, exchangeable coordination positions at the metal nodes. Besides, the bandgap energy ranges from 1.94 to 2.12 eV, depending on the synthesis parameters of the samples, making them very promising candidates for different PEC reactions.

In general, the role of 2D materials in HJs can be divided into three kinds: (i) as main catalysts, (ii) as CT mediators or (iii) as supporting matrices. Usually, 2D materials always have synergistic performance instead of one simple function in PEC, for instance in the *p-n* junction formed with 2D materials, the 2D materials can perform as catalyst but also CT mediators for separating the charge carriers. Further elaboration on this is discussed in the following sections.

2.1 2D materials as main catalyst

2D materials with semiconductive property are widely used as the main catalyst providing the active sites for PEC reactions within HJs. Specifically, the 2D materials can separate the photogenerated charges and collect more charges from the electric field due to the tunable band structure, then transfer the charges to the active sites for photoelectrocatalytic reactions. MoS₂/indium tin oxide (ITO) HJ is a typical example.³⁶ During the PEC reaction, the carrier separation occurs by injecting photogenerated electrons from the CB of MoS₂ to ITO, whereas photogenerated holes in the valence band of MoS₂ cannot diffuse to ITO because of the existence of a *p*-type Schottky barrier. These holes accumulate on the surface of MoS₂ and participate in oxidation reactions. Meanwhile, the reverse transport of positive and negative charge carriers at the MoS₂/ITO interface retards the recombination of electron/hole pairs and prolongs the carrier lifetime, leading to a superior photocurrent response.

There are different types of HJs formed by involving 2D materials and, depending on the band positions of the semiconductor components, they include type I, type II, Z-scheme and S-scheme HJs (Figure 4a-d). In type I HJs, the photogenerated electrons usually transfer from the more negative CB to the less negative CB for reduction reaction, while the holes transfer from the more positive band to the less positive one for oxidation reaction, in this way separating the photogenerated charge carriers and allowing their exploitation for PEC. For example, at a BiOBr/MoS₂ HJ, the photogenerated holes and electrons from 2D BiOBr can transfer to the valence band (VB) and CB of 2D MoS₂, respectively, because of the intrinsic band structure of the two materials.³⁷ However, the original band position is not the only prerequisite to determine the CT route, as defect states or the internal electric field (IEF) can influence the CT route as well. For instance, the defects or oxygen vacancies on BiOBr can trap part of the photogenerated holes, thus only part of the holes from BiOBr can transfer to MoS₂, though the VB of MoS₂ is less positive.

In a type II HJ, the photogenerated electrons and holes will still transfer to the less negative CB and less positive VB, respectively. Different from type I HJ, the conduction band minimum and the valence band maximum are on different components in the type II HJ, resulting in a staggered band

alignment. As a 2D semiconductor with suitable band alignment, g-C₃N₄ is frequently used as one of the components to construct type II HJs with other semiconductors. The g-C₃N₄/TiO₂ HJ is a widely reported HJ used for PEC, since both components are efficient and stable photoelectrocatalysts.³⁸⁻⁴¹ g-C₃N₄ and BiOI form a Type-II HJ at which photogenerated electrons in g-C₃N₄ are transferred to BiOI, while photogenerated holes in BiOI are transferred to g-C₃N₄.⁴² Effective charge separation, synergistic trap filling leading to a lower CT resistance, and enhanced light absorption have been identified as dominant factors for the enhancement of photocurrent when compared to the pristine photoanodes. In

addition, S doped g-C₃N₄ acts as electron donor when placed in contact with samarium vanadate (SmV). This can create a type II HJ, where reduction reaction occurs at the CB of SmV, while oxidation reaction occurs at the valence band of S doped g-C₃N₄.⁴³ Other 2D materials with semiconducting properties such as α-Fe₂O₃/MoS₂,⁴⁴ BiOI/BiPO₄,⁴⁵ WO₃/WS₂⁴⁶ and others are reported as type II HJ for PEC as well, and are shown in Table 1.

Table 1. Photoelectrocatalytic HJs containing 2D materials.

Catalyst	Synthesis	Light source	Photocurrent	Type	application	Ref
rGO/g-C₃N₄/BiVO	Hydrothermal	500 W halogen lamp, 100 mW.cm ⁻²	14.44 mA/cm ² at 1.0 V vs Ag/AgCl	II	HER	47
rGO/AgCl	Ultra-sonication, hydrothermal	300 W Xenon lamp (λ ≥ 400 nm)	2.5 μA /cm ²	/	Organic degradation	48
rGO/CeO₂/TiO₂	Electrochemical method	500W Xe lamp (>365 nm), 110 mW cm ⁻²	/	/	Organic degradation	49
rGO/Cu	Hummers' method, electrochemical method	Xe-arc lamp (100 mW cm ⁻²)	~14 mA/cm ² at -2.4 V vs. Ag/AgCl	/	CO ₂ reduction reaction (CO ₂ RR)	50
Pt/CdS/rGO	Solvothermal	Xe arc lamp (150 W)	~1.4 mA/cm ² at -0.3 V. SCE	/	Methanol oxidation reaction (MOR)	51
GO/In₂S₃/TiO₂	Hydrothermal, electrodeposition	300 W Xe short arc lamp, 100 mW cm ⁻²	0.45 mA/cm ² at 0.8 V vs Ag/AgCl		HER	52
GO/Ag₃PO₄/Ni	Electrochemical method reported	500W Xe lamp (>420 nm), 110 mW cm ⁻²	15 mA/cm ² at 1 V vs. SCE	/	Organic degradation	14
Nd:g-C₃N₄/BiOI	Polycondensation, hydrothermal	Air Mass, AM 1.5 G	0.03 mA/cm ² at 0.2 V vs RHE	II	HER	53
g-C₃N₄/Ag₃PO₄	Polycondensation, in situ precipitation	visible lamp, λ > 400 nm	13 μA/cm ²	II	organic degradation	54
g-C₃N₄/TiO₂	Polycondensation, sonication	AM 1.5G (100 mW cm ⁻²)	142.7 μA/cm ² at 1.23 V vs. RHE	II	OER	38
SmV/g-C₃N₄	Polycondensation, hydrothermal	400 W Xe light	~0.13 mA/cm ²	II	HER,	43
BiOI/g-C₃N₄	Hydrothermal	300 W Xenon lamp	0.1 μA/cm ²	S-scheme	Water splitting	55
BiVO₄/GQD/g-C₃N₄	Hummer's method, hydrothermal, thermal polycondensation	500 W halogen lamp	19.2 mA/cm ² at 1.0 V vs Ag/AgCl	II	HER	56

Co₃O₄/g-C₃N₄	Hydrothermal	Xenon lamp	0.01 $\mu\text{A}/\text{cm}^2$	S-scheme	Organic degradation	13
P/g-C₃N₄	chemical vapor deposition (CVD)	300 W Xenon lamp	202 $\mu\text{A}/\text{cm}^2$ at -1 V vs. Ag/AgCl	/	HER	57
g-C₃N₄/TiO₂	thermal condensation	300 W Xe lamp (200 ~800 nm)	0.63 mA/cm^2 at 0.0 V vs. Ag/AgCl	II	Organic degradation	40
CQDs/g-C₃N₄	thermal polycondensation, LPE	500W Xe lamp with a UV cut-off filter (>420 nm)	$\sim 0.025 \text{ mA}/\text{cm}^2$	/	Organic degradation	58
C/g-C₃N₄	Pyrolysis, thermal condensation	white light LED lamp (50 W)	$\sim 19 \mu\text{A cm}^{-2}$ at 1.23 V vs RHE	/	Organic degradation	59
g-C₃N₄/TiO₂	thermal condensation, wet chemical synthesis	100 mW cm^{-2} (AM 1.5 G)	72.3 $\mu\text{A}/\text{cm}^2$ at 1.23 V vs RHE	II	OER	39
g-C₃N₄/Sn₃O₄/Ni		LED		Z-scheme	Metal ions reduction	60
g-C₃N₄ /α-Fe₂O₃	Hydrothermal, thermal condensation	500W Xe lamp (>420 nm), 100 mW cm^{-2}	4.97 mA/cm^2 at 1.5 V vs. Ag/AgCl	II	Organic degradation	61
g-C₃N₅/BiOBr	Hydrothermal, thermal condensation	Xe lamp (>420 nm), 110 mW cm^{-2}	-1.2 $\mu\text{A}/\text{cm}^2$	II	N ₂ RR	21
BiVO₄/SnS₂	Hydrothermal	solar simulator, 100 mW/cm^2	0.21 mA/cm^2 at 1.23 V vs RHE	Z-scheme	HER	62
Au-WS₂	Hydrothermal	300 W Xenon lamp	23 mA/cm^2 at 1 V vs. SCE	/	Pollutant degradation	63
GaTe/ZnO	CVD	300 W Xe lamp ($\lambda > 420 \text{ nm}$), 100 mW cm^{-2}	-2.5 mA/cm^2 at -0.39 V vs RHE	II	HER	64
Ni/NiFe-LDH/Co₃O₄	hydrothermal	Xenon lamp	0.16 $\mu\text{A}/\text{cm}^2$ at 0.7 V vs. RHE	II	Organic degradation	32
α-Fe₂O₃/NiFe-LDH	Hydrothermal, electrodeposition		150 $\mu\text{A}/\text{cm}^2$ at 1.23 V vs RHE		OER	19
Ti₃C₂T_x/Bi₁₂TiO₂₀	Hydrothermal	xenon lamp	/	/	Organic degradation	65
Co-Ti₃C₂	Hydrothermal	solar simulator, 100 mW cm^{-2}	2.99 mA/cm^2 at 1.23 V vs RHE	/	OER	66
TiO₂/Ti₃CN MXene	Hydrothermal			/	CO ₂ RR	67
Pd/N-TiO₂/Ti₃C₂	Hydrothermal	300 W Xenon lamp with 200 mW/cm^2	1 mA/cm^2 at -0.7 V	/	CO ₂ RR	68
BiOBr/TiO₂	Chemical bath deposition	300W xenon lamp ($\lambda \geq 420 \text{ nm}$)	0.033 mA/cm^2	II	Organic degradation	69
WO₃/BiVO₄/NiCo₂O_x	Thermal calcination, chemical bath deposition	AM 1.5G illumination	2.85 mA/cm^2 at 0.7 V vs. RHE		OER	70

Pt-Bi₂WO₆/La₂Ti₂O₇	Hydrothermal	500 W Xenon lamp 186 mW/cm ² with a UV cut-off filter (>420 nm)	~0.5 mA/cm ² at -0.25 V vs. SCE		MOR	⁷¹
BiOI/BiPO₄	electrodeposition	xenon lamp	60 μA/cm ²	II	Organic degradation	⁴⁵
Pt/BiOI	hydrothermal	500 W Xenon lamp with a UV cut-off filter (>420 nm)	70.3 A/cm ² at -0.25 V	/	ethanol oxidation	³⁴
TiO₂/P₃HT	Hydrothermal, dip- coating	/	0.68 mA/cm ² at 1.0 V	II	Organic degradation	⁷²
Pt/La₂Ti₂O₇	Hydrothermal, photo- reduction	150 W Xe arc lamp	~0.15 mA/cm ² at -0.2 V vs. SCE	/	Methanol oxidation	⁷³
CuBDC/Cu	solvothermal method	300W Xe lamp (>420 nm), 100 mW cm ⁻²	0.6 mA/cm ² at - 0.3 V vs. RHE.	/	CO ₂ RR	¹¹

In addition to the CT-route in type II HJ, the Z-scheme PEC mechanism can be exploited for specific catalytic reactions. In a Z-scheme HJ, the less energetic electrons are transferred from the CB of one semiconductor to the valence band of another semiconductor through an intermediate redox mediator, which acts as a relay system (Figure 4c). This process results in the generation of electron-hole pairs in both semiconductors, allowing for simultaneous oxidation and reduction reactions to occur on their surfaces. However, it is not mandatory to have an intermediate in a Z-scheme HJ: direct Z-scheme catalysts have been developed as well. For example in the PEC of H₂O₂ production by MoS₂/CoMoS₄, the original band structure of MoS₂/CoMoS₄ is not able to catalyze the O₂ reduction to H₂O₂ in theory (Figure 4e).⁷⁴ This is because the E (O₂ → •O₂⁻) (-0.33 eV vs. NHE) is more negative than the CB of CoMoS₄ (-0.19 eV vs. NHE). In reality, instead of the traditional way of CT, the photogenerated charges follow the Z-scheme mechanism of charge recombination inside the HJ. Specifically, in the tight solid-solid contact HJ interface between MoS₂ and CoMoS₄, the CB of CoMoS₄ is very close to the VB of MoS₂, providing a shorter electron transfer path, and the photo-generated electrons at the CB of CoMoS₄ could quickly migrate to the VB of MoS₂ and immediately combine with the holes there. Thereby, the longevity of the remaining electron (CB, MoS₂) / hole (VB, CoMoS₄) pairs is greatly prolonged, giving the HJ excellent oxidation and reduction activity. A 2D/2D BiVO₄/SnS₂ nanocomposite can form a Z-scheme HJ by coupling both BiVO₄ and SnS₂.⁶² Inside this HJ, the electron transfer from BiVO₄ to SnS₂ is permitted, leaving holes on VB of BiVO₄ and electrons on the CB of SnS₂, making this HJ active in PEC reactions.

The formation of HJs from two different semiconductors can enhance the electron transfer capability through establishing IEF, since one material has a higher electron affinity and lower ionization energy compared to the other. This is the S-scheme HJ (Figure 4d). Typically, two types of semiconductors in the S-scheme can align the Fermi energy after contact, which results in a band bending forcing the less energetic photogenerated electron in the CB of the oxidation catalyst and

hole in the VB of reduction catalyst at the interfacial region. Different from Z-scheme HJs, in which the two materials have similar electron affinities and ionization energies, the IEF, band bending, and Coulombic attraction act as the driving forces of the charge recombination inside the S-scheme HJ. For example, the combination of 2D BiOI nanoflakes and g-C₃N₄ in a HJ forms a *p-n* junction and builds an IEF on the interface of the two materials, with more negative charges on the BiOI surface and more positive charges on the g-C₃N₄ surface (Figure 4f).⁵⁵ Under illumination, the photogenerated electrons transfer from BiOI to g-C₃N₄ under the influence of the IEF, while the photogenerated holes transfer on the opposite direction. The rapid recombination of photogenerated charges is prevented by the transfer. In this way, the accumulated electrons on g-C₃N₄ can catalyze a reduction reaction, meanwhile BiOI can provide reaction sites for an oxidation reaction.

It is worth to mention that in some S-scheme HJs, there can be several competitive CT processes and the pathway based on the S-scheme mechanism might not be dominant.⁷⁵ As shown in Figure 4g, in the MoS₂/WSe₂ HJ, photogenerated electrons and holes are formed in both MoS₂ and WSe₂ (process 1). Because of the carrier concentration gradient, an IEF forms at the interface between MoS₂ and WSe₂. This IEF accelerates the electrons to the CB of MoS₂ the hole to the VB of WSe₂ (process 2). Though the charge recombination process 3 and 4 occurs simultaneously *via* the interface transitions and inside the crystals, the time scale of process 3 is at a nanosecond (ns), which is 3 or 4 orders of magnitude slower than CT process 2. Thus, the CT is still dominant to the separation of the photoinduced charge pairs. As a result, the recombination process is suppressed by the consumption and inverse transfer of the electrons and holes, inducing a more significant photocurrent than individual MoS₂ and WSe₂. Consequently, the photocurrent of the HJ is 1.79 times larger than that of pristine MoS₂ and 1.94 times larger than that of pristine WSe₂.

Except for the intrinsic band structures of 2D semiconductors, the defect states can influence the band engineering of the HJs as well. For example, Al₂O₃ can construct a type I HJ with 2D SnS₂.⁷⁶ While the defect state is introduced into Al₂O₃, instead

of recombining with the holes inside SnS₂, the photogenerated electrons can transfer to the defect state of Al₂O₃ and move to the Pt electrode for PEC. Meanwhile, the holes on the VB of SnS₂ are free for further PEC.

Additionally, the morphology of the two nanomaterials involved in the HJ can influence the CT and the PEC efficiency. As mentioned before, 2D materials have a high surface area to provide more active sites, and thin thickness for short CT length to move to the catalytic reaction point. MoS₂/WS₂ HJs are widely used in different kinds of photoelectrocatalytic reactions. Sherrel et al. prepared 100 μm large flakes samples to enable minimization of atomic defects and nanosheets edge density, while the atomically sharp and clean interfaces between the flakes are responsible for reducing charge carrier recombination. The PEC performance turns out better than the MoS₂/WS₂ HJ with smaller flakes, which have higher density of defects.⁷⁷ Other HJs containing different 2D layered materials can also be formed, such as, g-C₃N₄/nitrogen-doped graphene/MoS₂⁷⁸, g-C₃N₄/BiOBr²¹, MoSe₂/g-C₃N₄⁷⁹, VS_x/graphene⁸⁰, etc. These HJs provide a broad optical window for effective light harvesting, short diffusion distance for excellent charge transport, as well as a large contact area for fast interfacial charge separation and PEC reactions. The measured photocurrent density of the HJs is generally enhanced compared

to the individual components, which is proof of the superior ability of HJs to generate and transfer photoexcited charge carriers.

The combination between 2D semiconductors and another metallic counterpart can benefit the charge separation as well. For instance, the Sn_xMo_{1-x}S₂/MoS₂ HJ is obtained with atomically sharp interface between the metallic Sn_xMo_{1-x}S₂ and semiconducting MoS₂.⁸¹ The electrons generated by photon energy can rapidly transfer to the mixed sulphide and then to the counter electrode, leaving a rich amount of holes for PEC oxidation reactions.

In the PEC processes, the CT pathway is usually determined by the combination of several confirmatory experiments. For example, free radical capture experiments were performed in the PEC of organic degradation by Co₃O₄/g-C₃N₄ to detect the active species, indicating that •OH and •O₂⁻ play a dominant role during the degradation reaction.¹³ Based on the analysis of band position from theoretical calculations and reaction energy of the active species free radical capture experiments, it is clear that the more energetic electrons on the CB of Co₃O₄ and holes on the VB of g-C₃N₄ participate in the formation of •OH and •O₂⁻, while the holes on Co₃O₄ and electrons on g-C₃N₄ recombine on the interface of the HJ.

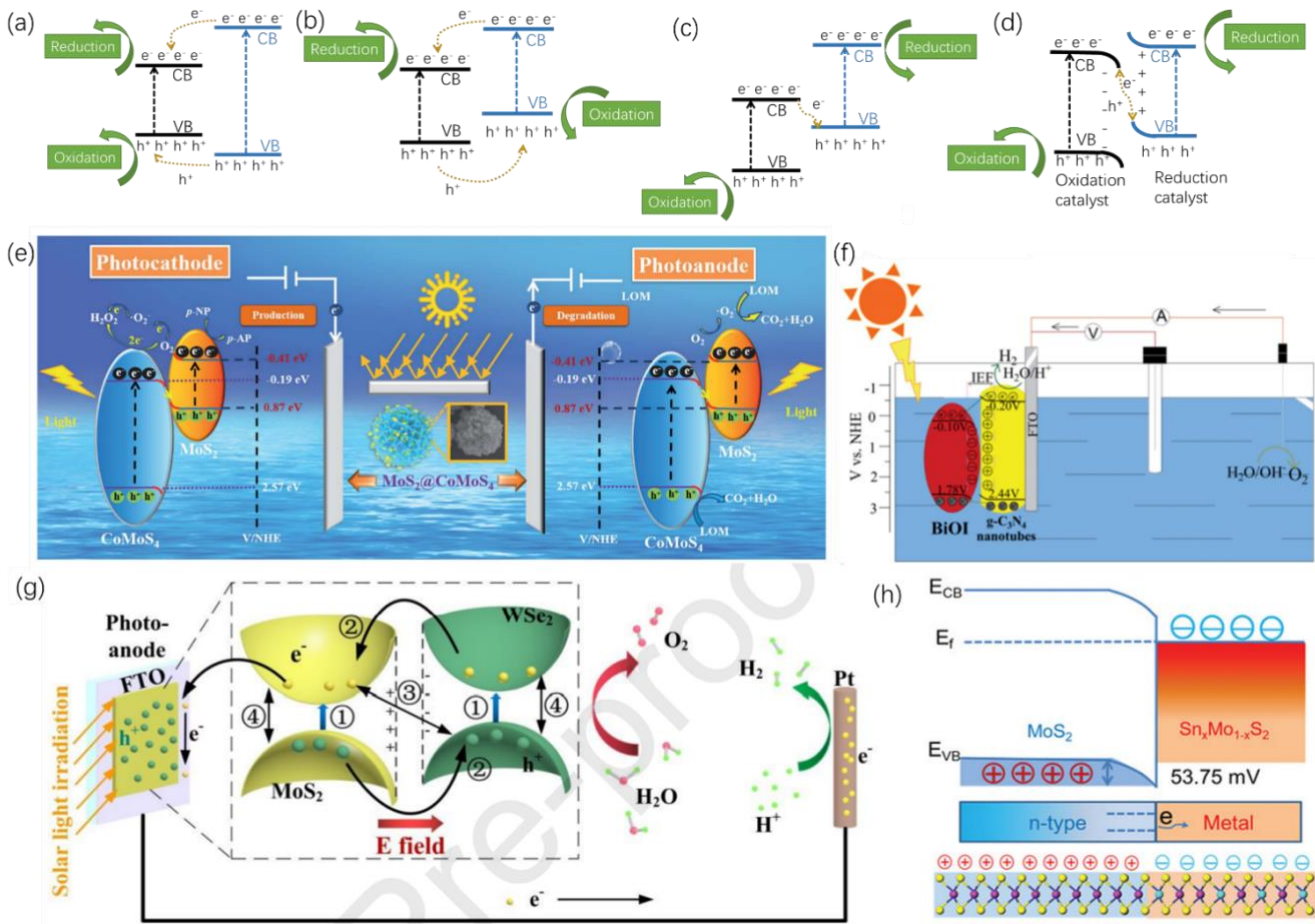


Figure 4. Scheme of (a) type I HJ, (b) type II HJ, (c) Z-scheme HJ and (d) S-scheme HJ. (e) Possible PEC mechanism of MoS₂/CoMoS₄.⁷⁴ © the Royal Society of Chemistry 2020. (f) Mechanism of BiOI/g-C₃N₄ over photoelectrode under light irradiation.⁵⁵ © 2022 Elsevier B.V. (g) Schematic diagram of the charge carrier separation and transfer processes of MoS₂/WSe₂ photoanode in an electrolyte under light illumination.⁷⁵ © 2019 Elsevier B.V. (h) Schematic of the band profile for Sn_xMo_{1-x}S₂/MoS₂ heterostructure according to Kelvin probe force microscopy (KPFM) characterization. Bottom: schematic of the

heterostructure's cross section. Purple, cyan, and yellow balls represent Mo, Sn, and S atoms, respectively. Red circles with plus symbol and blue circles with minus symbol represent holes and electrons, respectively.⁸¹ © 2020 Wiley-VCH GmbH.

2.2 2D materials as charge transfer mediators

As CT mediators, 2D materials do not behave as the direct catalyst in a HJ, but they act as support for charge separation and transfer. Charge transport must take place between the components of the HJs during PEC. By adding a 2D material, the CT pathway can be completely changed. As discussed in Session 2.1.1, graphene and its derivatives are widely used as CT mediators because of their high electrical conductivity. Therefore, they are more frequently used for CT rather than for charge generation, and other semiconductors are usually needed in the HJ to absorb and convert the light energy. For example, Cu₂O is largely used for PEC of CO₂RR.⁸² With the addition of 2D graphene, PEC measurements demonstrated better performance, which is rooted in a suppressed charge carrier recombination. RGO can combine with other semiconductors in forming HJ such as BiVO₄/g-C₃N₄ to fabricate more complex and efficient photoelectrocatalyst.^{47,56} Samsudin et al. loaded rGO on BiVO₄/g-C₃N₄ to fabricate a new HJ. Upon its integration in the HJ, rGO has become an intermediate material for charge migration in the HJ (Figure 5a). The electrons at the CB of g-C₃N₄ smoothly migrate towards the CB of BiVO₄

through rGO due to the electrostatic attraction between g-C₃N₄ and rGO. In addition, the observed smooth electron migration can be attributed to the lower Fermi level of rGO, which is higher in energy (-0.08 eV vs. NHE) compared to the calculated CB of g-C₃N₄ (-1.30 eV vs. NHE). Thereby, the photo-induced charge carriers generated via the rGO/g-C₃N₄/BiVO₄ photocatalyst will flow to the counter electrode via an external circuit for PEC. Similarly, the incorporation of 2D rGO within semiconducting nanoparticles such as AgCl and CdS⁵¹, plays a vital role in charge separation⁴⁸. In these combinations, rGO can attract and transfer one type of charge carriers, leaving the other type on the semiconductors, thus enhancing the charge separation and transfer. For example, the photo-excited electrons from AgCl quantum dots are transferred to the surface of rGO thanks to the favourable energy level between the CB of AgCl and the work function of rGO, and then flowed to the collecting electrodes, leaving the holes on the VB of AgCl QDs, suitable for oxidation reaction. rGO is used in the CeO₂-TiO₂ system for decreasing the recombination rate of charge pairs.⁴⁹ It was found that an optimized amount of rGO results in an improvement of degradation efficiency, while an excess loading reduces the PEC efficiency, as a too large amount of rGO coating blocks light absorption from the binary CeO₂-TiO₂ HJ.

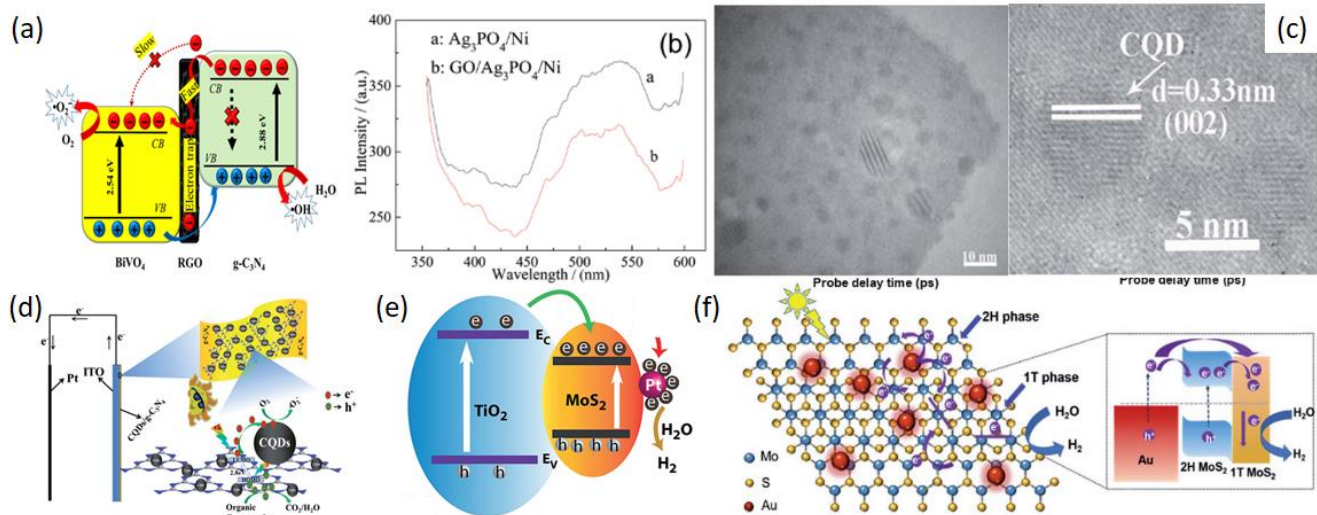


Figure 5. (a) Possible schematic illustration of CT inside the g-C₃N₄/BiVO₄ decorated with rGO.⁴⁷ © 2020 Elsevier B.V. (b) Room-temperature PL spectra of Ag₃PO₄/Ni and GO/Ag₃PO₄/Ni thin films.¹⁴ © The Royal Society of Chemistry and the Centre National de la Recherche Scientifique 2020. (c) Transmission electron microscopy (TEM) images of the CQDs/g-C₃N₄. (d) Mechanism of the photoelectrocatalytic process for the CQDs/g-C₃N₄ under visible light irradiation.⁵⁸ This article is licensed under a Creative Commons Attribution-NonCommercial 3.0 Unported Licence. (e) Schematic illustration of CT at the multiple interfaces and the mechanism of enhanced visible light PEC activity of Pt NPs decorated on TiO₂/MoS₂.⁸³ © The Royal Society of Chemistry 2017. (f) A schematic illustration of PEC hydrogen evolution over the 1T-2H MoS₂/Au HJ.⁸⁴ The Royal Society of Chemistry 2019.

Moreover, addition of rGO sheets can inhibit the recombination of charge carriers in a HJ such as Ag₃PO₄/Ni, due to the excellent conductivity of rGO.¹⁴ As shown in Figure 5b, the pure Ag₃PO₄/Ni has a broad optically active recombination at 475–510 nm by the photogenerated holes with electrons around surface oxygen vacancies. While the quenching of the PL intensity of the rGO/Ag₃PO₄/Ni composite film indicates that the optically active recombination of charge carriers is suppressed by rGO. Interfacial charges can be transferred from the CB of Ag₃PO₄ to rGO, thus effectively separating photogenerated charge carriers. This helps to prolong the

charge carrier lifetime and should lead to improved PEC activity. This better PEC performance is proved by faster rhodamine B (RhB) degradation than in the pristine Ag₃PO₄/Ni. Alternatives of rGO such as g-C₃N₄ work with the same mechanism in conjunction with Ag₃PO₄.

2D MXenes are another large group of CT-mediators researched in recent years. For example, the *in situ*-growth TiO₂/Ti₃CN HJ demonstrates excellent light absorption abilities, possess large specific surface area and contains Ti³⁺ species and oxygen vacancies, which are beneficial for the

generation and transport of electron/hole pairs.³⁵ In $\text{Ti}_3\text{C}_2\text{T}_x/\text{Bi}_{12}\text{TiO}_{20}$ HJ, it was proved that $\text{Ti}_3\text{C}_2\text{T}_x$, as a useful co-catalyst, creates an IEF at the contact interface with $\text{Bi}_{12}\text{TiO}_{20}$ and also an external one, which are both responsible for the enhanced PEC performance.⁶⁵

MoS_2 can perform as a CT-mediator as well. In $\text{MoS}_2/\text{La}_2\text{Zr}_2\text{O}_7$, the 2D MoS_2 surface presents a large active area for light absorption and photoelectrons generation, while rich oxygen vacancies in $\text{La}_2\text{Zr}_2\text{O}_7$ with a stable pyrochlore structure trap photogenerated electrons from MoS_2 and make them available for PEC.⁸⁵ Besides, the $\text{MoS}_2/\text{La}_2\text{Zr}_2\text{O}_7$ HJ distributes a localized charge density in the photoelectrocatalyst, which increases the adsorption sites of the reactants. All these factors drive efficient PEC reactions. To further improve the catalytic property, HJs with vertically aligned MoS_2 could be induced. For example, Fe doped Ni_3S_2 can be loaded on the edges of the MoS_2 to build an active interface which is more favorable for adsorption and desorption of the reactants and products.⁸⁶

In some HJs, the 2D materials with semiconducting properties can act as charge generators and mediators, while the other component can attract the photogenerated charges from the 2D materials and use them for PEC. As discussed in section 2.1, g- C_3N_4 has drawn attention as a promising new layered material with a bandgap of ~ 2.7 eV. When combined with carbon quantum dots (CQDs), the contact area between g- C_3N_4 nanosheets and CQDs may be greatly increased due to the small size of the CQDs (Figure 5c).⁵⁸ Therefore, nanoscale junctions under close contact may be established. Photogenerated charges can transfer rapidly to the surface and further travel to the CQDs for PEC reactions (Figure 5d). Similarly, g- C_3N_4 can combine with other materials to form more efficient HJs such as $\text{La}_2\text{O}_3/\text{g-C}_3\text{N}_4$, $\text{CoO}/\text{g-C}_3\text{N}_4$, and $\text{La}_2\text{O}_3/\text{CoO}/\text{g-C}_3\text{N}_4$ ⁸⁷, in which g- C_3N_4 mainly absorbs photons and converts them into active charges to be transferred to the other parts of the junction for PEC.

Metal oxides like WO_3 can act as charge transport mediators.⁷⁰ For example, in the HJ $\text{WO}_3/\text{BiVO}_4$, 2D WO_3 is used as the electron transport layer, providing direct and fast electron transport pathways in the photoinduced charge transport process to suppress the back reaction.

In some situations, the 2D layered catalyst works as a charge separator and transfer mediator on one photoelectrode, while the needed charge carriers are transferred to the counter electrode for the PEC reaction. In water splitting, the catalyst actually catalyze oxygen evolution reaction (OER) directly and enhance the hydrogen evolution reaction (HER) indirectly because these two half reactions complement each other. Since the catalytic property is finally determined by detecting the production of H_2 , the HJs are classified as catalysts for HER. The $\text{NiFe-LDH}/\text{Co}_3\text{O}_4$ HJ is such a catalyst for HER, in which the active electrons are generated on the $\text{NiFe-LDH}/\text{Co}_3\text{O}_4$ photoanode and move to the counter Pt electrode for the reduction reaction.³² Another example is photoelectrocatalytic reduction of U(VI) of g- $\text{C}_3\text{N}_4/\text{Sn}_3\text{O}_4/\text{Ni}$.⁶⁰ In this system, the charge separation is guaranteed by the outside electric field and the S-scheme charge recombination pathway. Under the influence of a bias voltage, the photogenerated electrons on the CB of g- C_3N_4 transfer to the cathode, while the photogenerated electrons on the CB of Sn_3O_4 can neutralize the photogenerated holes on the VB of g- C_3N_4 and prevent the charge recombination inside the g- C_3N_4 . Besides, photoelectrocatalysts such as h- $\text{MoO}_3/1\text{T-MoS}_2$ ⁸⁸, Nd-doped g- $\text{C}_3\text{N}_4/\text{BiOI}$ ⁵³, $\text{Co}_3\text{O}_4/\text{NiMnO}_3$ ⁸⁹, $\text{TiO}_2/\text{g-C}_3\text{N}_4$ ⁴⁰ and B-phase $\text{TiO}_2/\text{MoS}_2$ ⁹⁰ are

charge generators and separators, providing active species for the corresponding PEC reactions.

The previous tremendous research work has proved the excellent property of HJs with 2D materials and other semiconductors as charge separators. Indeed, the combination between metals and 2D materials can be a promising strategy for efficient photoelectrocatalysts. It is also known that noble metals are perfect catalysts for a lot of chemical reactions, but their cost limits the application towards industrial level. To reduce the cost and ensure the quality of the catalyst at the same time, scientists attempt to combine the “best” charge carrier separator, namely 2D materials, with the “fastest” reaction active sites, namely, noble metals, for specific PEC. With this design of catalyst, the small amount of noble metal usually functions as the reaction active site, while the 2D materials are charge separators to convert light and electric energy and transfer the charge carriers to the active sites. Paul et al. introduced Pt dots to further improve the catalytic property of a n-doped $\text{MoS}_2/\text{TiO}_2$ (B-phase) HJ. Instead of being the real catalyst, the HJ works as a CT mediator to concentrate the electrons and transfer them to the Pt dots for HER (Figure 5e).⁸³ A similar strategy is applied in the 2D Au/WS_2 photoanode system, in which Au nanodots were successfully incorporated into 2D WS_2 nanosheets in order to collect active species, adsorb and catalyze toxic chemicals degradation, while WS_2 is in charge of generating charge carriers with its photoelectric property.⁶³ Hu et al. designed a $\text{La}_2\text{Ti}_2\text{O}_7/\text{Pt}$ photoanode by following this strategy of building HJs.⁷³ The 2D perovskite $\text{La}_2\text{Ti}_2\text{O}_7$ is used as light converter and support for the decoration of Pt nanoparticles, while Pt acts as active site for photoelectrocatalytic methanol oxidation. Moreover, the loading of small amount of Pt, Ag, Rh or Au on B-doped g- C_3N_4 2D layered materials can facilitate the PEC reduction reaction as well, since the noble metal behave as a fast catalytic reaction center, while the 2D layered g- C_3N_4 is in charge of electron-hole separation and migration.^{91,15} In all of these above examples for PEC, a three-electrode system and external electrochemical workstation are applied for the test, indicating that this is still in the early stages of research. To push these cheap catalysts to the real application at industrial level, an artificial photosynthetic cell is needed for the characterization of the catalysts. Xu et al. prepared $\text{Pd}/\text{N-TiO}_2/\text{Ti}_3\text{C}_2$ as photocathode, in which $\text{N-TiO}_2/\text{Ti}_3\text{C}_2$ is responsible for generating and transferring active electrons to Pd for PEC, while BiVO_4 is chosen to replace Pt as the anode in the artificial photosynthesis cell.⁶⁸ Similar examples are listed in Table 1.

The combination of 2D semiconductors and materials with metallic properties can accelerate the CT at the interface of the HJ as well. Zheng et al. synthesized a 1T-2H MoS_2/Au HJ⁸⁴. Under illumination, both the plasmonic Au and semiconducting 2H- MoS_2 act as light absorbers (Figure 5f). The hot electrons from Au with high enough energies can overcome the Schottky barrier and be injected into the 2H- MoS_2 CB. Besides, the Schottky barrier existing at the interface of Au and 2H- MoS_2 can efficiently prevent the injected hot electrons to recombine. Moreover, the intimate lateral 1T-2H MoS_2 heterostructure improves the intralayer CT from the CB of 2H MoS_2 to 1T- MoS_2 . Additionally, the metallic 1T- MoS_2 enhances the electronic conductivity as well as provides abundant catalytically active sites for PEC water splitting.

2.3. 2D materials as supporting matrix

Thanks to the large surface area, 2D materials are frequently chosen as supporting matrix for other photoelectrocatalysts. By growing smaller nanosized photoelectrocatalysts on the 2D material matrix, the aggregation of the photoelectrocatalysts is prevented and it can be more uniformly distributed than without the 2D material matrix. For instance, nanosized pure lamellar structure of nickel boron oxide (Ni-B_i) suffer from low productivity and aggregation by direct synthesis, while on graphene matrix the ultrathin 2D Ni-B_i arrays vertically aligns and thus maximizes the exposure of the active sites for PEC (Figure 6a and 6b).⁹² As shown in Figure 6c, the photocurrent density of Ni-B_i/graphene displays a distinct enhancement compared to the pristine Ni-B_i, suggesting an improved charge separation and transfer at the Ni-B_i/graphene HJ.

Peng et al. reported a novel photoelectrocatalytic system by growing carbon nitride (CN) on the surface of carbon paper under in situ crystallization by using dicyandiamide and calcination step afterwards⁵⁹. As shown in Figure 6d, the synthesized CN by dicyandiamide or melamine exhibits a vertically aligned morphology with a homogeneous layer distribution and excellent contact with the carbon paper. It is notable that electrical conductivity of both CN/C samples is improved compared to that of carbon paper, and comparable to the commercial carbon paper. The good electrical conductivities of self-standing CN/C pave the way toward their application as freestanding photoanodes in PEC.

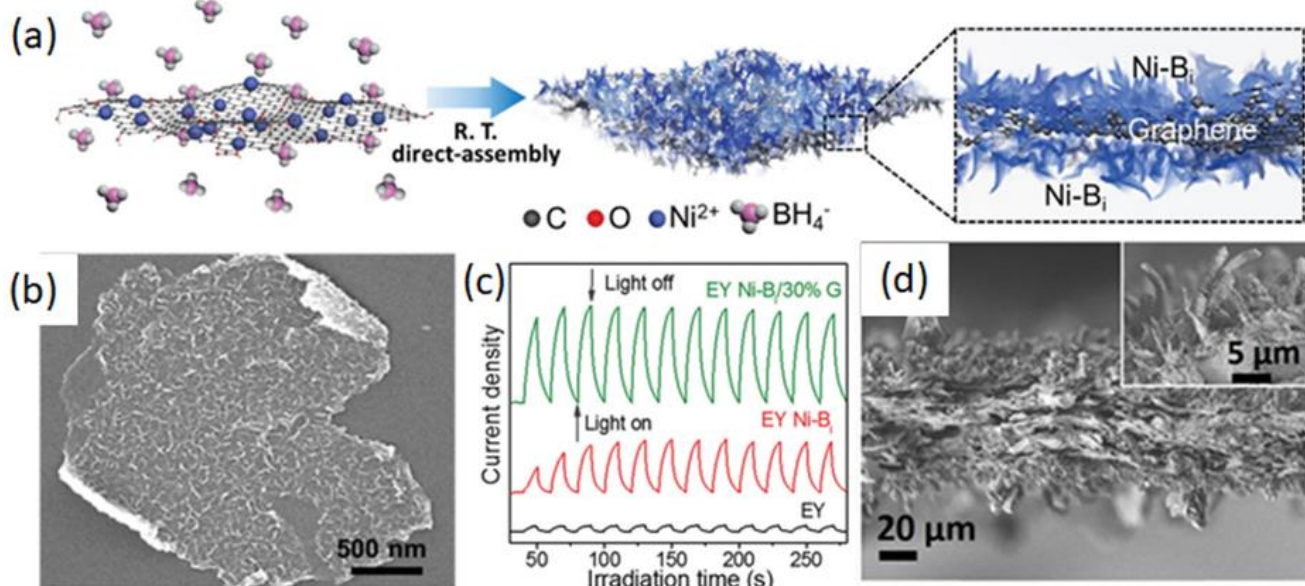


Figure 6. (a) Schematic illustration of the synthesis of the 2D-on-2D trilayered nickel boron oxide/graphene (Ni-B_i/G) sandwich heterostructure. (b) Field emission scanning electron microscopy images of Ni-B_i/G. (c) Transient photocurrent response bare EY, EY-(Ni-B_i) and EY-(Ni-B_i/G) Eosin Y is used (EY) as a photosensitizer.⁹² © The Royal Society of Chemistry 2017 (d) cross-sectional SEM images of CN/C.⁵⁹ © 2019, American Chemical Society.

3. Synthetic approaches

Various methods are employed in the synthesis of 2D materials and the HJs containing them. These approaches can generally be categorized into two main groups: *top-down* and *bottom up* methods. i) *Top-down* methods focus on the dimensional reduction of the bulk counterpart to obtain the final nanomaterial. Among all kinds of top down methods, electrochemical exfoliation, sonication exfoliation and acid etching are common methods used in the fabrication of photoelectrocatalyst (Figure 7).^{93,94} ii) *Bottom up* methods typically involve synthesizing the material beginning with the atoms or small molecular components, and the example of this strategy are CVD, hydrothermal synthesis, electrodeposition and polycondensation. The synthesis of the HJs generally includes one or more steps of synthesis method, and the multi-step synthesis combines various methods to build HJs with close interactions. The synthesis of HJs can be divided into *in-situ* and *ex-situ* strategies: i) in the *in-situ* synthesis the HJs are formed *in-situ* when one or more components are synthesized simultaneously. In this strategy, the bottom-up method is always used for crystallizing the last components and form HJs

eventually. ii) in the *ex-situ* synthesis, the components are synthesized independently and combined in the last step with a separate synthesis method. In this section, we will introduce mainly the combination of the synthesis methods on 2D HJs with the above-mentioned classification.

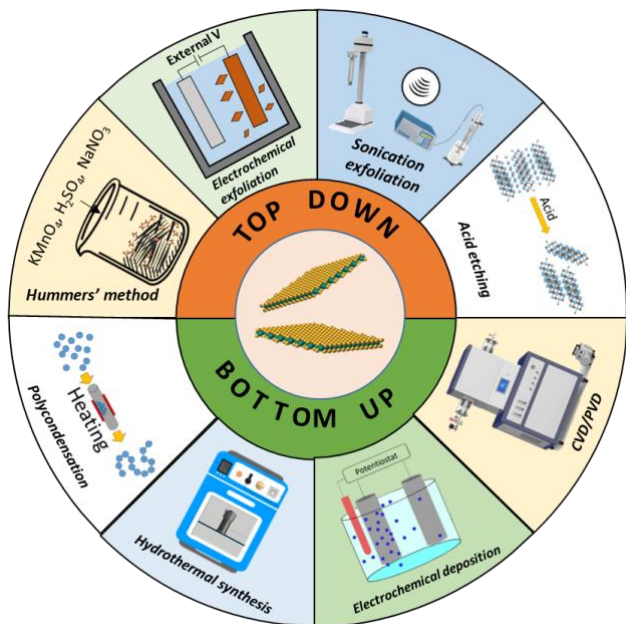


Figure 7. Commonly used top-down and bottom-up approaches for the synthesis of HJs containing 2D photoelectrocatalysts.

3.1 *In-situ* synthesis

In the *in-situ* synthesis, the formation of HJ is based on the direct and homogenous growth of one or more components. Usually, the more stable components are synthesized, followed by the addition of the less stable components to form the HJs. In this case, the 2D materials are usually firstly fabricated because of their better stability compared to other nanomaterial components and their ability as a platform to load and separate other nanomaterials.

For some popular 2D materials in the HJs, specific synthesis methods have been studied and developed on a relatively mature level, and they are synthesized individually as a platform for nucleation of the other components in the next synthesis steps. As a component of photoelectrocatalyst HJs, $g\text{-C}_3\text{N}_4$ is synthesized mainly by thermal polycondensation

method as a typical 2D platform for the HJ formation, and the *in-situ* formation of smaller nanoparticles on the surface of $g\text{-C}_3\text{N}_4$ can prevent the aggregation and result in more efficient interactions between two components. The precursors for $g\text{-C}_3\text{N}_4$ consist of urea, melamine, thiourea, and dicyandiamide, which are carbon and nitrogen-rich organics. For instance, by heating acid treated urea powder under $550\text{ }^\circ\text{C}$ for 2 h, Zhu et al synthesized ultrathin $g\text{-C}_3\text{N}_4$ nanosheets.¹⁵ Then Pt nanoparticles are loaded uniformly on the 2D $g\text{-C}_3\text{N}_4$ by a simple reflux method, as shown in Figure 8a and b. Similarly, Cu_2O nanoparticles⁹⁵ and CoMn-LDH ²⁶ can attach on $g\text{-C}_3\text{N}_4$ by a solution phase method. Besides, hydrothermal method is commonly used for *in-situ* crystallization of other components on $g\text{-C}_3\text{N}_4$ to form photoelectrocatalytic HJs, and typical examples include $\text{TiO}_2/g\text{-C}_3\text{N}_4$,⁴¹ $\text{BiVO}_4/g\text{-C}_3\text{N}_4$,⁵⁶ $\text{BiOCl}/g\text{-C}_3\text{N}_4$,⁹⁶ $\text{BiOI}/g\text{-C}_3\text{N}_4$,⁵⁵ $\text{La}_2\text{O}_3/g\text{-C}_3\text{N}_4$, $\text{Co}_3\text{O}_4/g\text{-C}_3\text{N}_4$,⁸⁷ $\text{ZnTe}/g\text{-C}_3\text{N}_4$,⁹⁷ $\text{NiMn-LDH}/g\text{-C}_3\text{N}_4$,²⁷ $\text{CuTi-LDH}/g\text{-C}_3\text{N}_4$,⁹⁸ $\text{Sn}_3\text{O}_4/g\text{-C}_3\text{N}_4$,⁶⁰ $\text{MoSe}_2/g\text{-C}_3\text{N}_4$,⁷⁹ $\text{SmV}/g\text{-C}_3\text{N}_4$,⁴³ $\text{Pt}/g\text{-C}_3\text{N}_4$,¹⁶ $\text{MoS}_2/g\text{-C}_3\text{N}_4$.⁹⁹ Except hydrothermal synthesis, other methods such as CVD,⁵⁷ solvothermal method¹⁶ can be used to grow HJs on the surface of $g\text{-C}_3\text{N}_4$ as well. For most nanomaterials with high surface energy, the risk of sintering and phase changing is high in a calcination step, thus the thermal polycondensation method for $g\text{-C}_3\text{N}_4$ is mostly in the first step. However, there are exceptions for the very stable nanomaterials connected to $g\text{-C}_3\text{N}_4$. For example, in $\alpha\text{-Fe}_2\text{O}_3/g\text{-C}_3\text{N}_4$ HJ, $\alpha\text{-Fe}_2\text{O}_3$ is made by hydrothermal method first, then goes through the calcination steps under $550\text{ }^\circ\text{C}$ which is the temperature to form $g\text{-C}_3\text{N}_4$ (Figure 8c).¹⁰⁰ Similarly, TiO_2 nanotube arrays can be synthesized by electrochemical anodization and used in the further step for $\text{TiO}_2/g\text{-C}_3\text{N}_4$ HJ by polycondensation as well.⁴⁰ It is possible to synthesize other types of carbon nitride such as $g\text{-C}_3\text{N}_5$ and CN by polycondensation with 3-amino-1,2,4-triazole and dicyandiamide as a precursor.^{59, 101} Further steps are then necessary to form the HJs. Apart from polycondensation method, CVD has been used for carbon nitrides and the HJs as well. For example, by using methylamine-borane as a precursor, borocarbonitride layers are deposited on TiO_2 nanoribbons for photoelectrocatalytic water splitting.¹⁰² Murugan et al. also reported a simple one-step soft template synthesis to prepare $g\text{-C}_3\text{N}_4/\text{TiO}_2$, which can be used as a photoanode for OER.³⁹

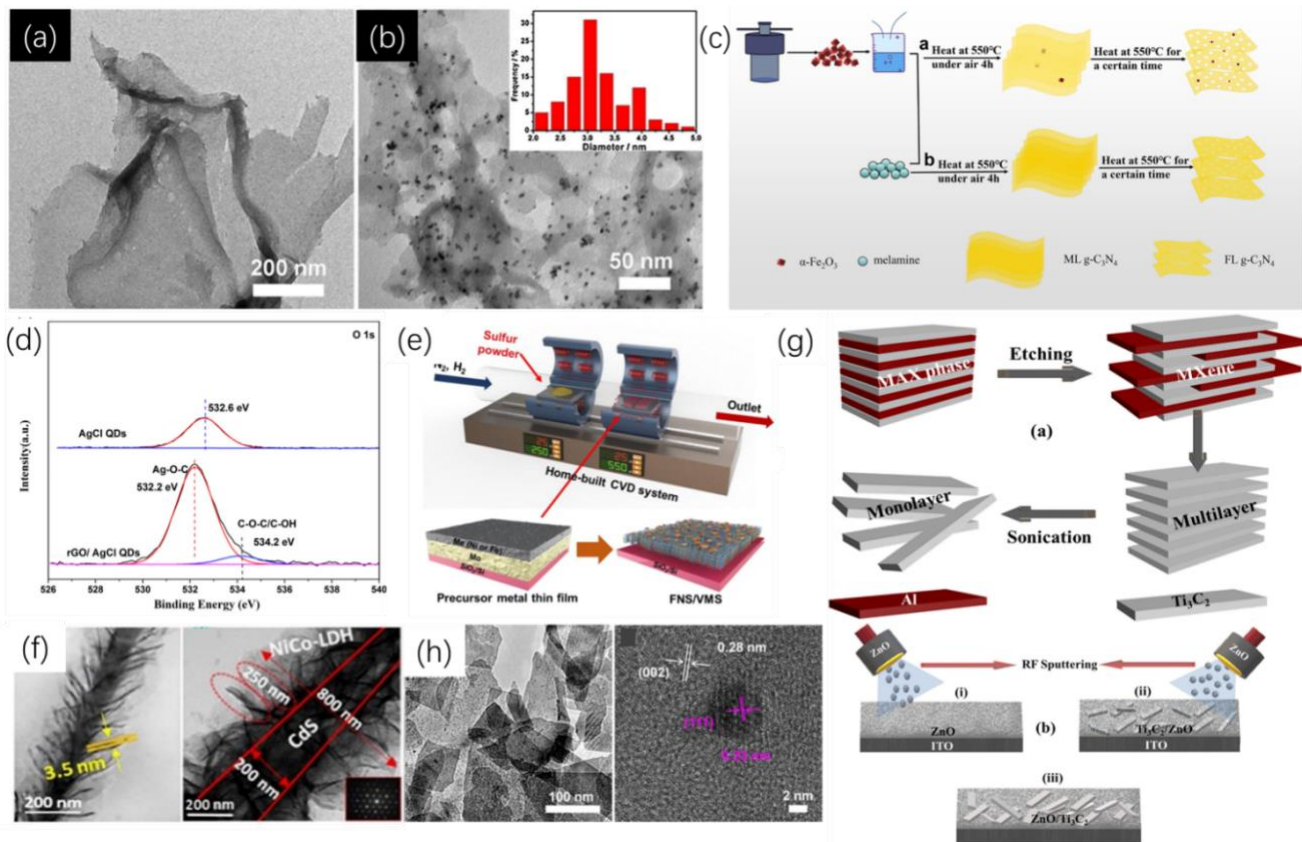


Figure 8. TEM images of pure ultrathin g-C₃N₄ nanosheets (a) and Pt/g-C₃N₄ nanocomposites (b). The inset of Figure 8b is the size distribution of Pt nanoparticles in Pt/g-C₃N₄ nanocomposites.¹⁵ © 2016 Elsevier B.V. (c) Schematic illustration of the synthetic route used to prepare the g-C₃N₄.¹⁰⁰ © 2020 The Chemical Society Located in Taipei & Wiley-VCH Verlag GmbH & Co. KGaA, Weinheim. (d) High resolution XPS spectra of O.⁴⁸ © 2019 The American Ceramic Society. (e) Schematic of experimental procedures and characterization of synthesized metal sulfide decorated MoS₂. © 2021 Elsevier B.V. (f) HRTEM images of the CdS@NiCo-LDH.²⁹ © 2018 Published by Elsevier B.V. (g) Schematic representation of the Ti₃AlC₂ MAX phase transformation into multilayer and monolayer Ti₃C₂ MXene and magnetron sputtering of (i) ZnO (ii) ZnO on monolayer Ti₃C₂ (Ti₃C₂/ZnO) and (iii) Ti₃C₂ on ZnO (ZnO/Ti₃C₂).¹⁰³ © 2021 Elsevier B.V. (h) TEM and HRTEM images of Pt/La₂Ti₂O₇.⁷³ © 2017 Taiwan Institute of Chemical Engineers. Published by Elsevier B.V.

RGO is generally synthesized by exfoliating graphite power via Hummers' method. Then other components will crystallize on the surface of rGO, such as Cu nanoparticles by electrochemical reduction process,⁵⁰ Ag₃PO₄ by electrodeposition,¹⁴ Pt/CdS combination by hydrothermal method.⁵¹ Graphene can be fabricated via CVD in which methane is used as the carbon source, and other components are deposited on the surface of graphene through different methods. For instance, Cu₂O can combine graphene by electrodeposition. Besides, hydrothermal method has been applied to reduce GO and construct a stable interaction in HJs containing rGO as well. For example, to prepare rGO/AgCl HJ, Kadeer et al. first mixed GO and AgCl quantum dots uniformly, then 2D GO was reduced and form Ag-O-C bonds simultaneously, which was confirmed by X-ray photoelectron spectroscopy (XPS) spectra of O (Figure 8d).⁴⁸

For the HJs containing TMDCs, they are usually synthesized by hydrothermal method which is used as the step of formation of HJ. For example, to synthesize BiOBr/MoS₂/GO HJ, (NH₄)₂MoO₄·4H₂O and (H₂N)₂S are chosen as precursors of Mo and S. Then the as-prepared GO is added in the precursor as a nucleation point for MoS₂.¹⁰⁴ Similar examples include MoS₂/TiO₂,⁹⁰ BiVO₄/SnS₂,⁶² MoS₂/La₂Zr₂O₇,⁸⁵ Al₂O₃/SnS₂,⁷⁶ MoS₂/CoMoS₄.⁷⁴ Moreover, hydrothermal synthesis can be

used as a single step to form HJs. For instance, to synthesize MoS₂/SnO₂ HJ, Na₂MoO₄, thiourea and SnCl₄·5H₂O are used as Mo, S and Sn precursors and mixed in the Teflon-lined autoclave for a one-step synthesis. It is easy to control the ratio between components by simply modifying the amount of the precursors. MoS₂ layered materials can be obtained by liquid phase exfoliation and applied as a platform for nucleation of other components such as Au.⁸⁴ Besides, it is possible to synthesize layered TMDCs through vulcanization or selenization of the corresponding oxides in the HJs, for example, from MoO_x/Si to MoS₂/Si and MoSe₂/Si.¹⁰⁵ It has to be mentioned that environmental friendly chemicals have been used to replace precursors with health risk. In the hydrothermal synthesis of Au-WS₂ HJ, organosulfur from rotten garlic powder is used as a S precursor alternative of CH₂N₂S, providing a possibility for "green synthesis".⁶³ CVD is a commonly used method for constructing HJs containing MCs as well. For example, GaTe/ZnO is synthesized by a 2-step of CVD: the first step is to grow ZnO nanowire, while the second step is to grow GaTe nanosheets on ZnO.⁶⁴ On the other hand, MoS₂/WS₂ and Fe-doped Ni₃S₂/WS₂ can be synthesized by one step CVD considering the possibility of both components of changing from oxide hydrate or metal precursors to sulfides simultaneously (Figure 8e).^{77, 86} Furthermore, MoS₂/Si,¹⁰⁶

$\text{Sn}_x\text{Mo}_{1-x}\text{S}_2/\text{MoS}_2$,⁸¹ MoS_2/WO_3 ,¹⁰⁷ HJs can be synthesized by decorating MoS_2 via CVD. Zheng et al. reported a chemical bath method to coat MoS_2 on BiVO_4 photoanode. In principle, the $(\text{NH}_4)_2\text{MoS}_4$ precursor remains on BiVO_4 by a merging step, then a calcination is needed to obtain stable $\text{MoS}_2/\text{BiVO}_4$ HJ.¹⁰⁸

LDHs can be easily synthesized by different kinds of wet chemical methods. Usually, the LDHs are easily formed on other components to produce HJs because of their flexibility in synthesis. For instance, CoFe LDH crystallizes easily on the surface of BiVO_4 in the ethanol solution of $\text{Co}(\text{NO}_3)_2$ and $\text{Fe}(\text{NO}_3)_3$, thus forming HJs photoelectrocatalytic water splitting.³⁰ Pirkarami et al. grow NiCo LDH microsheets on the surface of CdS by hydrothermal method by using $\text{Co}(\text{NO}_3)_2$ and $\text{Ni}(\text{NO}_3)_2$ as precursors (Figure 8f).²⁹ Zhu et al. grow NiFe LDH on $\alpha\text{-Fe}_2\text{O}_3$ particles via a fast electrodeposition method. Besides, LDHs can be used as nucleation points for other components. For example, Co_3O_4 is synthesized with NiFe -LDH as nucleation point to form a p-n HJ for photoelectrocatalytic removal of contaminants.³²

2D layered MXene is mostly obtained by acid etching method, then used for combining other nanomaterials to form HJs. As a popular MXene used in PEC, Ti_3C_2 is obtained from Ti_3AlC_2 by selectively etching Al layers inside Ti_3AlC_2 structure (Figure 8g). Then the layered Ti_3C_2 is used for crystallization of other nanomaterials, such as Ti-ZnO ¹⁰⁹ and ZnO ¹⁰³ by magnetron sputtering, Bi_2TiO_7 ⁶⁵ and TiO_2 ⁶⁸ by hydrothermal method.

BiOI is synthesized by hydrothermal method, followed by a second step of hydrothermal to produce Pt/BiOI as a photoelectrocatalyst for ethanol oxidation reaction.³⁴ Moreover, it can be deposited on BiPO_4 by electrochemical method for photoelectrocatalytic degradation of tetracycline.⁴⁵

Except the above mentioned popular 2D layered materials and the HJs based on them, additional new materials have been reported as active for PEC, and the corresponding synthesis method is newly designed as well. Ultrathin $\text{La}_2\text{Ti}_2\text{O}_7$ nanosheets can be synthesized via facile hydrothermal method with $\text{La}(\text{NO}_3)_3$ and $\text{Ti}(\text{SO}_4)_2$ are precursors, while photo-reduction method was applied to load Pt nanoparticles to form a HJ for methanol oxidation reaction (Figure 8h).⁷³ $\text{Bi}_2\text{WO}_6/\text{La}_2\text{Ti}_2\text{O}_7$ can be obtained by a simple hydrothermal method as well.⁷¹

3.2 Ex-situ synthesis

In the *ex-situ* methodologies, the components for the HJs are synthesized or prepared firstly, then a process is formed to anchor the existing components to each other via covalent or noncovalent interactions. In general, top-down synthesis is applied for producing 2D layered materials, which are combined with other components in the last synthesis step. For example, Wang et al. synthesized $\text{MoS}_2/\text{BiOBr}$ HJs via a two-step liquid phase exfoliation. The two components are combined with vdWs interaction, which is proved by the shift of the MoS_2 characteristic peaks in the Raman spectra (Figure 9a).³⁷ Si et al. managed to obtain $\text{MoS}_2/\text{WSe}_2$ by liquid phase exfoliation as well with isopropanol/ H_2O solvent.⁷⁵

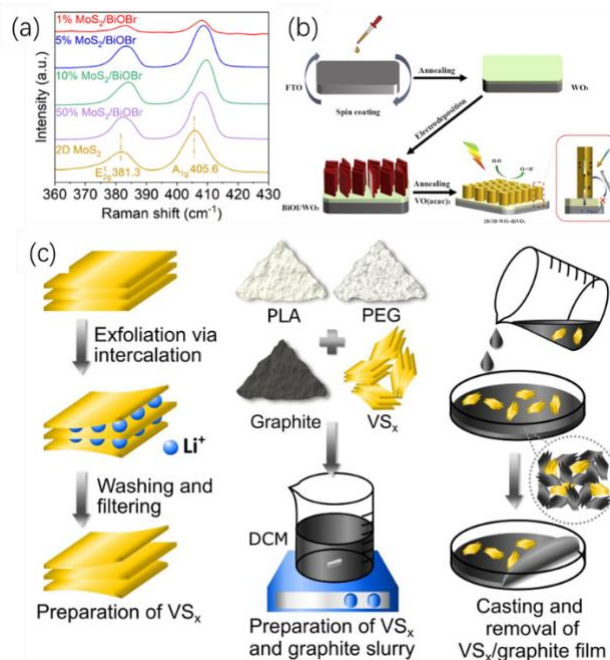


Figure 9. (a) Raman spectra of the HJs and 2D MoS_2 in the range of 360–430 cm^{-1} .³⁷ © The Royal Society of Chemistry 2023 (b) Schematic for the preparation of 2D/3D $\text{WO}_3/\text{BiVO}_4$ photoanode.⁷⁰ © 2021 Hydrogen Energy Publications LLC. Published by Elsevier Ltd. (c) Schematic illustration of the preparation of exfoliated VS_x and a flexible graphite film that contains the exfoliated VS_x .⁸⁰ © 2022 Elsevier B.V.

Spin-coating deposition is a common method for ex-situ synthesis of HJs. To fabricate uniform HJs, the suspension of each component should have the desired stability and viscosity. For instance, to fabricate $\text{TiO}_2/\text{In}_2\text{S}_3/\text{GO}$ HJ, GO powder was firstly obtained by Hummer's method, then dispersed in ethanol with acetic acid by ultrasonication to form a GO suspension. The suspension is eventually coated on the $\text{TiO}_2/\text{In}_2\text{S}_3$ structure.⁵²

Electrochemical deposition can be used to fabricate photoelectrodes with HJs. For instance, $\text{rGO}/\text{CeO}_2/\text{TiO}_2$ HJ was prepared by electrochemical deposition of rGO on $\text{CeO}_2/\text{TiO}_2$, using $\text{CeO}_2/\text{TiO}_2$ as a working electrode and GO dispersion as electrolyte.⁴⁹ $\text{WO}_3/\text{BiVO}_4$ electrode was fabricated by electrodeposition of WO_3 , in which WO_3 is used as a working electrode (Figure 9b).⁷⁰

The *ex-situ* synthesis of HJs can be achieved by simply mixing and depositing the components as well. For example, to prepare $\text{VS}_x/\text{graphite}$ film, Ng et al. mixed VS_x and graphite with other polymers including poly(lactic acid) and poly(ethylene glycol) to make a homogeneous slurry. The HJ film is then obtained by casting and drying on a Petri dish (Figure 9c).⁸⁰ WO_3/WS_2 HJ can be synthesized by a simple drop casting step.⁴⁶ Zhang et al. synthesized carbon quantum dots/ $\text{g-C}_3\text{N}_4$ via a simple ultrasonic dispersion self-assembly method.⁵⁸ Samsudin et al. managed to decorate rGO on $\text{g-C}_3\text{N}_4/\text{BiVO}_4$ by a simple wet-impregnation method.⁴⁷

Compared to the *in-situ* synthesis strategy, the *ex-situ* synthesis is not used frequently. However, in the *ex-situ* synthesis, each component of the heterojunction is synthesized independently before combining them. This allows for precise control over the

properties of each material, such as size, shape, composition, and crystallinity. Processing conditions for each material can be optimized independently. This can simplify the fabrication process and enhance the reproducibility of the heterojunction, as the synthesis of each component is not constrained by the presence of other materials. Researchers can optimize the properties of individual components separately, ensuring that each material is tailored to contribute specific characteristics to the heterojunction. This can lead to improved performance in the final application.

4. Computational methods

Theoretical modeling involves the study of materials at the atomic scale using the concepts of quantum mechanics (QM) or molecular mechanics (MM) and relying on appropriate algorithms and codes running on powerful supercomputers.¹¹⁰

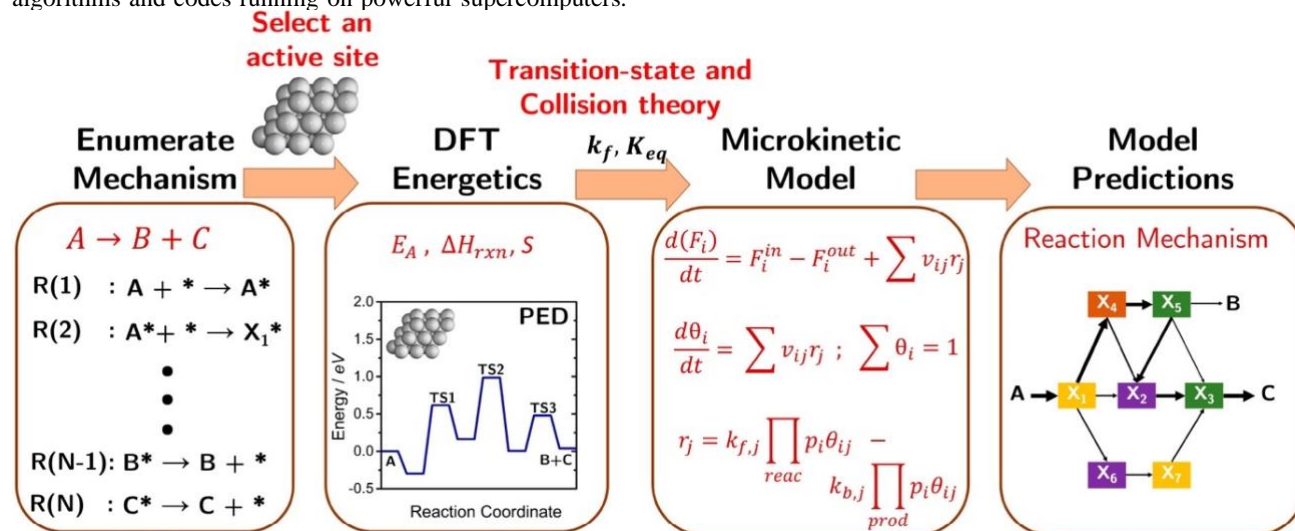


Figure 10. Schematic representation of the typical workflow adopted in a microkinetic-modeling (MKM)-based analysis for heterogeneous catalysis. A, B/C, and Xi refer to reactant, products, and reaction intermediates, respectively. PED refers to potential energy diagram. Reactor balance equations (system of differential-algebraic equations) solved in a MKM are shown in the third panel. Reprinted with permission from ref. ¹¹¹. Copyright 2020 American Chemical Society.

4.1 Interface modelling

First-principles density functional theory (DFT)^{112,113} calculations have overcome a challenge to explicitly understand both the surface configuration and the structure-dependent electronic structure, charge carrier mobility and photoelectrocatalytic properties of interfaces.¹¹⁴ It is essential to build an interface model of the 2D-layered HJ as close as possible to the real situation, described via employing experimental characterization techniques.^{114–117} As an example, certain facets of the surface may be more reactive than others in a catalytic material,¹¹⁸ or the presence of defects can constitute the most active catalytic sites due to their chemical surroundings or unsaturation.¹¹⁹ Therefore, careful understanding of the experimentally measured data from different spectroscopy and microscopy techniques, etc. is vital to model the correct HJ structure. In addition, surface reconstruction events may occur after creating heterostructures by combining different dimensional systems.⁹⁵ These effects are easily captured by optimization steps in DFT calculations, and if the DFT functional inherently includes dispersion (optB88-vdW¹²⁰, vdW-DF2¹²¹) or dispersion corrected functionals^{122,123} are selected, then the DFT shall provide correct structures.

Theoretical calculations provide a versatile method that allow us to help understanding the experimental data by providing the necessary atomistic detail into the studied problems, as well as provide the additional insight which could be hardly accessible by experiments. Thus, they shall be regarded as an indispensable part of research, together with experiments, to elucidate the mechanism behind PEC. Their advantages include the ability to isolate a particular issue from a complex problem, and conduct cost-effective material screening, making it a suitable method for discovering suitable photoelectrocatalysts (Figure 10). In the following section, we first introduce the most common methodologies and then we show how they can be used to provide insight into different PEC reactions on 2D materials and heterostructures, thus completing the experimental data.

Once the models of catalytic interfaces are built, DFT calculations allow to study their interactions which are typically described by the calculation of binding/adsorption energies and evaluation of the Gibbs energy profile to assess the catalytic mechanism. The Sabatier principle¹²⁴ for heterogeneous catalysis guides this approach. It states that the optimal catalyst binds adsorbates and intermediates with an appropriate binding energy: if intermediates are bound too strongly, they block active sites, and if they are too weakly adsorbed, they are not sufficiently present on the surface to allow for high reaction rates. The Sabatier principle is most often represented as a volcano plot.^{125,126}

In addition to the static DFT calculations, molecular dynamics (MD) simulations can generate the time evolution of all the particles (atoms, ions, molecules) of a model HJ using a classical, Newtonian MD approach. However, in classical MD breaking bonds is not allowed. Thus, other types of MD simulations such as *ab-initio* MD (AIMD),¹²⁷ MD simulations with (reactive) force fields, e.g., ReaxFF,^{128,129} AIMD-based metadynamics,^{130,131} constrained molecular dynamics (CMD),¹³² or density functional theory in classical explicit solvent (DFT-CES) simulation¹³³ can be employed. AIMD is a powerful tool that can quantify the interaction potentials and

describe the physical–chemical nature of active sites of the catalyst. This method is very popular when explicit molecules of solvent are considered to be vital in the theoretical description.^{134,135} ReaxFF based classical MD simulations allows bond breaking and forming but decreasing the computational cost as electrons are not computed. One of the most important features of ReaxFF is the use of charge equilibration (QEq) approach for handling the electrostatic interactions.¹³⁶ QEq calculates the actual charge distribution for every step of the MD trajectory and expands the electrostatic energy as a Taylor series where the linear term is identified as electronegativity of the atom and the quadratic term as electrostatic potential and self-energy.¹³⁷ DFT-CES offers an accurate description of the electrified interface at a balanced computational cost, by mean-field coupling of a QM description on the catalyst interface with a molecular dynamics description on the liquid structure of the electrolyte phase.¹³⁸ Compared with the AIMD simulation, the DFT-CES enables to investigate electrolyte phase dynamics with many more atoms over a more extended time-scale.

Apart from the information about interaction energetics between the adsorbent and the 2D-HJ, the electronic structure of the 2D-nanostructure before and after the adsorption of the targeted molecule is necessary to give insight onto the PEC process. This can be also obtained by DFT calculations.^{139,140} DFT calculations with local density approximation (LDA)¹⁴¹ and generalized gradient approximation (GGA)¹⁴² functionals usually underestimate the bandgaps of semiconductors,¹⁴³ while the Heyd–Scuseria–Ernzerhof (HSE) hybrid functional¹⁴⁴ leads to more accurate results of bandgaps with respect to experimental data due to the long-range correction present in its functional form. A different strategy is to use wave-function based methods, such as many-body perturbation theory (MBPT) with the Green functions (G) and screened Coulomb potential (W).¹⁴⁵ Calculation of the energy alignment of VB and CB for periodic models and of frontier orbitals (highest occupied molecular orbital, lowest unoccupied molecular orbital) for molecular systems is a computationally simple approach used to determine the adequacy of different photoelectrocatalytic HJs for PEC e.g., in the case of water splitting, by comparing these energies with reduction potential energy, etc.¹⁴⁶ Additional descriptors commonly used to assess the catalytic activity of HJs are band-structure, total or partial density of states, charge difference distributions, Bader^{147,148} charge analysis.

4.2 PEC calculations

The computational description of the full PEC process is a very challenging task, and, up to date, there are no available computational methods which can describe it in their entirety. This is mainly related to the difficulties in combining exciton dynamics with catalysis, since it requires the solution of the time-dependent Schrödinger equation for the many-body system, which has so far only been achieved for small molecules and is not yet applicable for HJs.

Involving nonradiative transitions between several electronic states using nonadiabatic MD (NAMMD) is relevant in PEC, nevertheless, the methodology is still very rare in this field due to its enormous computational cost. The issue is not intrinsic of the methodologies used to properly describe the excited state (ES) potential energy surface, but relates to the hundreds of trajectories needed to be run in order to achieve reliable statistics.^{149,150} The combined use of time-dependent density

functional theory (TDDFT),^{151,152} efficient in solving electronic problems, with NAMMD can track the pathway of ES carrier energy over time, describing trajectories that evolve or jump between coupled (electronic) potential energy surfaces. The main energy loss involved in PEC at HJs is the nonadiabatic coupling between electrons and atoms. This nonadiabatic problem can be investigated by mean-field classical molecular dynamics,¹⁵³ using the so-called Ehrenfest dynamics,^{154,155} or Tully's fewest switches trajectory surface hopping¹⁵⁶ which is self-consistently coupled with TDDFT for the description of the electronic degrees of freedom.¹⁵⁷ The hybrid quantum and classical dynamics approach evolves the electron wavefunction by solving the electron Schrödinger equation and describing the motion of the nucleus in Newtonian mechanics¹¹⁵. However, this technique is highly expensive in term of computational cost,¹⁵⁰ even though a few different codes (Hefei-NAMMD, PYXAID) able to investigate the interfacial charge carrier dynamics, the electron–hole recombination dynamics, the exciting spin-polarized hole dynamics, have been developed.^{158–160}

To solve this problem, the commonly used approach is to consider the PEC as two separate processes: (i) light harvesting and CT and (ii) electrocatalytic calculations. In this way, it is possible to compute a large part of the PEC process, although with the assumption that the catalysis is performed in the ground state (GS).

4.3 Light harvesting and charge transfer in 2D heterojunctions

QM approach based on TDDFT is the most used methodology for the description of ESs, as it enables modelling large systems and interfaces with high accuracy. However, since TDDFT is based on one-electron picture of the electronic GS, approximation must be considered.¹⁴⁶ The most common approximations in modelling the photogenerated holes and electrons include (i) study the positively (negatively) charged system by removing (adding) one electron, which inherently neglects the existence of the exciton and of the hole–electron interaction and is typically used for finite systems; (ii) adding electron traps or donors, to simulate hole or electron existence by, e.g., adding –OH or –H surface groups onto the periodic models, which is limited by the precise knowledge of the positioning and surface coverage of the functional groups;¹⁶¹ (iii) first-principles MDs describing the GS of the system upon addition or removal of electrons, avoiding the costly ES calculations;¹⁶² (iv) open-shell DFT calculations of the singlet photoexcited state, where the two unpaired electrons are coupled to a triplet spin state, allowing the structural optimization of the system in an excited-state potential energy surface which is supposed to be close to that of the singlet state.

For calculations of periodic systems, in addition to the prediction of the fundamental band gap, excitonic effects must be included in the determination of the optical band gap of a 2D material.¹⁴⁵ Most 3D semiconductors exhibit very small exciton binding energies, and hence, the distinction between optical and electronic bandgaps is frequently ignored. However, in 2D materials and for some organic semiconductors, the difference can be significant.¹⁵⁰ The optical absorption function is given by the imaginary part of the dielectric function and can be computed using DFT or the by applying GW quasiparticle approximation, including excitonic effects by solving the Bethe–Salpeter equation (BSE).^{150,163} Despite the higher accuracy, this method is more computationally expensive

compared to TDDFT, scaling as N^4 with the system size,¹⁶⁴ making TDDFT the best trade-off between accuracy and quality.¹⁶⁵

TDDFT calculations can also provide information on the location of the photogenerated holes and electrons at the HJ. By analyzing the charge distribution, it is possible to discriminate between CT or energy transfer processes that can take place at the interface and observe how the generated charge carriers are transported to the adsorbed molecules at the catalytic site to induce redox reactions.

Despite its benefits, the use of TDDFT needs to be considered with caution, as it (i) is incapable to properly describe systems with polyradical character of the GS wavefunction, (ii) fails to include doubly ESs due to the adiabatic approximation of the time-dependent correlation-exchange potential,¹⁶⁶ (iii) sometimes incorrectly orders the ESs based on the poor choice of the exchange-correlation functional,^{167,168} and (iv) fails to properly describe CT states.¹⁶⁹

For 2D-HJs, it is important to consider the lowest ES providing that the photogenerated charges are easily separated and transported at the catalytic sites. Thus, it could be assumed that the system evolves on the energy surface of its lowest ES before partaking in the PEC reaction. An exact description requires to obtain the optimized geometry of the first ES, and it can be computationally demanding. To avoid this bottleneck, the classical path approximation, in which the ES structure of each intermediate step in the reaction path is approximated by the GS structures,^{160,170} ignoring the response of the nuclear system to the excited electrons, can be adopted. For HJs, such approximation holds true since they have many electrons, and the excitation of a single electron has a limited influence on the system. Moreover, the excited electron lifetimes are very short, and the nuclear system has no time to respond to these short-lived excited carriers. Unfortunately, such calculations are barely performed in this field, even employing these simplifications.

4.4 Electrocatalysis calculations

Electrocatalysis is driven by applying a voltage across the reaction cell, providing a sensitive control of the rate. Therefore, for electrocatalysis calculations, the DFT procedure needs to be corrected to represent constant-potential conditions to make direct comparison with electrochemical available experiments.^{171–173} The two most common methodologies to estimate the catalytic performance for electrocatalysis are the computational hydrogen electrode (CHE) model,^{174–176} developed by Nørskov et al., and the grand canonical potential kinetics (GCP-K) method,^{177–180} developed by Goddard III et al. Both these methods can calculate the thermochemistry of the entire process by including additional factors such as pH and applied potential in the Gibbs free energy formulation for each reaction step (including transition states), however, while the CHE consider constant charges, the GCP-K allows for changes in charges during the catalytic steps.

4.4.1 Computational hydrogen electrode (CHE)

CHE prominently opened the door of EC to theoretical description. Thanks to its simplicity and computational efficiency, the CHE approach enabled studies of reaction pathways and large-scale computational screening studies with the purpose of finding the optimal electrocatalytic material for different reduction reactions.¹⁸¹ It enables the computation of the relative Gibbs free energies of intermediates of a series of

proton-coupled electron transfer (PCET) steps along an electrochemical reaction pathway. Each elementary step is formulated as a removal or addition of the electroactive species, (proton + electrons). For simplicity, we introduce CHE for the Volmer step of the HER reaction in acidic aqueous solution $H^+_{aq} + e^- + * \rightarrow H^*$, where $*$ represents a catalyst surface, H^* hydrogen adsorbed on the catalyst and H^+_{aq} proton in the aqueous solution. For this reaction, the Gibbs free energy ΔG shall be calculated from equation 1:

$$\Delta G = G(H^*) - G(*) - G(H^+_{aq}) - \mu_e \quad (1)$$

where $G(H^+_{aq})$ depends on the pH of the solution (2):

$$G(H^+_{aq}(pH)) = G(H^+_{aq}(pH = 0)) - 0.059pH \quad (2)$$

The chemical potential of electrons μ_e is the change in free energy when the electron is added or removed from an (infinitely large) system and depends on the electrode potential U which is referenced to the standard hydrogen electrode (SHE). Thus, equation 2 can be rewritten as:

$$\Delta G = G(H^*) - G(*) - G(H^+_{aq}(pH = 0)) - \mu_e(0_{SHE}) + 0.059pH + |e|U_{SHE} \quad (3)$$

The $G(H^*)$, $G(*)$, and $G(H^+_{aq})$ terms can be calculated from first-principles methods, typically DFT in the field of catalysis of 2D HJs, either in gas, but preferably in the implicit solvation as most of the experiments are done in some aqueous electrolyte. Nevertheless, it is still difficult to determine the $G(H^+_{aq}(pH=0))$ from first-principles, which not only involves the strong solvation but also the proton concentration.¹⁸² This bottleneck is overcome by the assumption that energies of other species can be easily calculated based on the existence of thermodynamic equilibrium in the SHE (equation 4):

$$G(H^+_{aq}(pH = 0)) + \mu_e(0_{SHE}) = G(H_2)/2 \quad (4)$$

As a result, the free energy can be calculated with DFT calculations by substituting equation 4 to equation 3 (equation 5), where all terms on the right side of the equation are known.

$$\Delta G = G(H^*) - G(*) - G(H_2)/2 + 0.059pH + |e|U_{SHE} \quad (5)$$

Overall, the essence of the CHE is that the free energy of solvated ions, which is difficult to obtain from DFT calculations, can be deduced from the equilibrium reaction where the energies of other species can be easily calculated or have been experimentally measured.¹⁸²

Due to its simplicity, the CHE method has been widely used for investigations of low-dimensional systems catalysis. This method allows to find an onset potential (minimum overpotential), which drives all the reaction steps towards the formation of the final product. Nevertheless, CHE still poses several drawbacks. First, it is not well adapted to study explicit pH effects and implicitly assumes that the neutral surface state computed by DFT is representative of 0 V vs reversible hydrogen electrode (RHE).¹⁸³ In other words, the electronic energies are only measured for electroneutral entities independently from the electrochemical potential as the electron transfer reaction is always coupled, even though in real systems electrons are exchanged between catalyst and electrode to reach equilibrium, where Fermi level of the catalyst and electrode potential shall be equal. Moreover, the effect of surface charge/constant potential can be significant in heterogeneous electrochemistry, especially for low-

dimensional HJs, where the change of charge affecting the electronic structure is not confined to the catalytic center. Secondly, the solvation effects are assumed to be negligible, and only computations in the gas-phase are necessary to evaluate electrocatalytic reaction pathways. Even though simple approaches to predict reaction barriers have been derived,^{184,185} CHE model neglects the activation energies of all PCET steps and therefore is not reliable for accurate kinetics.

Hence, different methods have been derived and implemented to reach more realistic theoretical description. Methodologies such as GCP-K, or constant potential-hybrid solvation-dynamic model (CP-HS-DM) appear to be useful to describe the kinetics at solid–water interface¹⁸⁶ and for decoupled electron transfer/proton transfer.^{187,188} CP-HS-DM methodology overcomes the oversimplification of CHE by (i) considering that the configurations and interactions of explicit water molecules can evolve along the reaction coordinate; (ii) not assuming that the system has zero (or constant) net electronic charges and does not neglect the surface charge effects. The key feature of the CP-HS-DM is the implementation of the constant-potential condition for electrons to the slow-growth AIMD. Practically, it uses several layers of explicit water molecules in conjunction with an implicit solution to solve the reaction species. The electrons are coupled with a fictitious potentiostat so that the Fermi level of the system fluctuates around a constant and the number of electrons evolves following the grand-canonical distribution at the preset electrode potential. The constrained AIMD simulations are performed with reaction coordinate gradually changing from the initial to the final state. Eventually, the mean force with respect to the reaction coordinate is integrated, giving the free energy profile, from which the activation energy can be identified.¹⁸⁶

4.4.2 Grand canonical potential kinetics formulation (GCP-K)

The recently developed GCP-K QM formulation based on thermodynamics calculations provides the understanding of heterogeneous electrochemical reactions by describing reaction kinetics as a function of an applied potential (U). In traditional QM, the number of electrons is fixed. In the GCP-K method, the number of electrons is automatically adjusted to the fixed applied potential, leading to a quadratic dependence of the potential on U . This provides physical quantities which describe differential capacitance during CT from the electrode to reacting species.¹⁸⁹ GCP-K method is elegantly capable of predicting electrochemical kinetics, thus, calculate current density and turnover frequency as a function of applied potential rather than for fixed charges as in standard QM. It describes how the energy barrier of transition state and its structure change with a fixed applied potential, which leads directly to current versus potential relation (Tafel slope). It has been demonstrated that GCP-K accurately describes the PCET process during different electrocatalytic reactions and it has already been successfully employed in a few theoretical works where a good agreement with experiments has been found.^{177,189,190}

In more details, the voltage-dependent GCP for surface states can be derived from traditional fixed-electron based free energies by using a Legendre transformation.¹⁷⁷ The GCP-K formulation arises from minimizing the free energy for each value of n in Equation (7) using a Legendre transform relating the net charge of the system and the applied voltage. Performing this macroscopic transformation explicitly allows to make the

connection of GCP-K to the traditional Butler–Volmer kinetics (Figure 11),

$$G(n; U) = F(n) - ne(U_{\text{SHE}} - U) \quad (7),$$

where G is the grand canonical free energy, which depends on the applied potential U_{SHE} vs SHE, n is the number of electrons, e the unit electronvolt in energy, F is the free energy obtained as a function of n and $U_{\text{SHE}} = \mu_{e,\text{SHE}}/e$ is the electronic energy at SHE conditions. The Fermi level can be shifted by changing the reference electrode based on the pH of the solution. To use $G(n; U)$ as a thermodynamic potential, the number of electrons needs to be equilibrated with the applied potential. The Fermi level shift with applied potential is achieved by changing the number of electrons of a system (changing the occupation of the electronic bands) during QM self-consistent calculations.¹⁸⁹ GCP is then obtained by minimizing the free energy following Equation (8):

$$\begin{aligned} GCP(U) &= \min_n G(n; U) \\ &= \min_n F(n) - ne(U_{\text{SHE}} - U) \quad (9). \end{aligned}$$

The minimization of free energy as a function of n shall be at least quadratic to describe the minimization of $GCP(n; U)$. That is why free energy $F(n)$ as a function of number of electrons is expanded as a quadratic form (Equation (9)):

$$F(n) = a(n - n_0)^2 + b(n - n_0) + c \quad (10),$$

where a, b, c are the fitting parameters. This leads to Equation (11)

$$\begin{aligned} GCP(U) &= -\frac{1}{4a}(b - \mu_{e,\text{SHE}} + eU)^2 + c \\ &\quad - n_0\mu_{e,\text{SHE}} + n_0eU \quad (11), \end{aligned}$$

where the final form of GCP becomes

$$n = n_0 - \frac{C_{\text{diff}}}{e}(U - U_{\text{PZC}}) \quad (12)$$

$$\begin{aligned} GCP(U) &= -\frac{C_{\text{diff}}}{2}(U - U_{\text{PZC}})^2 + F_0 \\ &\quad - n_0\mu_{e,\text{SHE}} + n_0eU \quad (13), \end{aligned}$$

$$\begin{aligned} F(n) &= \frac{e^2}{2C_{\text{diff}}}(n - n_0)^2 + (\mu_{e,\text{SHE}} \\ &\quad - eU_{\text{PZC}})(n - n_0) + F_0 \quad (14). \end{aligned}$$

where U_{PZC} is the potential at zero charge; $\mu_{e,\text{SHE}}$ is the chemical potential of an electron at SHE; F_0 is the free energy at zero net charge; n_0 is the number of electrons at zero net charge.

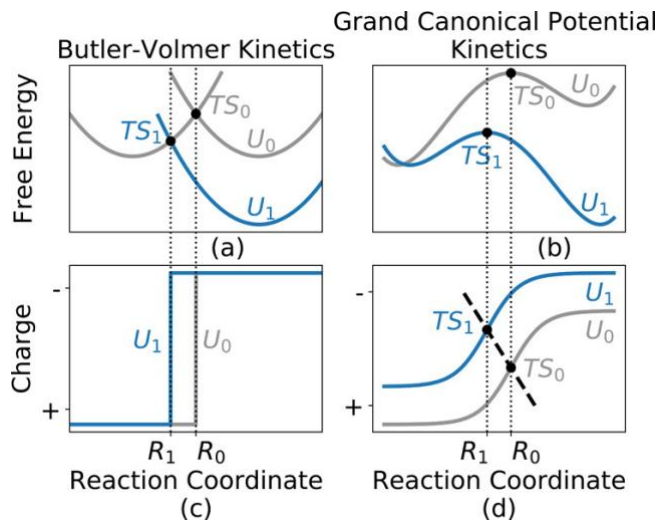


Figure 11. Schematics showing how voltage dependent electrochemical reactions are described by GCP-K. (b) and (d) differ from the more standard view of Butler–Volmer kinetics (a) and (c). As the voltage is changed from U_0 to U_1 , the energy profiles shift as in (a) and (b), while the relevant reaction coordinate changes from R_0 to R_1 . The Butler–Volmer picture in (c) can be considered as a special case of the GCP-K scheme (d) in which the electron transfers instantaneously. Reprinted with permission from ref. ¹⁷⁷. Copyright 2018 American Chemical Society.

For neutral system, $F_o(n = n_0) = c$ (from Equation 10); $b = \mu_{e,SHE} - eU_{PZC}$ (from Equation 4). Because of this formulation, the differential capacitance C_{diff} across the electrode and electrolyte can be calculated $C_{diff} = -e \frac{\partial n}{\partial U} = \frac{e^2}{2a}$; where $a = \frac{e^2}{2C_{diff}}$ (from Equation 11). This all allows a continuous description of the evolution of the reaction intermediates and transition states.

Despite its versatility, the computational cost of the GCP-K approach is higher than the CHE one, and its application to low dimensional materials just started to be relevant.¹⁹¹ Nevertheless, its high accuracy, implementation, and ability to provide physical observables, make this method a much reliable choice for EC reaction studies compared to CHE.

4.5 Microkinetic modelling

First-principles kinetics can simulate EC processes in real time, considering rare reaction events, and the method may be parametrized by data, including adsorption energies and kinetic barriers, obtained from DFT calculations and transition state theories. First-principles kinetics is then followed by kinetic modeling such as (i) microkinetic modeling or (ii) kinetic Monte Carlo (kMC) simulations. In microkinetic modeling, a set of differential equations is simultaneously solved to calculate the overall reaction rates and species concentrations, describing the catalyst surface, gaseous phases, and, if relevant, liquid phase and interfaces (Figure 10).¹¹¹ Usually, competitive adsorption, desorption, and surface transformations are included.^{192,193} Microkinetic modeling needs all relevant rate constants of the reaction as an input, calculated from all the energies of the relevant reaction intermediates and transition states as functions of applied potential using the quadratic grand canonical potential, and then obtained using the Eyring

equation. For periodic systems, transition states are commonly computed using the climbing image nudged elastic band calculations.^{194,195} Another effective way to obtain the kinetic barrier is the Brønsted–Evans–Polanyi (BEP) relationship.^{196,197} It relates the kinetic barrier to the corresponding reaction energy for a class of materials: $\Delta G^\ddagger = \beta \Delta G + \alpha$, where ΔG^\ddagger , β , ΔG , and α are the kinetic barrier, BEP coefficient, reaction energy, and a constant, respectively. BEP relationship allows one to estimate the kinetic barrier by simply calculating the reaction energy, leading to a significant reduction in computational costs and permitting high-throughput screening of materials.^{198,199} For EC, its main approximation is that the transition state for the nonelectrochemical step is equivalent to that of the electrochemical step at a specific potential U (Equation (15)):

$$\Delta G^\ddagger(U) = \alpha(U)(\Delta G(U) + neU) + \beta(U) \quad (15),$$

where $\alpha(U)$ and $\beta(U)$ represent the best fit slope and intercept of the BEP scaling relation that vary with potential.¹⁹¹

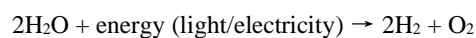
Microkinetic modeling is not computationally demanding, however, it deals with averages, hence it lacks the capabilities to probe the catalyst surface on the atomistic level, such as tracing the effects of adsorbate relative positions, *i.e.*, lateral interactions and cooperative effects.¹⁹²

On the other hand, kMC^{200,201} is a relatively cheap method, which can be applied for EC in estimating material properties, charge transfers at the interface or reaction paths.^{110,202} The combined DFT and kMC approach could provide a detailed picture of the interplay between thermodynamics and kinetics, as well as precise predictions of the current and voltages for electroreduction reactions as a function of the applied electrochemical potential.²⁰³ kMC simulations are also capable to assess the charge transport and electron dynamics processes at the interface in the framework of a hopping regime,²⁰⁴ as well as to cast down the contributions from the different constituents of the system and helping in avoiding possible causes of charge recombination.²⁰⁵

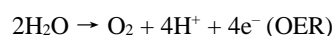
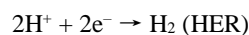
5. Photoelectrochemical applications of 2D materials

5.1 PEC water splitting

The PEC water splitting reaction occurs at the interface of the photoelectrode and the electrolyte solution. The photo-generated electrons reduce water to form hydrogen gas while the holes generated in the photoelectrode oxidize water to form oxygen gas. The overall reaction is represented as:



The whole reaction can be divided into two half reactions, namely HER and OER, which take place on photocathode and photoanode, respectively:



2D material HJs have shown great potential in photoelectrocatalytic water splitting because of their special properties. One of the most promising 2D materials used for PEC water splitting is graphene, acting mostly as CT mediator or supporting matrix because of its electrical conductivity, excellent mechanical strength, large surface area and stability in a wide range of environments.

Other 2D materials that have been investigated for photoelectrocatalytic water splitting include TMDCs, which have tunable bandgap and strong light-matter interactions, thus showing excellent active charge carrier production and high

catalytic activity.³³ The formation of HJs composed of TMDCs is a promising strategy to improve the PEC activity, and there are some HJs designed for catalysing water splitting, like a triple W/WO₃/WS₂ HJ.⁴⁶ As the photoanode, the WO₃/WS₂ is able to separate charges, use the photogenerated holes for OER, while accumulating and transferring electrons to the W substrate and the counter electrode for HER. This HJ showed a photocurrent density of 5.6 mA/cm² at 1.23 V vs. Ag/AgCl, which was 7.2 times higher than pure 2D WO₃. Moreover, the WO₃/WS₂ HJ enhances the incident photocurrent efficiency (IPCE) by 55%, and the applied-bias photon-to-current conversion efficiency of the WO₃/WS₂ films was approximately

2.26% at 0.75 V (vs. Ag/AgCl), which is 9 times higher than pure WO₃.

In some cases, PEC water splitting can combine with other techniques to improve the reaction efficiency. For example, HJ photoelectrocatalysts can be used with ion membranes to facilitate the production of H₂ and O₂.²⁸ A ZnCr-LDH/g-C₃N₄ HJ was applied as a catalyst with an interlayer bipolar membrane to split water for HER and OER near each Pt electrode, while the remaining unreacted H⁺ and OH⁻ combine with Cl⁻ and Na⁺ respectively, and the cation-exchange and anion exchange membrane is permselective to specific ions (Figure 12a).

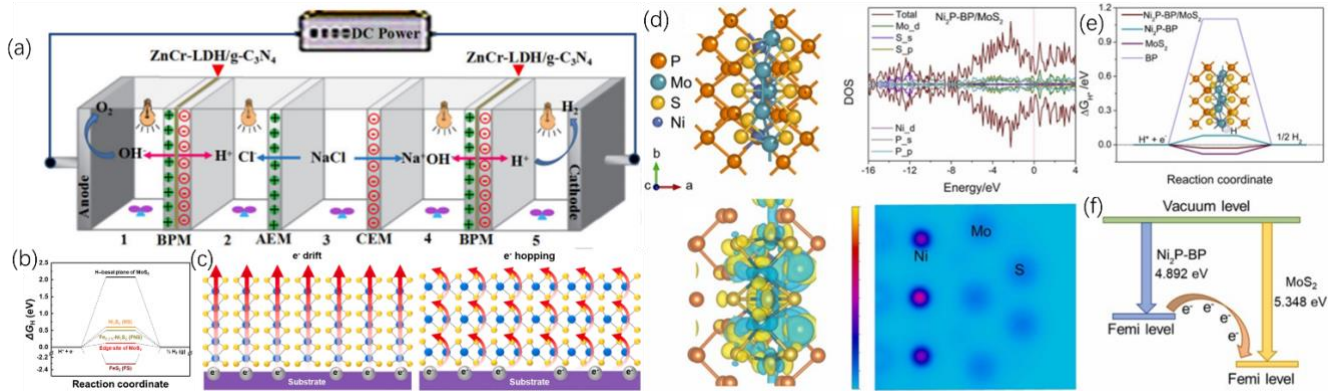


Figure 12. (a) Schematic diagram of photoelectrocatalytic water dissociation performance tests.²⁸ © 2017 Elsevier B.V. (b) Free-energy diagram of H adsorption on the site of each catalyst from DFT calculation. Schematics of (c) pristine MoS₂ and vertically aligned MoS₂.⁸⁶ © 2021 Elsevier B.V. (d) DFT calculation results: model, Bader charge distribution, density of states (DOS), and local electron state density distribution of the Ni₂P-BP/MoS₂ heterointerface, (e) ΔGH^* of BP, MoS₂, Ni₂P-BP, and the Ni₂P-BP/MoS₂ heterointerface. (f) Difference in the work functions of Ni₂P-BP and MoS₂. Reproduced with permission from ref.²⁰⁶

There are several reports focusing separately on catalysts for either HER or OER, since most photoelectrocatalysts are either oxidative or reductive. However, there are also catalysts which are active for both HER and OER. To design a proper catalyst for the whole water splitting process, one of the strategies is to build a *p-n* junction, to separate excited electrons and holes more efficiently and transfer them on different sites for HER and OER, separately. As mentioned before in Section 2.4.1, the 2D/1D BiOI/g-C₃N₄ HJ is able to gather holes on 2D BiOI and electrons on g-C₃N₄ nanotubes.⁵⁵ Thus, both the photogenerated charge carriers can be exploited, resulting in an enhanced PEC water splitting.

DFT calculations on CT efficiency in type II Cu₂O/g-C₃N₄ HJ⁹⁵ showed an enhanced hydrogen generation via photocatalytic and electrocatalytic water splitting reaction, which was induced by the transfer of photogenerated electrons from p-type Cu₂O to n-type g-C₃N₄. These DFT calculations focused on changes in the electronic structure upon adsorption of Cu₂O nanoparticle on g-C₃N₄ nanosheets. Although the Cu₂O (111) facet is stable, a surface reconstruction of outermost layer of Cu₂O was revealed using AIMD simulation. Moreover, two adsorbed g-C₃N₄ sheets suffered significant structural distortions because of the surface-bound bonding interactions between sp² hybridized N and Cu atoms. This structural deformation of g-C₃N₄ nanosheets is thought to be a crucial component in the enhanced catalytic activity of the HJs. Importantly, Bader electron charge analysis carried out after the HJ formation revealed the net electron transfer from the Cu₂O surface related

to the adsorption and limited electron tunnelling toward g-C₃N₄ sheets without direct contact with the Cu₂O surface.

DFT calculations with the HSE06 functional (on the PBE optimized geometries) were used to analyze the evolution of optoelectronic properties and high-frequency dielectric constant profiles of various 2D MoO_{3-x}S_x/MoS₂ HJs modified by chemical and physical approaches.²⁰⁷ This MoO₃/MoS₂ HJ is a type III (broken gap) HJ associated with a metallic character. Nevertheless, the DFT calculations proposed a strategy to tune the transitions from type III to type II band alignment of materials made of the 2D MoO_{3-x}S_x/MoS₂ HJ by exchanging the terminal oxo atoms of the MoO_{3-x}S_x single layer with sulfur shifting its CB position above the VB position of the MoS₂ single layer. Interestingly, at medium and high S-doping (>5%), the bandgap and CT of the MoS₂/MoO_{3-x}S_x HJ evolve continuously with the S concentration in the MoO_{3-x}S_x. At medium S-doping (9–10%), the 2D MoS_{0.28}O_{2.72}/MoS₂ HJ was identified as a potential PEC material for water splitting since it may generate a direct Z-scheme system due to the proximity of the CB of S-doped MoO₃ to the VB of MoS₂ (bandgap ~0.4 eV).

5.1.1 Hydrogen evolution reaction

HER in PEC involves the use of a photocathode to catalyze the reduction of H₂O into H₂ in the presence of light and bias. Theoretically, H⁺ needs to combine with electrons and change to H₂. Therefore, a photoelectrocatalyst with proper CB edge can provide sufficient electrons for the reaction. Meanwhile, the

bandgap of the catalyst should be as small as possible to absorb as wide a range of the solar spectrum as possible.

Different kinds of MCs have been reported as photoelectrocatalysts. Among them, MoS₂ has caught most of the attention as a component of HJs since its band position is suitable to convert UV and visible light to active charges and provide reaction active sites for HER.²⁰⁸ It is known that in the PEC of HER, the reaction active sites where the intermediates are adsorbed and reactions happens play a crucial role. The active sites of 2D layered materials in PEC of HER are typically located at the edges and defects of the material. This is because the edges and defects of 2D materials have higher energy states than the flat surface, which can provide sites for the adsorption and activation of reactant molecules. For instance, Paulraj et al. wrapped 2D MoS₂ on silicon nanowires, the photoelectrocatalytic results evidence the significant enhancement in performance of MoS₂/Si NWs based hybrid photocathode with ~300 mV vs. RHE, and the current density of -26.5 mA/cm² was achieved at the applied bias of 0 V vs. RHE.¹⁰⁶ This performance is also comparable with stable Pt/Si NWs photoelectrode. GaTe/ZnO HJ is designed similarly to ensure as many active sites are exposed to the reactants as possible.⁶⁴ In this HJ, the ZnO nanowires acted as the supporting framework for the favour layer-over-layer stacked growth of GaTe, which provided high surface area and high density of exposure edges for HER. The dark and photocathodic current reached -2 mA/cm² and -2.5 mA/cm² at -0.39 V vs RHE. High stability was indicated by the 20% decreased photocurrent density in 2 h. The hydrogen evolution rate was about 1.5 μmol/cm²/h, which is much higher than that obtained at the pristine ZnO nanowires.

Furthermore, the activation of basal plane of MoS₂ is another strategy to intensify the photoelectrocatalytic properties. Roy et al. report basal plane activation of MoS₂ by heterostructuring with 2D MoSe₂ for enhanced PEC of HER. MoS₂/MoSe₂ HJ grown on silicon nanowire (SiNW) array shows 1.2 times higher photocurrent density and 1.36 times higher incident IPCE than pristine MoS₂ grown on SiNW array along with 4.44 times higher H₂ evolution rate compared to pristine SiNW photocathode.²⁰⁹ Here, DFT calculations of heterostructure reveal that CT from the MoSe₂ layer to the basal plane of MoS₂ increases overall electron density resulting in its increased affinity towards proton reduction, which supports the experimental findings.

HJ containing vertically aligned MoS₂ was designed by introducing Ni₃S₂ and Fe doped Ni₃S₂ on the edge-terminated

surface of MoS₂ as well. The onset potentials of this photocathode markedly shifted toward the anodic direction to 280 mV, with photocurrent density at 0 V of -25.4 mA/cm². The significant decrease in Gibbs free energy at the interface between MoS₂ and Ni₃S₂ or Fe-doped Ni₃S₂ promotes robust proton reduction at the interface (Figure 12b). Moreover, the resistance is reduced dramatically at the HJs with vertically aligned MoS₂, indicating that the electrode-to-electrolyte shuttling of electrons on this HJ was the fastest among all the samples. This is because the movement of the electrons inside the 2D layers of MoS₂ is much faster than through the H-basal plane, as shown in Figure 12c.

However, recent reports find that the crystal defects can behave as electron traps to hinder the reaction efficiency, as the defects are the recombination center of the photogenerated charge carriers. By passivating the edge defects, the charge recombination is reduced, and the cathodic photocurrent increased dramatically; while the photocurrent increases even more after the sample was treated by pre-annealing and surface passivation to eliminate the internal and edge defects, respectively. These contradictions in the reaction mechanism encourage scientists to invest more attention on these directions to develop more efficient photoelectrocatalysts for HER.

For some 2D HJs, the photoelectrocatalytic property is optimized by tuning the amount ratio of each component. For instance, the 2D/2D BiVO₄/SnS₂ HJ with a 1:3 molar ratio exhibited dramatically higher current densities of 0.21 mA/cm² than the HJ with a 3:1 ratio (0.01 mA/cm²).⁶² However, the mechanism governing the components' ratio is still unknown and requires further investigations. A new 2D MC, VS_x, has been reported as a photoelectrocatalyst for HER as well.⁸⁰ VS_x/graphite HJ forms a flexible electrode functionalized as a photoelectrocatalyst for enhanced HER by visible and near-infrared light irradiation (overpotential ≈500 mV at the current density of -10 mA/cm²), in which graphite is a charge separator and mediator.

Transition metals such as Fe, Co, Ni and Mn, and their compounds have been proved active for electrocatalytic and photoelectrocatalytic HER. This is due to their partially filled d orbitals, allowing them to readily donate or accept electrons during the catalytic processes. The NiMn-LDH/g-C₃N₄ HJ can improve the HER performance by reducing the potential at -60 mA/cm² to -126 mV and Tafel slope to 50 mV/dec, thus boosting the PEC of HER dramatically. Similarly, using Co instead of Ni in the HJ also show promising PEC activity for HER, and the performance are listed in Table 2.²⁶

Table 2. Comparison of PEC HER activities for some state-of-the-art 2D-HJ related materials.

Catalyst	electrolyte	Light source	Current density	Tafel slope (mV/dec)	H ₂ production	Ref.
Nd-doped C₃N₄/BiOI	g- 0.5 Na ₂ SO ₄	M Air Mass, AM 1.5 G	15.5 mA/cm ² at -1.23 V vs. RHE	/	288 μmol/h/cm ²	53
Pt/MoS₂/TiO₂	0.5 H ₂ SO ₄	M 250 W Xenon lamp	-10 mA/cm ² at -74 mV vs RHE	30	/	83
BiOI/g-C₃N₄	1.0 M KOH	300 W Xe lamp	-0.23 mA/cm ² at -1 V vs. Ag/AgCl	/	/	55
GaTe/ZnO	0.1 Na ₂ SO ₄	M 300 W Xe lamp (λ > 420 nm), 100 mW cm ⁻²	-2 mA/cm ² at -0.39 V vs. RHE	/	1.5 μmol/h/cm ²	64

MoSe₂/Si	0.1 MH ₂ SO ₄		white LED			4.5 mA/cm ² at -1.0 V vs Ag/AgCl	/	/	210
SmV/g-C₃N₄	0.5 H ₂ SO ₄	M	400 W Xe light			-10 mA/cm ² at -200 mV vs RHE	63	/	43
1T/2H MoS₂	0.5 Na ₂ SO ₄	M	visible light			-1.4 mA/cm ² at -0.6 V vs. Ag/AgCl		/	18
MoS₂ nanoribbons	0.5 H ₂ SO ₄	M	405 nm LED, 140 μW/cm ²			-10 mA/cm ² at -280 mV vs RHE	124	/	211
MoS₂/Si	0.5 Na ₂ SO ₄	M	He-Ne lamp 100 mW/cm ²			-33 mA/cm ² at -0.3 V vs. RHE	34	/	106
BiVO₄/GQD/g-C₃N₄	Lake water		500 W halogen lamp			19.2 mA/cm ² at 1.0 V vs Ag/AgCl	/	84.9 mmol/h/cm ²	56
BiVO₄/SnS₂	0.5 Na ₂ SO ₄	M	solar simulator, 100 mW/cm ²			0.21 mA/cm ² at 1.23 V vs RHE	/	~21 μmol/sec/cm ²	62
RGO/g-C₃N₄/BiVO₄	0.5 Na ₂ SO ₄	M	500 W halogen lamp, 100 mW.cm ⁻²			14.44 mA/cm ² at 1.0 V vs Ag/AgCl	/	63.5 mmol/h/cm ²	47
P/g-C₃N₄	0.1 Na ₂ SO ₄	M				202 μA/cm ² at -1 V vs. Ag/AgCl	/	/	57
MoS₂/TiO₂	0.5 H ₂ SO ₄	M	300 W Xenon lamp			10 mA/cm ² at -320 mV	135	/	90

The decoration of small number of noble metals has become a strategy to improve catalytic properties of 2D HJs. For instance, the MoS₂/TiO₂ HJ can be used as photoelectrocatalyst for HER and the onset potential is -215 mV, and the Tafel slope is 92 mV/dec.⁸³ The performance can be strongly improved by decorating Pt nanoparticles on the surface of MoS₂ to form more effective reaction active sites. Specifically, the onset potential is reduced to -9 mV vs. RHE, which is dramatically lower than the benchmark Pt/C (-48 mV vs. RHE under the same experimental conditions). Meanwhile, the Tafel slope decreased from 92 mV/dec to 30 mV/dec with the addition of Pt, revealing faster kinetics by using Pt as catalyst and MoS₂/TiO₂ HJ as charge mediator.

In some reports, the HJs are not directly used as photocathode for HER, but to separate and migrate the charge, while the counter electrode collects the electrons for HER. In the work of Samsudin et al., the BiVO₄/rGO/g-C₃N₄ is the photoanode to separate and migrate photogenerated electrons to the cathode for HER, while the production of H₂ is on the Pt counter electrode.⁵⁶ To quantify the yield of H₂, the gas analyzer was applied. The high photoelectrochemical hydrogen production of 63.5 mmol/h demonstrated by this HJ exceeds the pure BiVO₄ (9.5 mmol/h) and g-C₃N₄ (11.9 mmol/h), implying that the rGO serves as an excellent electron mediator for the reduction process which lowers the photocatalytic overpotential and minimizes the photocharge carrier recombination. Similarly, h-MoO₃/1T-MoS₂ HJ is used as photoanode to generate active electrons for HER as well.⁸⁸ There are more other HJs reported as an indirect photoelectrocatalysts, which are listed in Table 2.

Although pristine MXenes show unsatisfactory catalytic activity, phosphorus and oxygen modified Mo₂CT_x MXenes appear to be different class of promising HER photocatalysts.²¹² Using the CHE method, Qu et al. observed that MXenes doped with non-metals possess a metallic band structure and an optimal value of ΔG_{H*}, which lead to improved conductivity and electrocatalytic kinetics, respectively.²¹² Interestingly, both

O and P needed to be present in the model, otherwise the resulting ΔG_{H*} value would be too negative, restraining the adsorbed hydrogen escaping from the surface. Doping of Ti₃C₂T_x MXenes by nitrogen atoms was also found advantageous for HER.²¹³ Ti₃C₂T_x MXene used as an efficient solid support to host a N and S coordinated ruthenium single atom (RuSA) catalyst was demonstrated to display superior activity toward the HER.²¹⁴ The model of RuSA/N/S/Ti₃C₂T_x catalyst was constructed based on XPS and XAFS results, and DFT calculations employing CHE method. partial density of states and total density of states analyses revealed that the coordination interaction of RuSA altered the electronic structure of the Ti₃C₂T_x support while achieving an optimal ΔG_{H*} close to zero.

An enhancement in HER performance under UV illumination was found for pristine 2D BiOBr and the 1% MoS₂/BiOBr vdWs HJ, with the latter showing better catalytic performance and stability than the former.¹³⁹ DFT calculations revealed that excellent properties of 1% MoS₂/BiOBr may be attributed to an optimal distribution of MoS₂ nanosheets among 2D BiOBr layers, as was revealed by total and partial density of state (DOS) analysis. The CT analysis demonstrated that an almost constant number of ~0.35 electrons was transferred from BiOBr to MoS₂. DFT calculations also proved that the holes photogenerated in BiOBr can remain in BiOBr or be partially transferred on the surface of MoS₂. Overall, it was concluded that the system can be considered a Type-I HJ, in which a formal energy transfer process takes place from BiOBr to MoS₂ following photoexcitation of the former through a charge exchange mechanism.

Another novel dual in-plane/out-of-plane Ni₂P-black phosphorus (BP)/MoS₂ HJ (Figure 12d-f) was found to be a promising catalyst for HER.²⁰⁶ Here, the DFT calculations with PBE functional and vdWs corrections verified that the work function difference at this Mott-Schottky interface caused an electron transfer from Ni₂P-BP to the outer-surface MoS₂, which boosts the HER process. This was demonstrated by

Bader charge and DOS analysis. As such, the Ni₂P-BP/MoS₂ heterostructure presents almost zero ΔG_{H^*} (-0.03 eV), indicating superior HER activity beyond the counterparts (MoS₂, BP, and Ni₂P-BP).²⁰⁶ Hydrogen was found to be preferentially adsorbed on the S atom of the Ni₂P-BP/MoS₂ HJ. Moreover, ultrasmall NiSe/WSe₂@NC HJ exhibited an enhanced alkaline HER.²¹⁵ All calculations were carried out by spin-polarized DFT. Changes in Gibbs free energy were calculated by the CHE model. The calculated work function of WSe₂ of 5.67 eV was higher than that of NiSe (4.84 eV). Consequently, the contact potential at the NiSe/WSe₂ interface could induce a built-in electric field, resulting in electron transfer from NiSe to WSe₂. In accordance, the charge density difference analysis showed that 1.83 e⁻ are transferred from NiSe to WSe₂, resulting in the electron accumulation on WSe₂, favoring the water dissociation energies, and electron depletion on NiSe, being beneficial for the release of H₂. Moreover, the calculated adsorption energy of water on NiSe/WSe₂ was presented to be suitable adsorption energy at W sites (-1.07 eV), and the ΔG_{H^*} at Ni sites is as low as 0.37 eV, which are superior to those of both single NiSe and WSe₂ surfaces.

2D HJs InSe nanosheets modified with Au nanoparticles, where Au atoms are adsorbed on the hollow site of the InSe nanosheet, also achieved the theoretical enhancement of the HER performance comparing to the not-modified InSe nanosheets.²¹⁶ Here, the DFT calculation of the band structure revealed that Au nanoparticles can improve the conductivity of InSe nanosheets after the Au adsorption, as the indirect band semiconductor, with a gap of approximately 1.36 eV, is changed to metal after the formation of the heterojunction. Moreover, charge density distribution analysis demonstrated that the adsorption of Au induces the formation of Au–Se CT channels with ionic bond characteristics. This feature can not only inject free electrons on the surface of Au ions into the InSe nanosheet to improve its conductivity but also serves as a CT channel for the HER process. Additionally, the calculated ΔG_{H^*} of the HER process changed from 1.72 eV for InSe nanosheets to -0.59 eV for InSe/Au HJ, confirming that the formation of the HJ optimizes the hydrogen adsorption/desorption kinetics process, effectively improving the HER performance.

5.1.2 OER

OER is the other half reaction of water splitting. It occurs on the photoanode, which requires the active holes to oxidize hydroxyl species and produce O₂. Thus, a photoelectrocatalyst which can accumulate and release holes to the reactants is required.

g-C₃N₄ 2D HJs are commonly used as a photoelectrocatalyst for OER. Among them, the TiO₂/g-C₃N₄ HJ is the most reported because of its flexibility of synthesis, good energy conversion ability and the excellent stability of TiO₂. g-C₃N₄ is the catalyst for OER considering the band alignment of the two

components. For example, Murugan et al. combine g-C₃N₄ with TiO₂ to prepare a type II HJ, in which g-C₃N₄ absorbs the incident photons and excites the electrons between the frontier orbitals, while TiO₂ attracts the excited electrons to hinder the charge recombination.³⁹ As such, the HJ with 20 wt% of g-C₃N₄ exhibits 1.4 and 595 folds of OER efficiency than the bare components, respectively. Rajaiatha et al. obtained a similar HJ with a simple wet chemical synthesis method and found that this photoanode yields a maximum efficiency of $\sim 0.072\%$, which is twofold higher than bare TiO₂ (0.035%).³⁸ Moreover, g-C₃N₄/BiOI photoanode was able to generate a photocurrent density as high as 0.70 mA/cm². This 50% increase in photoresponse over the pristine, low bandgap BiOI films indicates the superior charge separation ability of the HJ.⁴² Besides, it displayed almost no loss in photoelectrochemical performance and did not suffer damage to their structure and optical properties due to reuse, which bodes well for their long-term operational stability and durability.

HJs containing MoS₂ are widely used in PEC of OER as well. The VB edges of monolayer MoS₂ are more positive than the oxidation potential of water, which means 2D MoS₂ could be used as catalyst for PEC of OER.²¹⁷ However, the pure MoS₂ suffers from fast charge recombination which inhibits its usage for OER. Therefore, a variety of MoS₂ HJs are fabricated for efficient charge separation and enhanced OER performance. For instance, the combination of MoS₂ and α -Fe₂O₃ can change the band structure of the catalyst and separate the photo-generated charges more efficiently.⁴⁴ As shown in Figure 13a, the band bending achieved equilibrium of the Fermi level when MoS₂ is in contact with α -Fe₂O₃ in the p-n junction. Following visible light illumination, the photo-generated electrons were transferred from the CB of MoS₂ to the CB of α -Fe₂O₃. The holes were simultaneously driven by the electrostatic field from the VB of α -Fe₂O₃ to the VB of MoS₂, and they reacted with •OH to generate O₂. Vertical MoS₂ NSs-decorated WO₃ nanorods possessed an enlarged surface area, improved light absorption performance, and appropriately organized the staggered HJ of MoS₂/WO₃ for promoting the PEC reaction, showing a 72% enhancement in PEC performance compared to pristine WO₃. The photoanode with 3D BiVO₄ grown on 2D WO₃ underlayer displays a photocurrent of 2.55 mA/cm² at 1.23 V vs. RHE as well.⁷⁰ Moreover, the onset potential of the 2D/3D WO₃/BiVO₄ photoanode is shifted to 300 mV comparing to the pristine BiVO₄, ensuring lower voltage requirements for PEC of OER. MoS₂/WS₂ monolayers can form a type II HJ with matching crystal lattice parameters, allowing for ultrafast CT and separation between the discrete materials. Sherrel et al. synthesized the MoS₂/WS₂ HJ on Au substrate, reaching an IPCE of $\sim 1.6\%$ and a visible-light-driven photocurrent density of 1.7 mA/cm² (at 1.19 V vs RHE) for OER (Figure 13b).

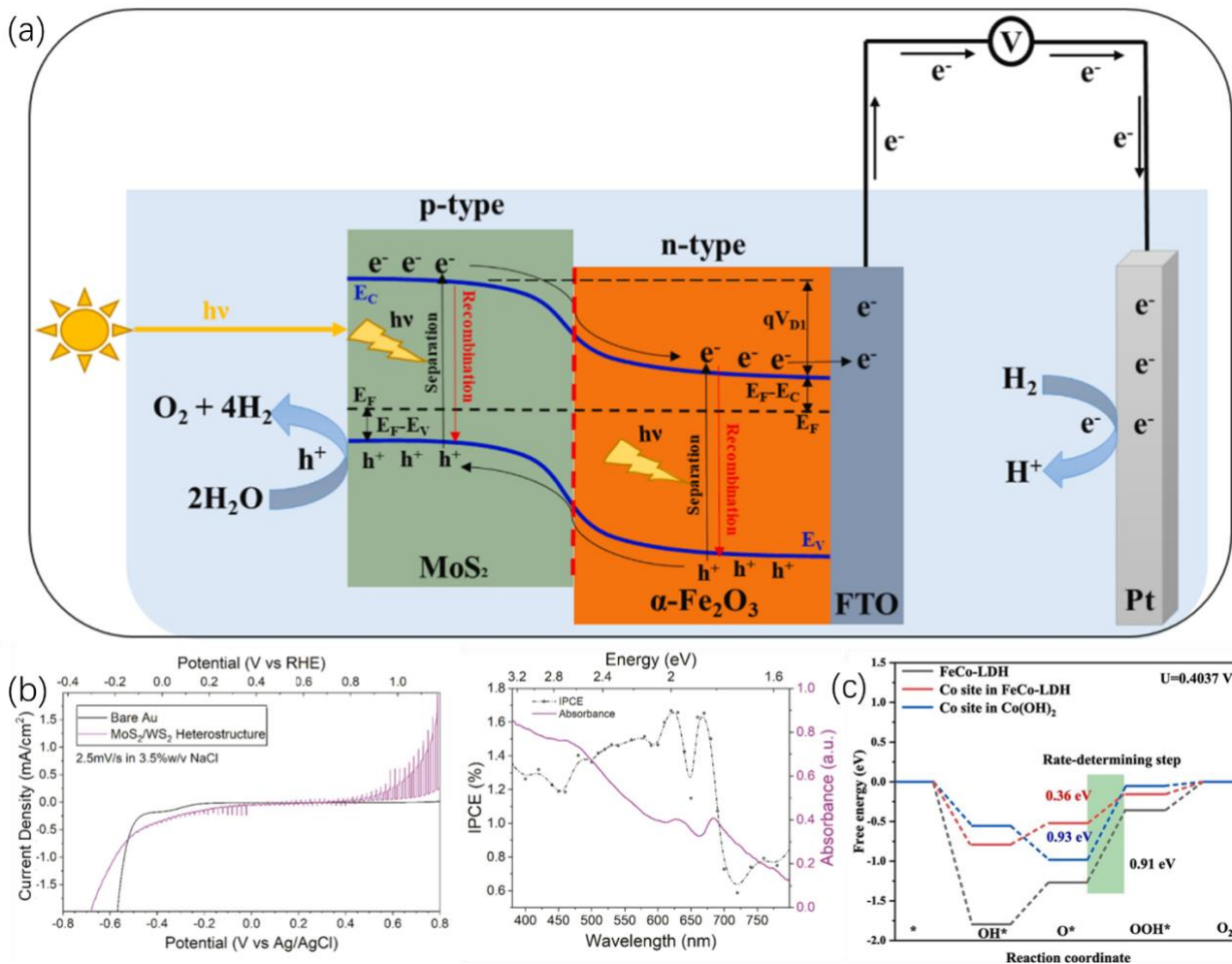


Figure 13. (a) Mechanism for the p–n HJ of $\alpha\text{-Fe}_2\text{O}_3/\text{MoS}_2$.⁴⁴ © 2020 The Author(s). Published by Elsevier B.V. (b) Linear sweep voltammetry at 2.5 mV/s from +0.8 to –0.8 V vs Ag/AgCl, demonstrating the complete protection of the Au surface as minimal noble-metal hydrogen evolution is observed and a negligible contribution of the substrate to either dark or photocurrent in the water oxidation region occurred. Photocurrent dependence on monochromatic light at +0.75 V vs Ag/AgCl and corresponding absorbance spectra of the heterostructures dispersed via sonication in ethanol.⁷⁷ © 2019 American Chemical Society. (c) Adsorption free energy of FeCo-LDH and FeCo-LDH@Co(OH)₂ (with Co site in Co(OH)₂ and FeCo-LDH) electrocatalysts for OER.²¹⁸ © 2023 Elsevier B.V.

The construction of HJs with MoS₂ and materials with metallic properties like Sn_xMo_{1-x}S₂ is helpful for the enhancement of the charge separation and transfer.⁸¹ The Sn_xMo_{1-x}S₂/MoS₂ interface can effectively eliminate the Fermi level pinning effect and minimize the contact resistance, therefore ensuring electron transfer through Sn_xMo_{1-x}S₂ to the counter electrode, while the photogenerated holes participate in OER on the photoanode, improving the photoelectrocatalytic performance by 2.5 times.

Besides, the thin layer of 2D MoS₂ on the surface of BiVO₄ dramatically increases the photocurrent density in the range of 0.6–1.8 V vs. RHE²¹⁹. This is mainly because MoS₂ provides the reaction active sites from OER, as the pure BiVO₄ shows

negligible photocurrent in the range of 0.6–1.8 V. vs. RHE, since it is probably a charge mediator in the PEC.

LDHs containing Fe, Co and Ni are largely studied as electrocatalysts for OER because of the intrinsic properties of Fe, Co and Ni. Therefore, these compounds are combined with other photoelectrocatalysts for more efficient OER. For instance, $\alpha\text{-Fe}_2\text{O}_3/\text{Ni}_{0.5}\text{Fe}_{0.5}\text{-LDH}$ photoelectrode exhibits a negative shift of onset potential compared with pure $\alpha\text{-Fe}_2\text{O}_3$, suggesting a boost in the HJs kinetics for OER.¹⁹ CoMn-LDH shows photocurrent for OER as well, and the catalytic property can be enhanced by adding 10 wt% of g-C₃N₄.²⁶ A comparison of the photoelectrocatalytic properties of different photoelectrocatalysts is listed in Table 3.

Table 3. Comparison of PEC OER activities for some state-of-the-art 2D-HJ related materials.

Catalyst	electrolyte	Light source	Current density	Efficiency	Ref.
MoS ₂ /WO ₃		AM 1.5 illumination	1.12 mA/cm ² at 0.8 V vs. Hg ₂ /Hg ₂ Cl ₂	photoconversion efficiency at 0.8 V: 0.52%	107

$\text{Sn}_x\text{Mo}_{1-x}\text{S}_2/\text{MoS}_2$	0.5M Na ₂ SO ₄	300 W Xe lamp (100 mW cm ⁻²)	> 0.8 mA/cm ² at 1.23 V vs RHE	/
BiOI/g-C₃N₄	1.0 M KOH	300 W Xe lamp	81.5 $\mu\text{A}/\text{cm}^2$ at -1 V vs. Ag/AgCl	55
g-C₃N₄/TiO₂	1 M KOH	100 mW cm ⁻² (AM 1.5 G)	72.3 $\mu\text{A}/\text{cm}^2$ at 1.23 V vs RHE	applied bias photon-to-current efficiency ~0.028% ³⁹

PH-dependent M_kM was used to evaluate the relative performance of 12 different transition metal catalysts embedded in fourfold N-substituted double carbon vacancies in graphene for OER.²²⁰ It is revealed that the used methodology to calculate the reaction pathways led to the results with enhanced catalytic activity when compared to purely thermodynamics-based predictions, which underestimated an onset potentials. The reason is that the catalytic reaction pathways performed on graphene-based catalysts are naturally also influenced by features such as metal site coverage, etc.

Ultra-thin FeCo-LDH@Co(OH)₂ HJ is found to have many surface exposed active sites, which resulted in enhanced catalytic activity for the OER, and the spin-polarized DFT calculations were helpful to reveal the reaction rate determining step (RDS).²¹⁸ The absorption Gibbs free energies of OH*, O*, and OOH* were calculated on different Co active site. The RDS of both FeCo-LDH and the FeCo-LDH@Co(OH)₂ HJ (different Co sites) was found to be the third step of the process in which O* generates OOH* (Figure 13c). These calculations also indicated that the interfacial cooperation between the electrons from FeCo-LDH and Co(OH)₂ effectively regulated the adsorption strength of intermediates on the HJ and reduced the barrier of RDS in the OER process. Interestingly, the real active site of was described to be the Co site.

5.2 Organic detoxification

Organic pollutants can be harmful to the environment, particularly if they enter waterways and affect aquatic life. PEC organic detoxification is a useful process for removing organic pollutants from wastewater and other industrial effluents. By applying light and electricity as the reaction power source, PEC can be a cost-effective method compared to the traditional methods like chemical oxidation or biological treatment. It can also be combined with other treatment methods to further increase the efficiency of the overall treatment process. As a versatile method for wastewater treatment, PEC organic degradation can be used to treat a wide range of organics, including pharmaceuticals, dyes and pesticides. As shown in Figure 14a, both the photogenerated electrons and holes can be used indirectly or directly for organic degradation, since the organic pollutants are mainly decomposed into non-toxic species by oxidation reaction. The excited electrons can react with O₂ and form $\cdot\text{O}_2^-$, which is a powerful oxidant to degrade organic molecules. Meanwhile the holes can be directly used to oxidize OH⁻ and H₂O into $\cdot\text{OH}$, which can be used for the removal of pollutants. These free radicals can oxidize most of the organic pollutants regardless of their nature. Usually, organic pollutants can be degraded totally into inorganic non-toxic molecules or changed into other non-toxic or value-added commodity organic molecules, depending on the types of the active species and specific reactions.

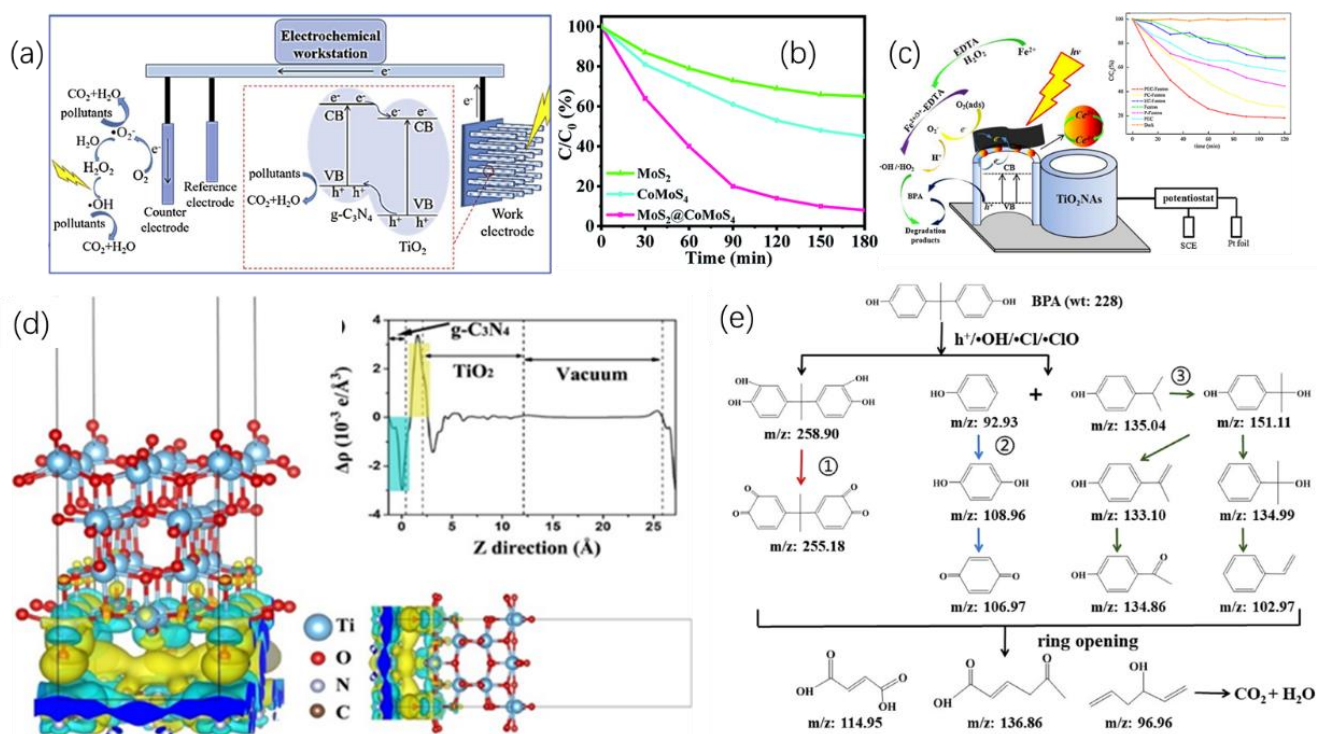


Figure 14. (a) Schematic of photoelectrocatalytic degradation of organic pollutants.⁴⁰ © 2019 Elsevier B.V. (b) the PEC activities of MoS₂, CoMoS₄ and MoS₂/CoMoS₄.⁷⁴ © The Royal Society of Chemistry 2020. (c) Schematic diagrams for PEC degradation towards Bisphenol A (BPA) using rGO/CeO₂/TiO₂.⁴⁹ © 2016 Elsevier Ltd. (d) The side view of the charge density difference for 2D TiO₂/g-

C₃N₄; Planar-averaged electron density difference $\Delta\rho(z)$ for 2D TiO₂/g-C₃N₄. The cyan and yellow areas indicate electron depletion and accumulation, respectively.⁴¹ © 2019 Elsevier Inc. (e) Proposed pathway of BPA photoelectrocatalytic degradation over MoS₂/BiVO₄ photoanode under visible light illumination.¹⁰⁸ © 2020 Elsevier Ltd.

Tetracycline (TC), lomefloxacin (LOM), and p-nitrophenol (PNP) are common antibacterial agents or precursors for medicines and can influence the microorganisms once released to nature. Therefore, there is plenty of work focused on the detoxification of these organics by PEC. In most cases, the photocatalytic oxidation is incomplete, and the final products are still organic molecules presenting lower toxicity. For instance, TC can be photoelectrocatalytic oxidized by

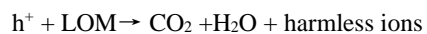
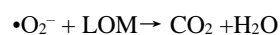
rGO/AgCl⁴⁸ and BiOI/BiPO₄,⁴⁵ though the final product is not CO₂ and H₂O. The ratio of the HJ components has an optimized value, meaning that either materials can inhibit the PEC degradation efficiency.⁴⁵ The comparison of performance of these catalysts are listed in Table 4. Considering the complexity of the final products from PEC degradation of pharmaceuticals, it is more reasonable to evaluate the toxicity of all the products than quantify all the products after PEC.

Table 4. Comparison of photoelectrocatalytic degradation of organics for some state-of-the-art 2D-HJ related materials.

Catalyst	Pollutants	Conditions	Degradation efficiency	Ref.
g-C ₃ N ₄ / Ag ₃ PO ₄	RhB	[RhB] 10 ppm [NaCl] 0.01 M J = 10 mA cm ⁻²	99% in 30 min	54
GO/Ag ₃ PO ₄ /Ni	RhB	[RhB] = 5 ppm 0.1 M Na ₂ SO ₄ Xenon lamp E = 0.6 V	97 % in 18 min	14
rGO/AgCl	TC	[TC] = 20 mg/L 0.5 M Na ₂ SO ₄ E = 1.5 V (vs Ag/AgCl). Visible light	85.2% in 120 min	48
TiO ₂ /g-C ₃ N ₄	TC	10 mg/L 0.1 M Na ₂ SO ₄ Xenon lamp 1 V vs. Ag/AgCl	100% in 120 min	40
Co ₃ O ₄ /g-C ₃ N ₄	Reactive brilliant blue KN-R	C = 60 mg/L 0.1 mol/L Na ₂ SO ₄ Xenon lamp J = 0.01 μ A cm ⁻²	91.4% in 120 min	13
CQD/g-C ₃ N ₄	Methylene blue (MB)	5 ppm 0.1 M Na ₂ SO ₄ xenon lamp E = 1.5 V	97.21% in 3 h	58
Ti ₃ C ₂ T _x /Bi ₁₂ TiO ₂₀	MB	10 mg/L 0.5 M Na ₂ SO ₄ xenon lamp E = 1V	85.4% in 120 min	65
BiOBr/TiO ₂	RhB	xenon lamp 10 mg/L Rh.B mol/L NaCl E = 0.3 V	60% in 100 min	69
Al ₂ O ₃ /SnS ₂	MB	10 mg/l xenon lamp 0.5 M Na ₂ SO ₄ E = 0.49 V (vs. Ag/AgCl)	85.9% in 3 h	76

Pt/g-C₃N₄/CdS	MB	5 mg L ⁻¹) E = 0.6 V Xe arc lamp	60% in 2 h	16
C/g-C₃N₄	MB	10 ⁻⁶ g/mL 0.1 M KOH white light LED E = 1.5 V vs RHE	90% in 25 min	59
CQD/g-C₃N₄	phenol	5 ppm 150 mg/mL Na ₂ SO ₄ xenon lamp E=1.5 V	51.6% in 3 h	58
BiOI/BiPO₄	TC	0.1 mol/L Na ₂ SO ₄ 10 ppm Xenon lamp E=1.2 V	77% in 250 min	45
MoS₂/BiVO₄	BPA	0.1 M of NaCl 10 ppm Xenon lamp E=1.5 V	100% in 75 min	108
CQDs/g-C₃N₄	MB	0.1 M Na ₂ SO ₄ MB: 5 ppm Xe lamp E=1 V	100% in 180 min	58
Au-WS₂	phenol	50 mg L ⁻¹ phenol 1 M Na ₂ SO ₄ Xenon lamp Cyclic voltammetry (CV): 0-1.0 V	100% in 70 min	63
Ni /NiFe-LDH/Co₃O₄	BPA	10 mg/L 0.1 M Na ₂ SO ₄ Xenon lamp E = 0.7 V	100% in 120 min	32
g-C₃N₄/TiO₂	TC	C0 = 10 mg/L, 0.1 M Na ₂ SO ₄ Xe lamp E=1.0 V vs. Ag/AgCl	100% in 120 min	40
g-C₃N₄/α-Fe₂O₃	PNP	10 mg/L 0.2 M Na ₂ SO ₄ Xe lamp E = 1.5 V	83.5% in 150 min	61
RGO-CeO₂-TiO₂	BPA	10 mg L ⁻¹ 0.05 M Na ₂ SO ₄ Xe lamp	80% in 120 min	49

Zhang et al. use the MoS₂/CoMoS₄ HJ to perform LOM degradation.⁷⁴ The electrons accumulated on the CB of MoS react with O₂ to form •O₂⁻, which is a strong oxidant for LOM degradation. Simultaneously, the photogenerated holes are left on the VB of CoMoS₄ to enhance the PEC degradation efficiency of LOM. The reaction equations can be proposed as follows:



Eventually, 79% of LOM was degraded in 180 min with MoS₂/MoMoS₄ as photoanode (Figure 14b).

As to the PEC of PNP degradation, the photogenerated electrons can combine with toxic PNP and convert it to less

toxic p-aminophenol (PAP), which is an organic intermediate to produce various medicines, dyes, antioxidants and oil additives.

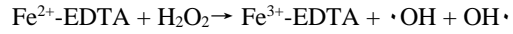
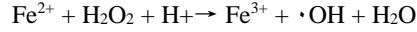
Total degradation of the PNP into N₂, NO, CO₂ and H₂O is performed by g-C₃N₄/α-Fe₂O₃ HJ along both oxidation and reduction pathways.⁶¹ The presence of the HJ improves the CT efficiency, as proved by the photocurrent density and the resistance. At the optimum experiment conditions at PAP initial concentration of 10 mg/L, pH value of 6.1, electrolyte concentration of 0.2 mol/L, and bias voltage of 1.5 V, the optimized photoanode displayed the highest PNP removal rate, which results from the synergistic effect of photocatalysis and electrocatalysis.

As a group of typical organic pollutants, dyes are widely used in the textile, paper, and leather industries, and present in wastewater from these industries. They are often resistant to conventional treatment methods and can persist in the environment for a long time, leading to environmental pollution and health hazards. To eliminate them efficiently, methods including PEC have been developed. The mechanism of dye degradation is like the degradation of other organics. Theoretically, both the active electrons and holes can join the PEC of dye by reacting with water and oxygen to produce reactive oxygen species (ROS). Different kinds of dyes are used for PEC degradation by 2D HJs, such as RhB, reactive brilliant blue KN-R, MB, phenol et al. Table 4 reports the photoelectrocatalytic activities for some state-of-the-art catalysts.

Bisphenol A (BPA) is a common chemical compound primarily used in the manufacturing of various plastics. It has been linked to a variety of health problems, including reproductive and developmental disorders, diabetes, cardiovascular disease, and certain cancers. BPA pollution can occur through a variety of sources, including industrial wastewater discharges, leaching from plastic products and packaging, and landfill leachate. It can also be found in food and drinking water due to its use in the production of food packaging, can linings, and water bottles. Therefore, this compound has become one of the targets to be removed by PEC. TiO₂ is commonly used as catalyst for this reaction. However, its catalytic efficiency is low due to its poor conductivity, unexpected recombination of photoinduced charges, and broad bandgap (3.2 eV). Therefore, 2D materials/TiO₂ HJs are designed to reinforce the PEC efficiency. For example, TiO₂/g-C₃N₄ is prepared for the photodegradation of BPA.⁴¹ Its composition reduces internal resistance and enhances the electrocatalytic conductivity compared to the pristine components. The TiO₂/g-C₃N₄/carbon fiber electrode exhibits a higher PEC activity, with reaction rates of 1.7, 2.5, and 3 times faster than that of g-C₃N₄, TiO₂, and commercial P25, respectively. DFT calculations with PBE functional suggested that the generated interface HJ of 2D TiO₂/g-C₃N₄ can provide quick charge separation and transfer via both Ti–N and C–O bridges, resulting in a prepared catalyst that can facilitate the effective separation and transportation of photoinduced electron-hole pairs.⁴¹ The redistribution of charges mostly took place at the 2D TiO₂/g-C₃N₄ interface region, largely because of the weak vdW interaction between TiO₂ and g-C₃N₄ (Figure 14d). Additionally, the results indicated that electrons move from g-C₃N₄ to the TiO₂ slab at the 2D TiO₂-g-C₃N₄ interface.

rGO/CeO₂/TiO₂ HJ is used for the PEC degradation of BPA as well, while the efficiency rate is only 40%. Fenton oxidation is

reported helpful in increasing the amount of ROS, and the following formulas explain how the Fenton oxidation generate ROS continuously:



As shown in figure 14c, with the combination of PEC and Fenton oxidation, the degradation rate reaches 81.8% in 120 min, meanwhile the kinetics is improved from 0.0045 min⁻¹ to 0.0146 min⁻¹, indicating a synergetic effect between Fenton and PEC process (Figure 14e).

This type of electrolyte can influence the photoelectrocatalytic degradation of BPA as well. By using 100 mM of NaCl as the supporting electrolyte, 10 ppm of BPA could be completely degraded in 75 min by MoS₂/BiVO₄ photoanode, with a bias of 1.5 V vs. Ag/AgCl. This is because chloride anions can be activated by photogenerated holes to form chlorine oxide radical (•ClO), which plays a dominant role in the degradation of BPA. NiFe-LDH/Co₃O₄ HJ is reported to exhibit 100% removal rate of BPA of 10 mg/L in 120 min under visible light illumination.³²

4.3 CO₂ reduction reaction

Valorization of CO₂ by converting it into value add-products and fuels is one of the leading scientific challenges to face the effects of global warming. PEC is one of the most promising techniques, along with photocatalysis, electrocatalysis, or thermocatalysis, capable of transforming carbon dioxide into useful products.²²¹ PEC for CO₂ reduction is usually performed in organic media due to the good solubility of CO₂. However, in order to have an easier scale-up application and lower cost, aqueous media is still the first choice for PEC of CO₂RR.³ However, in water it is important to take into account the HER competitive process. Half reduction reactions in Table 5 below show the main reduction of products that can be obtained from CO₂RR.³

Table 5. Electrochemical reduction potentials evaluated in an aqueous solution at pH = 7 vs. standard hydrogen electrode (SHE).

Reaction	E ₀ vs SHE (V)
CO ₂ + e ⁻ → CO ₂ ^{•-}	-1.850
CO ₂ + 2H ⁺ + 2e ⁻ → CO + H ₂ O	-0.665
CO ₂ + 2H ⁺ + 2e ⁻ → HCO ₂ H	-0.521
CO ₂ + 4H ⁺ + 4e ⁻ → HCHO + H ₂ O	-0.485
CO ₂ + 6H ⁺ + 6e ⁻ → CH ₃ OH + H ₂ O	-0.399
CO ₂ + 8H ⁺ + 8e ⁻ → CH ₄ + 2H ₂ O	-0.246
2CO ₂ + 12H ⁺ + 12e ⁻ → C ₂ H ₄ + 4H ₂ O	-0.349
2CO ₂ + 12H ⁺ + 12e ⁻ → C ₂ H ₅ OH + 3H ₂ O	-0.329
2CO ₂ + 14H ⁺ + 14e ⁻ → C ₂ H ₆ + 4H ₂ O	-0.270
3CO ₂ + 18H ⁺ + 18e ⁻ → C ₃ H ₇ OH + 5H ₂ O	-0.310
2H ⁺ + 2e ⁻ → H ₂	-0.414

Usually, CO and formate are the main products since they require 2 electrons in the process. However, since thermodynamically the reduction potentials have similar

values, product selectivity has to be controlled as best as possible by tuning the system properly.²²² Moreover, CO₂ adsorption on the material surface is a key step in the general CO₂ conversion efficiency. In this regard, thanks to the numerous surface active sites and the tunable electronic properties, 2D HJs have been studied with increasing effort.²²³ Currently, the production of C₂ compounds such as alcohols and ethylene has become an important direction in the field of CO₂RR, but the study of 2D HJs photoelectrocatalysts is still poor both theoretically and experimentally.

One of the most promising 2D materials for CO₂RR is g-C₃N₄, Zhu et al. demonstrated how CO₂ molecules have better adsorption on 2D monolayer compared to the bulk g-C₃N₄. Thanks to DFT calculation it was possible also to show how the adsorption is favored on two coordinated N atoms.²²⁴ In order to increase the catalytic performance of g-C₃N₄, Wang et al. inserted S atoms into the g-C₃N₄ structure, showing a reduction of the bandgap and an increased photogeneration of charge carriers thanks to the presence of the impurity states.²²⁵ Sagara et al. combined B atoms with g-C₃N₄, showing a 5 times increase in the photocurrent compared to the undoped g-C₃N₄ (Figure 15a).⁹¹ In the same work, the addition of a co-catalyst on the surface of the semiconductor in the form of gold nanoparticles, further increased the selectivity toward a specific product (ethanol) and the catalytic activity (Figure 15b). More HJs for PEC of CO₂RR have been reported as a theoretical

model. For instance, BiOCl/g-C₃N₄ is constructed for DFT calculations of Gibbs free energy (Figure 15c).⁹⁶ The comparison of the calculated Gibbs free energy for the CO₂RR to CO on the surface of ns-CN, p-BiOCl/ns-CN, OV_s-BiOCl/ns-CN, and OV_s-BiOCl/ns-CN reveal that for all systems, *CO₂ + H⁺ + e⁻ → *COOH is a RDS. Importantly, it was described that O vacancies and N vacancies in the BiOCl and ns-CN, respectively, in the HJ led to the lowest energy barrier. Although the formation of the heterojunction from BiOCl nanosheets with 2D g-C₃N₄ with vacancies seems to be promising for PEC, the adsorbed CO molecules have difficulty forming the final products involved with more than two-electron processes as the free energy change of *CO is negative, hence *CO is desorbed from the catalyst surface as the final product.

Another class of 2D materials studied for CO₂RR is the TMDs. Hong et al. worked on a simple system using MoS₂ and MoSe₂ thin film on silica substrates showing an increase of current density shining light on the photoelectrodes, where MoSe₂ has the best performance (Figure 15d).²²⁶ Hu et al. investigated on MoS₂ nanosheets loaded on SnO₂ nanoparticles as a photocathode.²²⁷ It was discovered that a 5% loading of MoS₂ is the best for increasing the catalytic activity in terms of faradic efficiency and current density, with respect to the bare SnO₂.

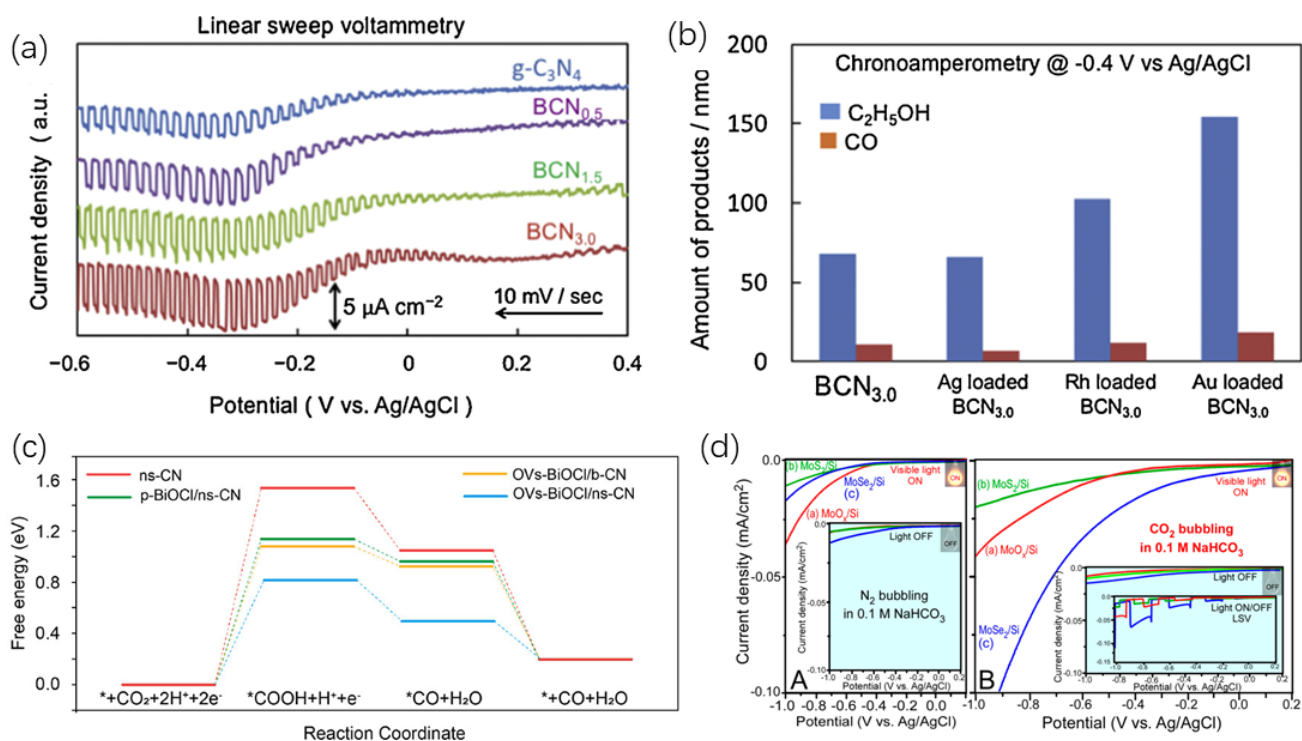


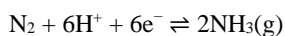
Figure 15. (a) Linear sweep voltammetry of the g-C₃N₄ and B/g-C₃N₄ electrodes. (b) Products analyses of PEC of CO₂RR over cocatalyst loaded B/g-C₃N₄ electrodes.⁹¹ © 2016 Elsevier B.V. (c) Gibbs free energy calculations.⁹⁶ © 2023 American Chemical Society. (d) Linear sweep voltammetry curves (voltage range: +0.2~1.0 V) in N₂- (A) and CO₂-purged (B) 0.1 M NaHCO₃ electrolyte at a scan rate of 10 mV/sec under dark (in the corresponding inset Figure) and the visible light exposure condition for MoO_x/Si, MoS₂/Si and MoSe₂/Si samples. The inset (B) shows the light ON-and-OFF linear sweep voltammetry curves.²¹⁰ © 2019 by the authors. Licensee MDPI, Basel, Switzerland.

5.4 N₂ reduction reaction (NRR)

Ammonia is one of the most important chemicals, and its production, exclusively carried out through the Haber-Bosch

process, accounts for about 1.3% of total CO₂ global emissions.²²⁸ Since the production requires high temperatures (300–500 °C) and pressures (150–300 atm), processes that work under mild conditions are highly desirable.

The overall reaction (below) has an equilibrium potential E° equal to +0.55 V vs NHE.²²⁹



It is well known how the N_2 double bond activation is particularly challenging due to the high cleavage energy (945 kJ mol^{-1}) and the addition of the first H atom to form N_2H^+ has a quite negative potential (-3.2 V vs RHE).²³⁰ Moreover, as well as for NRR, HER is still a competitive process that makes the selectivity toward ammonia even more difficult. PEC of NRR is still a new field since most of the research so far has been more active on the photochemical and electrochemical processes for ammonia production.²³¹

Simple DFT calculations were performed to study the electronic structures of MoS_2 and map out the energy profile of NRR on MoS_2 (Figure 16a and 16b).²³² Ideal scenario for NRR catalysis requires a catalyst with a strong activation (small activation energy, E_a) to N_2 , but a relatively weak binding (small adsorption energy, ΔE) for the intermediate species. The calculations revealed that the basal plane was found to be inert and N_2 molecules even cannot be effectively adsorbed. Moreover, these calculations suggested that the positively charged Mo-edge plays the key role to polarize and activate the N_2 molecules. The computed free-energy profile also demonstrated that the RDS is the reductive protonation of adsorbed N_2 , with a barrier of 0.68 eV without external potential.

As for NRR, 2D HJs can improve the catalytic activity by reducing the charge recombination. Mushtaq et al. reported a $\text{MoSe}_2/\text{g-C}_3\text{N}_4$ HJ used in NRR with 28.9% of faradic efficiency at -0.3 V vs RHE (Figure 16c).⁷⁹ By optimizing the quantity of $\text{g-C}_3\text{N}_4$ (7%) inside the HJ, the photocurrent obtained is higher than the individual semiconductor. In another work by Ye et al., a $\text{MoS}_2/\text{TiO}_2$ HJ optimized with a molar ratio to 1:2 was capable of reaching 65.5 % of faradic efficiency at -0.2 V vs RHE .²³³

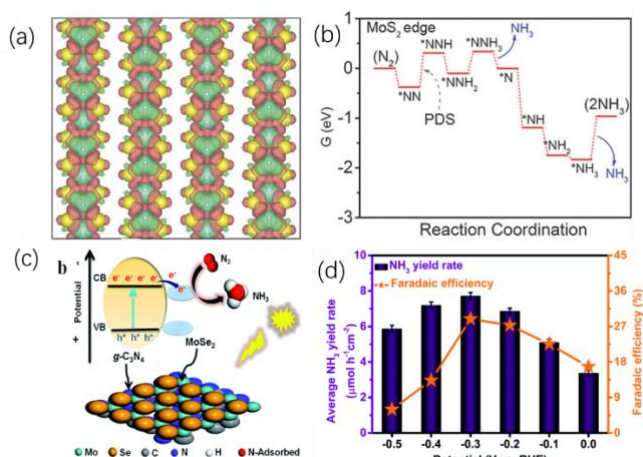


Figure 16. (a) The isosurface of deformation charge density from the top view. Red and green represent charge accumulation and loss, respectively. Isosurface is 0.0025 a.u. (b) Free-energy profile for NRR at MoS_2 edge site. An asterisk (*) denotes as the adsorption site.²³² © 2018 WILEY-VCH Verlag GmbH & Co. KGaA, Weinheim (c) PEC illustration of $\text{MoSe}_2/\text{g-C}_3\text{N}_4$ HJ. (d) Equivalent NH_3 yield rates and FE at the potential from 0 to -0.5 V vs. RHE of $\text{MoSe}_2/\text{g-C}_3\text{N}_4$

heterojunctions. Reproduced with permission from ref ⁷⁹. © 2020 Royal Society of Chemistry.

DFT calculations further predicted that 2D MXene compounds, specifically Nb_3C_2 , can function as efficient NRR catalysts.²³⁴ The mechanism for the electrochemical conversion of N_2 into NH_3 catalysed by d^2 (Ti, Zr, and Hf), d^3 (V, Nb, and Ta), and d^4 (Cr and Mo) 2D transition metal carbides, or MXenes, with formulae M_{n+1}C_n ($n = 2, \text{M}_3\text{C}_2$ unit-cell), has been studied by means of DFT with PBE functional. The calculated results suggested that V_3C_2 and Nb_3C_2 exhibited a strong N_2 fixation ability and had a stronger adsorption energy of N_2 than that of CO and H_2O molecules. Once N_2 was spontaneously captured by V_3C_2 and Nb_3C_2 , limiting barriers of just 0.64 and 0.90 V, respectively, were demanded for its electrochemical conversion into NH_3 .

5.5 Alcohol oxidation

Alcohol oxidation is the anodic reaction in fuel cells which converts chemical energy into electrical energy. Although Pt is currently used as the most effective and stable catalyst for it, the attempt to reduce the amount of Pt by spreading Pt nanoparticles on cheaper and stable substrates with optoelectronic properties is a trend in this field. Till now, there are several 2D catalysts applied as substrates in this direction. Perovskites are a big group of semiconductors used in all the optoelectronic field, and the decoration of Pt on 2D perovskite $\text{La}_2\text{Ti}_2\text{O}_7$ was performed by Hu et al.⁷³ This system is able to make use of the light energy efficiently, with the catalytic methanol oxidation activities 10.6 times higher compared to activities in the dark condition.

$\text{g-C}_3\text{N}_4$ can be used as promising photoactivated support for Pt towards the alcohol oxidation reaction as well.¹⁵ To perform the PEC of methanol oxidation in a 1.0 M $\text{CH}_3\text{OH} + 1.0 \text{ M KOH}$ solution, it is observed that the forward peak current intensity of Pt/ $\text{g-C}_3\text{N}_4$ nanosheets can reach 520.4 mA mg^{-1} , which is higher than that of pure Pt nanoparticles modified electrode (104.8 mA mg^{-1}) (Figure 17a). The introduced ultrathin $\text{g-C}_3\text{N}_4$ as a support will not only prevent the aggregation of Pt during the synthesis process, resulting in small size Pt nanoparticles, but also in favor of adsorption of target molecules owing to 2D structures. On the other hand, when the Pt/ $\text{g-C}_3\text{N}_4$ electrode was upon visible light ($>400 \text{ nm}$) irradiation, the $\text{g-C}_3\text{N}_4$ can be excited and generated electrons in the CB and holes in the VB. Therein, the holes have oxidative ability and can react with surface adsorbed $\text{OH}^-/\text{H}_2\text{O}$ to form strong oxidative hydroxyl radicals ($\bullet\text{OH}$ s). The adsorbed methanol molecules on the surface of catalysts can be also oxidized upon these $\bullet\text{OH}$ s, leading to a photoelectrocatalytic alcohol oxidation process (Figure 17b). Usually, these electron-hole pairs will quickly recombine and only a fraction of holes can be used. On the other hand, the photoexcited electrons transfer to Pt firstly in the Pt/ $\text{g-C}_3\text{N}_4$ composite, and then flow to the circuit under an external electric field, thus preventing the charges recombination. With the combination of $\text{g-C}_3\text{N}_4/\text{CdS}$, the Pt nanoparticles shows 7.4 times enhanced methanol oxidation under visible light irradiation compared to the test in the dark environment.¹⁶ Beside the catalytic activity of methanol oxidation, the stability of corresponding electrode is also significantly improved with assistance of visible light irradiation.

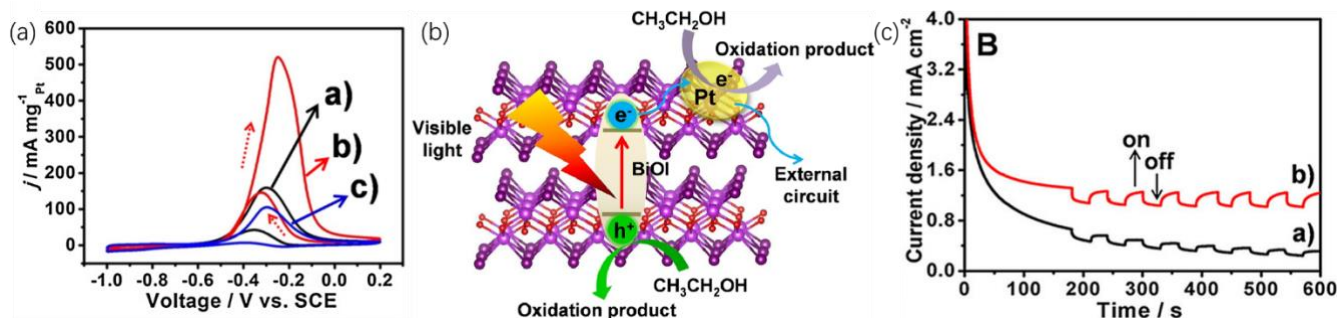


Figure 17. (a) CVs of the Pt/g-C₃N₄ under dark a) and visible light illumination b), and pure Pt nanoparticles c) in 1.0 M CH₃OH + 1.0 M KOH solution at a scan rate of 50 mV s⁻¹. © 2016 Elsevier B.V. (b) Schematic illustration for oxidation ethanol process on Pt/BiOI electrode under visible light illumination. © 2017 Elsevier B.V. (c) Chronoamperometric curves for a) Pt/CdS and b) Pt/CdS/rGO electrodes with and without visible-light illumination every 30 s at -0.3 V. © 2017 Wiley-VCH Verlag GmbH & Co. KGaA, Weinheim.

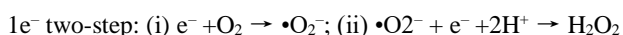
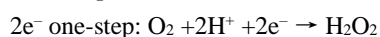
Additionally, there are more than two components in the catalyst system, in which the 2D materials with metallic properties are helpful for charge separation and transfer. For example, Pt/CdS/rGO nanocomposites were reported to have an enhanced catalytic property in methanol oxidation, mainly because the synergetic effect of each composite⁵¹. Specifically, Pt provide the reactive site, CdS oversees light absorption and conversion, rGO mainly favors CT and the stability of the catalyst, as the photoelectric current density remains at around 1.2 mA/cm² at -0.3 V, while the Pt/CdS has a smaller photocurrent and continuously decreasing current density during 600 s of test (Figure 17c).

BiOI has been used as the support for Pt and charge separator, as the pure BiOI does not show any catalytic activity on ethanol oxidation.³⁴ For Pt/BiOI, the CV curves display two typical ethanol electro-oxidation features in the range of -0.8 ~ 0.2 V with forward (ca. -0.20 V) and backward (ca. -0.30 V) peaks in alkaline media. When the Pt/BiOI electrode was upon visible light irradiation, the current density was 874.4 mA mg⁻¹ Pt, which is about 3 times higher than the current in dark. This proved that the photogenerated charges from BiOI can be converted to Pt and used for PEC of ethanol oxidation eventually.

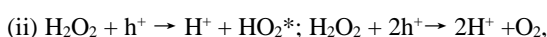
Deep into the mechanism of MOR process, GCP-K DFT calculations were able to find the difference in methylation using chloromethane on 1T MoS₂ and 1T WS₂ surfaces.²³⁵ Thermodynamics and kinetics calculations were performed for the first methyl addition on the experimentally observed coverages. These calculations at constant potential elucidated that (i) the methylation reaction became more favorable as the potential decreased and (ii) the thermodynamics and kinetics of 1T MoS₂ methylation were more favorable than the equivalent reaction on 1T WS₂ at constant potential. The reason behind this was described as differences in the charge per WS₂/MoS₂ unit at constant potential. Methodologically interesting observation was that differences in reactivity decreased, and even reversed, when these reactions were calculated at constant charge instead of constant potential.

5.6 H₂O₂ production

The oxygen reduction reaction is a crucial PEC process that occurs at the cathode. This reaction involves the reduction of O₂ to H₂O or other oxygen-containing species like H₂O₂. The PEC of H₂O₂ production reaction can be described as follows:



Under PEC environment, the active electrons and holes can also lead to H₂O₂ decomposition:



where H⁺/e⁻ is the main cause of H₂O₂ decomposition at lower pH and light-induced holes are the main cause of H₂O₂ decomposition at higher H₂O₂ concentration.⁷⁴ Therefore, the amount of H₂O₂ produced gradually increased with time, and the formation rate gradually slowed down and the yield of H₂O₂ tended to stabilize. MoS₂/CoMoS₄ is a perfect example of this situation. During the PEC H₂O₂ production, the amount of H₂O₂ increases fast from 0 to ~180 μM in the first 60 min under irradiation, while reaches about 205 μM after another 60 min. Therefore, the separation of the product from the reaction cell could be designed to improve the reaction, such as the application of H-cell as the reaction cell.

The puzzling question why many catalysts exhibit high selectivity for H₂O₂ during ORR despite the strong thermodynamic preference for the O-OH breaking leading to the formation of water was studied by first-principles calculations of the electrochemical reaction kinetics at the solid-water interface of single Co-graphene or single vacancy graphene.¹⁸⁶ These authors considered water movement and net electronic charges, using the CP-HS-DM method. The obtained reaction mechanism demonstrated that using these catalysts, breaking the O-OH bond has a higher energy barrier than breaking *-O, due to the rigidity of the O-OH bond. Moreover, the potential and pH affected the selectivity towards formation of H₂O or H₂O₂. For single Co-graphene decreasing potential promoted proton adsorption to the O absorbed onto Co, thus increasing the H₂O₂ selectivity. On the contrary, for single vacancy graphene, the proton preferred to adsorb onto the latter O, resulting in a lower H₂O₂ selectivity in acid condition.

5.7 Metal cations detoxification

Photoelectrocatalysts can be used to detoxify poisonous metal ions by changing their valence state. For example, the oxidation of As(III) to As(V) is performed by the Au/WS₂ photoanode with an efficiency of 95% under visible light illumination⁶³. Removal of uranium from uranium-containing wastewater is of great significance for uranium contamination remediation and development of nuclear energy. To solve this problem, Dai et al designed a photoelectrocatalytic method to reduce the U(VI)

cations to U(IV), which can be deposited on the cathode of the cell. By using the $g\text{-C}_3\text{N}_4/\text{Sn}_3\text{O}_4/\text{Ni}$ photoanode as a S-scheme catalyst to produce and transfer active electrons to the Pt cathode, the deposition rate of U(IV) on the Pt cathode reached 94.28 % at pH of 5.0 for photoelectrocatalytic approach, while the removal rates of U(VI) only amounted to 10.56 % and 36.65 % for the photocatalytic and electrochemical extraction approaches, respectively. The reduction of Cr(VI) to Cr(III) is reported as well.³² By the combination of the active electrons generated from NiFe-LDH/ Co_3O_4 with $\text{Cr}_2\text{O}_7^{2-}$ ions in the waste water, the toxic $\text{Cr}_2\text{O}_7^{2-}$ ions are able to be reduced to Cr^{3+} .

6. Perspective and conclusion

In summary, we have thoroughly reviewed the various 2D layered materials which are used in PEC. This exercise is motivated by the infant research on 2D materials as one of the most promising materials for PEC. Currently, many popular 2D materials (such as graphene and its derivatives, and mostly MXenes) suffer from their metallic property, which means they are not able to behave as an active charge generator. Therefore, they always behave as a co-catalyst in PEC and are mainly responsible for charge separation and transfer. Moreover, semiconductive 2D materials (such as TMDs, $g\text{-C}_3\text{N}_4$, and LDHs) can suffer from their unfavorable band positions, poor charge carrier mobilities and poor stabilities due to the photocorrosion or electrochemical environment. In fact, several strategies have been applied to solve these problems, including HJ, doping, defects engineering and tuning of morphology. From the literature, the efforts in developing the photoelectrocatalysts with these strategies are prominent. In principle, all these strategies aim at tuning the bandgap of the catalytic system to make it suitable for the specific reactions. The formation of HJs, impurity state, defect state and band alignment due to the 2D material size and thickness are proved to work properly in many published works. Meanwhile, some of the strategies described may help to increase the surface-active sites, which synergize the band tuning effort and facilitate the PEC efficiency. Among all these strategies for improvement, we reviewed different kind of structure alignment in the HJs (such as type I, type II, Z-scheme, and S-scheme), in which the 2D materials can behave either as charge generator, charge separator or CT pathways, depending on the natural properties of the 2D materials. In a type I HJs, the component with broader bandgap usually absorbs light and produces active charge carriers, while the component with narrower bandgap can receive the photogenerated charges and provide active sites for the photoelectrocatalytic reactions. Type II is more frequently compared to other types of HJs due to its simplicity and efficiency in charge separation and transport. Z-scheme and S-scheme are less established systems, but show notable architecture developments in CT channels. Thus, in our perspectives, deeper exploration in Z-scheme and S-scheme HJs is to be designed and pursued in the future.

Despite the design of the 2D catalysts, the synthesis methodology is the first step to realize these designs. It is clear that the development of synthesis methods is still at the laboratory level and some steps away from practical applications. The synthesis top-down and bottom-up methods were reviewed in Section 3. In general, the “top-down” methods are more scalable compared to the “bottom-up” ones, as they can leverage existing manufacturing techniques and equipment. Moreover, top-down methods can utilize existing materials, which may already possess desirable properties or

characteristics. Specifically, mechanical force is the main source to destroy the weak interaction between the layers during the synthesis of 2D materials, thanks to the special 2D structure of the materials. Eventually, the synthesized products can keep the original phase with dimension decreased to 2D. In contrast, certain materials may not be suitable for top-down processing due to their inherent properties, making it difficult to achieve desired 2D structures with specific properties. Bottom-up methods allow for precise control at the nanoscale or atomic level, enabling the creation of complex structures with high precision and functionality. Different from top-down methods, bottom-up approaches can produce materials with unique properties not found in bulk materials. By controlling the assembly or synthesis process, it is possible to achieve tailored material properties. Moreover, HJs with complicated design of shapes and compositions are available by bottom-up methods. Furthermore, bottom-up methods are not limited to the phase of the precursors, enabling the creation of new materials with tailored properties and functionalities, opening up possibilities for advancements in various fields. However, there are several disadvantages of bottom-up methods as well. First, scaling up the bottom-up approach from the laboratory to large-scale production can be challenging due to issues related to reproducibility, efficiency, and cost. Second, the assembly or synthesis processes in the bottom-up approach can be complex, requiring precise control of reaction conditions, self-assembly mechanisms, or chemical reactions. The probability of impurities is quite high compared to the top-down methods. As to the industrial synthesis, scalability, reproducibility, cost-effectiveness, and quality control will be always considered. Considering both top-down and bottom-up methods have their strengths and limitations, the representative methods of both of them are developed at the industrial level, resulting in different forms of products. Typically, different kinds of exfoliation have been widely used in producing large quantities of graphene, TMDCs and BP suspensions or powders, while CVD can be used in fabricating large area of films. Although many synthetic strategies have been developed for the synthesis of high quality, large surface area ultrathin 2D materials, the controlled synthesis of the desired layer with high charge carrier mobility of the materials still needs further research attention. Furthermore, practical research is needed for designing efficient hybrid materials with intimate contact and efficient interfacial coupling. By continuously optimizing the parameters of synthesis techniques, large-scale production of different high-quality 2D material HJs for various photoelectrocatalytic reactions will be developed properly. Similarly, even though the theoretical research has reached the maturity to provide great insight into the mechanism of the specific (photo)electrocatalytic reaction using 2D HJs, there is a great space for improvement. The most urgent methodological improvement consists of the simultaneous consideration of both light and applied voltage in the calculation of catalytic processes. This will be realized by considering the catalytic process in the excited state, a holy grail for PEC. Moreover, the current state-of-the-art focuses only on the static description of light interaction with 2D HJs, which can suggest the location of hole and electrons either before or after irradiation. However, the time evolution after the photoexcitation is not usually explicitly calculated and relies only on this static picture and dynamic events are neglected. On the other hand, the description of the EC has progressed significantly as the state-of-the-art calculations are capable of considering constant

potential, as it is applied in the experiments, instead of the most common constant charge approach in the DFT calculations. Here, the challenge is to apply these methodologies, e.g., GCP-K, to large systems, and at the same time reduce its computational cost.

Although 2D materials have achieved very encouraging progress in a wide range of fields from PEC, some challenges remain, which demand an urgent solution. The various challenges and opportunities over 2D material HJs are elaborately discussed in the following section. i) A thorough experimental and theoretical review regarding the activity improvement of 2D material HJs has been presented. In the PEC of water splitting and organic detoxification, there are already plenty of 2D-HJs applied for the reactions. However, some fundamental aspects still need to be addressed to achieve the highest activity result in the target reaction. ii) 2D-HJs have received eye-catching progress in different photoelectrocatalytic reactions such as N₂RR, CO₂RR, ORR, reduction of inorganic pollutants and alcohol oxidation. These are merging as new reactions for PEC; thus, more attention is needed and more kinds of 2D materials should be applied for these reactions in order to find the more suitable catalysts for these reactions. iii) The selection of a photocatalytic system with long-term use and durability is very challenging. Currently, the overall solar energy conversion efficiency differs from 1% to 10%, and the photo energy in the whole PEC occupies around 10%. Hence, a higher photo conversion efficiency must be achieved for the process to be commercialized. 2D semiconductive materials such as g-C₃N₄ and TMDs provide a wide photon absorption range and generates multiple excitons, and thus can be an ideal candidate to obtain photocatalytic HJ for future use. But once the catalysts are used under photoelectrochemical environment, the durability is decreased compared to the ones in photocatalytic system. Thus, designing 2D materials which are resistant to the electrochemical environment is another urgent problem to solve.

All these above perspectives are focused on the 2D materials which have been explored to some extent. Besides, considering that there are still a large number of materials with 2D structures not studied deeply or not applied in the field of PEC, it is promising to expand the type of 2D materials for PEC. To achieve this goal, more synthesis methods should be developed. Besides, novel HJs containing the new 2D materials can be designed as well for better efficiency and stability. Finally, the scope of PEC over 2D-HJs can be further expanded in the aspect of new materials, new methods and new applications. Meanwhile, the mechanisms can be deeply studied to modify the efficiency and durability of the catalysts.

AUTHOR INFORMATION

Corresponding Authors

Mengjiao Wang - *Department of Applied Science and Technology, Politecnico di Torino, 10129 Torino, Italy. E-mail: mengjiao.wang@polito.it*

Teresa Gatti - *Department of Applied Science and Technology, Politecnico di Torino, 10129 Torino, Italy. E-mail: teresa.gatti@polito.it*

Silvio Osella - *Chemical and Biological Systems Simulation Lab, Centre of New Technologies, University of Warsaw, 02097 Warsaw, Poland. E-mail: s.osella@cent.uw.edu.pl*

Authors

Roberto Altieri - *Institute of Physical Chemistry and Center for Materials Research (LaMa), Justus Liebig University, 35392 Giessen, Germany.*

Matteo Crisci - *Institute of Physical Chemistry and Center for Materials Research (LaMa), Justus Liebig University, 35392 Giessen, Germany.*

Michal Langer - *Chemical and Biological Systems Simulation Lab, Centre of New Technologies, University of Warsaw, 02097 Warsaw, Poland.*

Author Contributions

The manuscript was written through contributions of all authors. / All authors have given approval to the final version of the manuscript.

Funding Sources

European Research Council, European Commission, Deutsche Forschungsgemeinschaft, Fondazione Compagnia di San Paolo, National Science Centre, Poland.

Notes

Any additional relevant notes should be placed here.

ACKNOWLEDGMENT

T.G. would acknowledge the support of the European Research Council for the project JANUS BI (grant agreement no. [101041229]). M.W. and T.G. also thank Fondazione Compagnia di San Paolo for financial support through the “Bando TRAPEZIO - Paving the way to research excellence and talent attraction”. R.A. would like to thank the DFG for project 460609161. M.C. and T.G. thank the European Commission for the project LIGHT CAP (grant agreement no. [101017821]). S.O. is grateful to the National Science Centre, Poland (grant no. UMO/2020/39/I/ST4/01446) and the “Excellence Initiative – Research University” (IDUB) Program, Action I.3.3 – “Establishment of the Institute for Advanced Studies (IAS)” for funding (grant no. UW/IDUB/2020/25).

ABBREVIATIONS

2D, two-dimensional; PEC, (photo)electrocatalysis; CT, charge transfer; CB, conduction band; HRTEM, High resolution transmission electron microscopy; g-C₃N₄, graphitic carbon nitride; MCs, metal chalcogenides; HJ, heterojunction; vdWs, van der Waals; MPCh₃, metal phosphorous trichalcogenides; h-BN, hexagonal boron nitride; MOFs, metal organic frameworks; LDHs, layered double hydroxides; rGO, reduced graphene oxide; GO, graphene oxide; TMDCs, transition metal dichalcogenides; ITO, indium tin oxide; VB, valence band; IEF, internal electric field; SmV, samarium vanadate; CO₂RR, CO₂ reduction reaction; MOR, Methanol oxidation reaction; RhB, rhodamine B; CQDs, carbon quantum dots; OER, oxygen evolution reaction; HER, hydrogen evolution reaction; CVD, chemical vapor deposition; Ni-Bi, nanosized pure nickel boron oxide; CN, carbon nitride; QM, quantum mechanics; MM, molecular mechanics; MKM, microkinetic-modeling; DFT, density functional theory; MD, molecular dynamics; AIMD, *ab-initio* MD; CMD, constrained molecular dynamics; DFT-CES, density functional theory in

classical explicit solvent; QEq, charge equilibration; LDA, local density approximation; GGA, generalized gradient approximation; HSE, Heyd–Scuseria–Ernzerhof; MBPT, many-body perturbation theory; NAMD, nonadiabatic MD; TDDFT, time dependent density functional theory; GS, ground state; ES, excited state; BSE, Bethe–Salpeter equation; CHE, computational hydrogen electrode; PCET, proton-coupled electron transfer; SHE, standard hydrogen electrode; RHE, reversible hydrogen electrode; CP-HS-DM, constant potential-hybrid solvation-dynamic model; GCP-K, grand canonical potential kinetics; kMC, kinetic Monte Carlo; BEP, Brønsted–Evans–Polanyi; IPCE, incident photocurrent efficiency; SiNW, silicon nanowire; RuSA, ruthenium single atom; BP, black phosphorus; NGr, nitrogen-doped graphene; RDS, rate determining step; ROS, reactive oxygen species; BPA, Bisphenol A; TC, Tetracycline; LOM, Lomefloxacin; PNP, p-nitrophenol; MB, Methylene blue; PAP, p-aminophenol; NRR, N₂ reduction reaction;

REFERENCES

- Wu, H.; Huang, Q.; Shi, Y.; Chang, J.; Lu, S. Electrocatalytic Water Splitting: Mechanism and Electrocatalyst Design. *Nano Res.* **2023**, *1*–16. <https://doi.org/10.1007/S12274-023-5502-8>.
- Chanda, D.; Xing, R.; Xu, T.; Liu, Q.; Luo, Y.; Liu, S.; Tufa, R. A.; Dolla, T. H.; Montini, T.; Sun, X. Electrochemical Nitrogen Reduction: Recent Progress and Prospects. *Chem. Commun.* **2021**, *57* (60), 7335–7349. <https://doi.org/10.1039/D1CC01451J>.
- Long, C.; Li, X.; Guo, J.; Shi, Y.; Liu, S.; Tang, Z. Electrochemical Reduction of CO₂ over Heterogeneous Catalysts in Aqueous Solution: Recent Progress and Perspectives. *Small Methods* **2019**, *3* (3), 1800369. <https://doi.org/10.1002/SMTD.201800369>.
- Li, X.; Lu, S.; Zhang, G. Three-Dimensional Structured Electrode for Electrocatalytic Organic Wastewater Purification: Design, Mechanism and Role. *J. Hazard. Mater.* **2023**, *445*, 130524. <https://doi.org/10.1016/J.JHAZMAT.2022.130524>.
- Ahmed, S. F.; Mofijur, M.; Nuzhat, S.; Rafa, N.; Musharrat, A.; Lam, S. S.; Boretti, A. Sustainable Hydrogen Production: Technological Advancements and Economic Analysis. *Int. J. Hydrogen Energy* **2022**, *47* (88), 37227–37255. <https://doi.org/10.1016/J.IJHYDENE.2021.12.029>.
- Fujishima, A.; Honda, K. Electrochemical Photolysis of Water at a Semiconductor Electrode. *Nat.* **1972**, *238* (5358), 37–38. <https://doi.org/10.1038/238037a0>.
- Wu, B.; Kempt, R.; Kovalska, E.; Luxa, J.; Kuc, A.; Heine, T.; Sofer, Z. Lithium-Assisted Exfoliation of Palladium Thiophosphate Nanosheets for Photoelectrocatalytic Water Splitting. *ACS Appl. Nano Mater.* **2021**, *4* (1), 441–448. https://doi.org/10.1021/ACSANM.0C02775/ASSET/IMAGES/LARGE/AN0C02775_0004.JPEG.
- Muthuraman, G.; Choi, Y.; Daekeun, K.; Hu, J.; Zhang, C.; Liu, A. C. L.; Zhang, N.; Li, J. Review—Strategic Design of Layered Double Hydroxides and Graphitic Carbon Nitride Heterostructures for Photoelectrocatalytic Water Splitting Applications. *J. Electrochem. Soc.* **2022**, *169* (4), 046515. <https://doi.org/10.1149/1945-7111/AC65B8>.
- Fareza, A. R.; Nugroho, F. A. A.; Abdi, F. F.; Fauzia, V. Nanoscale Metal Oxides–2D Materials Heterostructures for Photoelectrochemical Water Splitting—a Review. *J. Mater. Chem. A* **2022**, *10* (16), 8656–8686. <https://doi.org/10.1039/D1TA10203F>.
- Faraji, M.; Yousefi, M.; Yousefzadeh, S.; Zirak, M.; Naseri, N.; Jeon, T. H.; Choi, W.; Moshfegh, A. Z. Two-Dimensional Materials in Semiconductor Photoelectrocatalytic Systems for Water Splitting. *Energy Environ. Sci.* **2019**, *12* (1), 59–95. <https://doi.org/10.1039/C8EE00886H>.
- Luo, M.; Li, H.; Wang, Z.; Shen, Q.; Xue, J.; Liu, X.; Jia, H. In-Situ Growth of MOF Nanosheets with Controllable Thickness on Copper Foam for Photoelectrocatalytic CO₂ Reduction. *J. Mater. Sci. Mater. Electron.* **2022**, *33* (18), 14568–14580. <https://doi.org/10.1007/S10854-022-08378-4/FIGURES/8>.
- Sanna, M.; Ng, S.; Pumeru, M. Layered Transition Metal Selenophosphites for Visible Light Photoelectrochemical Production of Hydrogen. *Electrochem. Commun.* **2021**, *129*, 107077. <https://doi.org/10.1016/J.ELECOM.2021.107077>.
- Zhao, F.; Li, W.; Song, Y.; Fu, Y.; Liu, X.; Ma, C.; Wang, G.; Dong, X.; Ma, H. Constructing S-Scheme Co₃O₄-C₃N₄ Catalyst with Superior Photoelectrocatalytic Efficiency for Water Purification. *Appl. Mater. Today* **2022**, *26*, 101390. <https://doi.org/10.1016/J.APMT.2022.101390>.
- Zhao, D.; Dai, F. C.; Li, A. C.; Chen, Y.; Li, G. H.; Wang, Q.; Hou, W. S.; Zhou, H. Z. Photoelectrocatalytic Properties and Mechanism of Rhodamine B Degradation Using a Graphene Oxide/Ag₃PO₄/Ni Film Electrode. *New J. Chem.* **2020**, *44* (22), 9502–9508. <https://doi.org/10.1039/D0NJ00864H>.
- Zhu, M.; Zhai, C.; Sun, M.; Hu, Y.; Yan, B.; Du, Y. Ultrathin Graphitic C₃N₄ Nanosheet as a Promising Visible-Light-Activated Support for Boosting Photoelectrocatalytic Methanol Oxidation. *Appl. Catal. B Environ.* **2017**, *203*, 108–115. <https://doi.org/10.1016/J.APCATB.2016.10.012>.
- Hu, J.; Yu, C.; Zhai, C.; Hu, S.; Wang, Y.; Fu, N.; Zeng, L.; Zhu, M. 2D/1D Heterostructure of g-C₃N₄ Nanosheets/CdS Nanowires as Effective Photo-Activated Support for Photoelectrocatalytic Oxidation of Methanol. *Catal. Today* **2018**, *315*, 36–45. <https://doi.org/10.1016/J.CATTOD.2018.02.043>.
- Hu, X.; Yang, H.; Gao, M.; Tian, H.; Li, Y.; Liang, Z.; Jian, X. Insights into the Photoassisted Electrocatalytic Reduction of CO₂ over a Two-Dimensional MoS₂ Nanostructure Loaded on SnO₂ Nanoparticles. *ChemElectroChem* **2019**, *6* (12), 3077–3084. <https://doi.org/10.1002/CELC.201900632>.
- Qi, Y.; Xu, Q.; Wang, Y.; Yan, B.; Ren, Y.; Chen, Z. CO₂-Induced Phase Engineering: Protocol for Enhanced Photoelectrocatalytic Performance of 2D MoS₂ Nanosheets. *ACS Nano* **2016**, *10* (2), 2903–2909. https://doi.org/10.1021/ACS.NANO.6B00001/ASSET/IMAGES/LARGE/NN-2016-000016_0004.JPEG.
- Zhu, Y.; Zhao, X.; Li, J.; Zhang, H.; Chen, S.; Han, W.; Yang, D. Surface Modification of Hematite Photoanode by NiFe Layered Double Hydroxide for Boosting Photoelectrocatalytic Water Oxidation. *J. Alloys Compd.* **2018**, *764*, 341–346. <https://doi.org/10.1016/J.JALLCOM.2018.06.064>.
- Avouris, P.; Dimitrakopoulos, C. Graphene: Synthesis and Applications. *Mater. Today* **2012**, *15* (3), 86–97. [https://doi.org/10.1016/S1369-7021\(12\)70044-5](https://doi.org/10.1016/S1369-7021(12)70044-5).
- Li, M.; Lu, Q.; Liu, M.; Yin, P.; Wu, C.; Li, H.; Zhang, Y.; Yao, S. Photoinduced Charge Separation via the Double-Electron Transfer Mechanism in Nitrogen Vacancies g-C₃N₅/BiOBr for the Photoelectrochemical Nitrogen Reduction. *ACS Appl. Mater. Interfaces* **2020**, *12* (34), 38266–38274. https://doi.org/10.1021/ACSAMI.0C11894/ASSET/IMAGES/LARGE/AM0C11894_0006.JPEG.
- Xu, H.; Zhu, J.; Ma, Q.; Ma, J.; Bai, H.; Chen, L.; Mu, S. Two-Dimensional MoS₂: Structural Properties, Synthesis Methods, and Regulation Strategies toward Oxygen Reduction. *Micromachines* **2021**, *Vol. 12*, Page 240 **2021**, *12* (3), 240. <https://doi.org/10.3390/M12030240>.
- Cong, C.; Shang, J.; Wang, Y.; Yu, T. Optical Properties of 2D Semiconductor WS₂. *Adv. Opt. Mater.* **2018**, *6* (1), 1700767. <https://doi.org/10.1002/ADOM.201700767>.
- Hanson, E. D.; Lilley, L. M.; Cain, J. D.; Hao, S.; Palacios, E.; Aydin, K.; Wolverson, C.; Meade, T.; Druvid, V. P. Phase Engineering and Optical Properties of 2D MoSe₂: Promise and Pitfalls. *Mater. Chem. Phys.* **2019**, *225*, 219–226. <https://doi.org/10.1016/J.MATCHEMPHYS.2018.11.069>.
- Sheraz, A.; Mehmood, N.; Çiçek, M. M.; Ergün, I.; Ergün, E.; Rasouli, H. R.; Durgun, E.; Kasirga, T. S. High Elasticity and Strength of Ultra-Thin Metallic Transition Metal Dichalcogenides. *Nanoscale Adv.* **2021**, *3* (13), 3894–3899. <https://doi.org/10.1039/D1NA00225B>.
- Arif, M.; Yasin, G.; Shakeel, M.; Fang, X.; Gao, R.; Ji, S.; Yan, D. Coupling of Bifunctional CoMn-Layered Double Hydroxide@Graphitic C₃N₄ Nanohybrids towards Efficient Photoelectrochemical Overall Water Splitting. *Chem. – An Asian J.* **2018**, *13* (8), 1045–1052. <https://doi.org/10.1002/ASIA.201800016>.
- Shakeel, M.; Arif, M.; Yasin, G.; Li, B.; Khan, H. D. Layered by Layered Ni-Mn-LDH/g-C₃N₄ Nanohybrid for Multi-Purpose

- Photo/Electrocatalysis: Morphology Controlled Strategy for Effective Charge Carriers Separation. *Appl. Catal. B Environ.* **2019**, *242*, 485–498. <https://doi.org/10.1016/J.APCATB.2018.10.005>.
- (28) Liu, X.; Liang, J.; Song, X.; Yang, H.; Li, X.; Dai, H.; Song, Y.; Liu, Y.; Hu, J.; Pan, X.; OuYang, X.; Liang, Z. Enhanced Water Dissociation Performance of Graphitic-C3N4 Assembled with ZnCr-Layered Double Hydroxide. *Chem. Eng. J.* **2018**, *337*, 560–566. <https://doi.org/10.1016/J.CEJ.2017.12.138>.
- (29) Pirkarami, A.; Rasouli, S.; Ghasemi, E. 3-D CdS@NiCo Layered Double Hydroxide Core-Shell Photoelectrocatalyst Used for Efficient Overall Water Splitting. *Appl. Catal. B Environ.* **2019**, *241*, 28–40. <https://doi.org/10.1016/J.APCATB.2018.09.021>.
- (30) Wei, P.; Wen, Y.; Lin, K.; Li, X. Turning off the “Shunt Channel” by Coating with CoFe Layered Double Hydroxide Nanocrystals for Efficient Photoelectrocatalytic Water Splitting. *Inorg. Chem. Front.* **2022**, *9* (18), 4685–4694. <https://doi.org/10.1039/D2QI00760F>.
- (31) Ye, W.; He, C.; Asim Mushtaq, M.; Lin, K.; Xing, X. High Performance Cobalt-Vanadium Layered Double Hydroxide Nanosheets for Photoelectrochemical Reduction of Nitrogen. *Eur. J. Inorg. Chem.* **2022**, *2022* (26), e202200325. <https://doi.org/10.1002/EJIC.202200325>.
- (32) Fei, W.; Gao, J.; Li, N.; Chen, D.; Xu, Q.; Li, H.; He, J.; Lu, J. A Visible-Light Active p-n Heterojunction NiFe-LDH/Co3O4 Supported on Ni Foam as Photoanode for Photoelectrocatalytic Removal of Contaminants. *J. Hazard. Mater.* **2021**, *402*, 123515. <https://doi.org/10.1016/J.JHAZMAT.2020.123515>.
- (33) Raza, A.; Zhang, X.; Ali, S.; Cao, C.; Rafi, A. A.; Li, G. Photoelectrochemical Energy Conversion over 2D Materials. *Photochem 2022, Vol. 2, Pages 272-298* **2022**, *2* (2), 272–298. <https://doi.org/10.3390/PHOTOCHEM2020020>.
- (34) Zhai, C.; Hu, J.; Sun, M.; Zhu, M. Two Dimensional Visible-Light-Active Pt-BiOI Photoelectrocatalyst for Efficient Ethanol Oxidation Reaction in Alkaline Media. *Appl. Surf. Sci.* **2018**, *430*, 578–584. <https://doi.org/10.1016/J.APSUSC.2017.06.175>.
- (35) Xu, Y.; Wang, F.; Zhao, D.; Gao, Y.; Lei, S.; Chang, S.; Li, S.; Ma, X.; Wang, M.; Jing, H. Two-Dimensional TiO2/Mxene Ti3cn Heterojunction for Highly Efficient Photoelectrocatalytic Co2 Reduction. *SSRN Electron. J.* **2022**. <https://doi.org/10.2139/SSRN.4076641>.
- (36) Xu, X.; Hu, J.; Yin, Z.; Xu, C. Photoanode Current of Large-Area MoS2 Ultrathin Nanosheets with Vertically Mesh-Shaped Structure on Indium Tin Oxide. *ACS Appl. Mater. Interfaces* **2014**, *6* (8), 5983–5987. https://doi.org/10.1021/AM501159S/SUPPL_FILE/AM501159S_SI_001.PDF.
- (37) Mengjiao Wang; Silvio Osella; Rosaria Brescia; Zheming Liu; Jaime Gallego; Mattia Cattelan; Matteo Crisci; Stefano Agnoli; Teresa Gatti. 2D MoS₂/BiOBr van Der Waals Heterojunctions by Liquid-Phase Exfoliation as Photoelectrocatalysts for Hydrogen Evolution. *Nanoscale* **2023**, *15* (2), 522–531. <https://doi.org/10.1039/D2NR04970H>.
- (38) Mary Rajaiitha, P.; Shamsa, K.; Murugan, C.; Bhojanaa, K. B.; Ravichandran, S.; Jothivenkatachalam, K.; Pandikumar, A. Graphitic Carbon Nitride Nanoplatelets Incorporated Titania Based Type-II Heterostructure and Its Enhanced Performance in Photoelectrocatalytic Water Splitting. *SN Appl. Sci.* **2020**, *2* (4), 1–14. <https://doi.org/10.1007/S42452-020-2190-9/FIGURES/10>.
- (39) Murugan, C.; Bhojanaa, K. B.; Ong, W. J.; Jothivenkatachalam, K.; Pandikumar, A. Improving Hole Mobility with the Heterojunction of Graphitic Carbon Nitride and Titanium Dioxide via Soft Template Process in Photoelectrocatalytic Water Splitting. *Int. J. Hydrogen Energy* **2019**, *44* (59), 30885–30898. <https://doi.org/10.1016/J.IJHYDENE.2019.09.114>.
- (40) Tang, H.; Shang, Q.; Tang, Y.; Yi, X.; Wei, Y.; Yin, K.; Liu, M.; Liu, C. Static and Continuous Flow Photoelectrocatalytic Treatment of Antibiotic Wastewater over Mesh of TiO2 Nanotubes Implanted with G-C3N4 Nanosheets. *J. Hazard. Mater.* **2020**, *384*, 121248. <https://doi.org/10.1016/J.JHAZMAT.2019.121248>.
- (41) Wang, W. K.; Zhu, W.; Mao, L.; Zhang, J.; Zhou, Z.; Zhao, G. Two-Dimensional TiO₂-g-C3N4 with Both TiN and CO Bridges with Excellent Conductivity for Synergistic Photoelectrocatalytic Degradation of Bisphenol A. *J. Colloid Interface Sci.* **2019**, *557*, 227–235. <https://doi.org/10.1016/J.JCIS.2019.08.088>.
- (42) Alam, K. M.; Kumar, P.; Kar, P.; Thakur, U. K.; Zeng, S.; Cui, K.; Shankar, K. Enhanced Charge Separation in G-C3N4-BiOI Heterostructures for Visible Light Driven Photoelectrochemical Water Splitting. *Nanoscale Adv.* **2019**, *1* (4), 1460–1471. <https://doi.org/10.1039/C8NA00264A>.
- (43) Alkorbi, A. S.; Kumar, K. Y.; Prashanth, M. K.; Parashuram, L.; Abate, A.; Alharti, F. A.; Jeon, B. H.; Raghu, M. S. Samarium Vanadate Affixed Sulfur Self Doped G-C3N4 Heterojunction; Photocatalytic, Photoelectrocatalytic Hydrogen Evolution and Dye Degradation. *Int. J. Hydrogen Energy* **2022**, *47* (26), 12988–13003. <https://doi.org/10.1016/J.IJHYDENE.2022.02.071>.
- (44) Masoumi, Z.; Tayebi, M.; Lee, B. K. Ultrasonication-Assisted Liquid-Phase Exfoliation Enhances Photoelectrochemical Performance in α -Fe2O3/MoS2 Photoanode. *Ultrason. Sonochem.* **2021**, *72*, 105403. <https://doi.org/10.1016/J.ULTSONCH.2020.105403>.
- (45) Liu, S.; Zhao, M.; He, Z.; Zhong, Y.; Ding, H.; Chen, D. Preparation of a P-n Heterojunction 2D BiOI Nanosheet/1DBiPO4 Nanorod Composite Electrode for Enhanced Visible Light Photoelectrocatalysis. *Chinese J. Catal.* **2019**, *40* (3), 446–457. [https://doi.org/10.1016/S1872-2067\(18\)63186-9](https://doi.org/10.1016/S1872-2067(18)63186-9).
- (46) Tayebi, M.; Masoumi, Z.; Lee, B. K. Ultrasonically Prepared Photocatalyst of W/WO3 Nanoplates with WS2 Nanosheets as 2D Material for Improving Photoelectrochemical Water Splitting. *Ultrason. Sonochem.* **2021**, *70*, 105339. <https://doi.org/10.1016/J.ULTSONCH.2020.105339>.
- (47) Samsudin, M. F. R.; Sufian, S. Hybrid 2D/3D g-C3N4/BiVO4 Photocatalyst Decorated with RGO for Boosted Photoelectrocatalytic Hydrogen Production from Natural Lake Water and Photocatalytic Degradation of Antibiotics. *J. Mol. Liq.* **2020**, *314*, 113530. <https://doi.org/10.1016/J.MOLLIQ.2020.113530>.
- (48) Kadeer, K.; Reheman, A.; Maimaitizi, H.; Talifu, D.; Tursun, Y.; Abulizi, A. Preparation of RGO/AgCl QDs and Its Enhanced Photoelectrocatalytic Performance for the Degradation of Tetracycline. *J. Am. Ceram. Soc.* **2019**, *102* (9), 5342–5352. <https://doi.org/10.1111/JACE.16391>.
- (49) Zhou, Q.; Xing, A.; Li, J.; Zhao, D.; Zhao, K.; Lei, M. Synergistic Enhancement in Photoelectrocatalytic Degradation of Bisphenol A by CeO2 and Reduced Graphene Oxide Co-Modified TiO2 Nanotube Arrays in Combination with Fenton Oxidation. *Electrochim. Acta* **2016**, *209*, 379–388. <https://doi.org/10.1016/J.ELECTACTA.2016.05.094>.
- (50) Zhang, M.; Xuan, X.; Wang, W.; Ma, C.; Lin, Z.; Zhang, M.; Wang, W.; Ma, C.; Lin, Z.; Xuan, X. Anode Photovoltage Compensation-Enabled Synergistic CO2 Photoelectrocatalytic Reduction on a Flower-Like Graphene-Decorated Cu Foam Cathode. *Adv. Funct. Mater.* **2020**, *30* (52), 2005983. <https://doi.org/10.1002/ADFM.202005983>.
- (51) Zhai, C.; Hu, J.; Sun, M.; Zhu, M. High-Performance Visible-Light-Driven Pt/CdS/Graphene Photoelectrocatalysts for Methanol Oxidation. *Energy Technol.* **2017**, *5* (8), 1292–1299. <https://doi.org/10.1002/ENTE.201600637>.
- (52) Braiek, Z.; Ben Naceur, J.; Jrad, F.; Ben Assaker, I.; Chtourou, R. Novel Synthesis of Graphene Oxide/In2S3/TiO2 NRs Heterojunction Photoanode for Enhanced Photoelectrochemical (PEC) Performance. *Int. J. Hydrogen Energy* **2022**, *47* (6), 3655–3666. <https://doi.org/10.1016/J.IJHYDENE.2021.10.268>.
- (53) Velusamy, P.; Sathiy, M.; Liu, Y.; Liu, S.; Ramesh Babu, R.; Aly Saad Aly, M.; Elangovan, E.; Chang, H.; Mao, L.; Xing, R. Investigating the Effect of Nd3+ Dopant and the Formation of G-C3N4/BiOI Heterostructure on the Microstructural, Optical and Photoelectrocatalytic Properties of g-C3N4. *Appl. Surf. Sci.* **2021**, *561*, 150082. <https://doi.org/10.1016/J.APSUSC.2021.150082>.
- (54) Amedlous, A.; Majdoub, M.; Amaterz, E.; Anfar, Z.; Benlhachemi, A. Synergistic Effect of G-C3N4 Nanosheets/Ag3PO4 Microcubes as Efficient n-p-Type Heterostructure Based Photoanode for Photoelectrocatalytic Dye Degradation. *J. Photochem. Photobiol. A Chem.* **2021**, *409*, 113127. <https://doi.org/10.1016/J.JPHOTOCHEM.2020.113127>.
- (55) Du, Y.; Ma, R.; Wang, L.; Qian, J.; Wang, Q. 2D/1D BiOI/g-C3N4 Nanotubes Heterostructure for Photoelectrochemical Overall Water Splitting. *Sci. Total Environ.* **2022**, *838*, 156166.

- <https://doi.org/10.1016/J.SCITOTENV.2022.156166>.
- (56) Samsudin, M. F. R.; Ullah, H.; Tahir, A. A.; Li, X.; Ng, Y. H.; Sufian, S. Superior Photoelectrocatalytic Performance of Ternary Structural BiVO₄/GQD/g-C₃N₄ Heterojunction. *J. Colloid Interface Sci.* **2021**, *586*, 785–796. <https://doi.org/10.1016/J.JCIS.2020.11.003>.
- (57) Jing, L.; Zhu, R.; Phillips, D. L.; Yu, J. C.; Jing, L.; Yu, C.; Zhu, R. X.; Phillips, D. L. Effective Prevention of Charge Trapping in Graphitic Carbon Nitride with Nanosized Red Phosphorus Modification for Superior Photo(Electro)Catalysis. *Adv. Funct. Mater.* **2017**, *27* (46), 1703484. <https://doi.org/10.1002/ADFM.201703484>.
- (58) Zhang, Z.; Lin, S.; Li, X.; Li, H.; Cui, W. Metal Free and Efficient Photoelectrocatalytic Removal of Organic Contaminants over G-C 3 N 4 Nanosheet Films Decorated with Carbon Quantum Dots. *RSC Adv.* **2017**, *7* (89), 56335–56343. <https://doi.org/10.1039/C7RA11205J>.
- (59) Peng, G.; Qin, J.; Volokh, M.; Shalom, M. Freestanding Hierarchical Carbon Nitride/Carbon-Paper Electrode as a Photoelectrocatalyst for Water Splitting and Dye Degradation. *ACS Appl. Mater. Interfaces* **2019**, *11* (32), 29139–29146. https://doi.org/10.1021/ACSAMI.9B08263/ASSET/IMAGES/LARGE/AM9B08263_0004.JPEG.
- (60) Dai, Z.; Lian, J.; Sun, Y.; Li, L.; Zhang, H.; Hu, N.; Ding, D. Fabrication of G-C₃N₄/Sn₃O₄/Ni Electrode for Highly Efficient Photoelectrocatalytic Reduction of U(VI). *Chem. Eng. J.* **2022**, *433*, 133766. <https://doi.org/10.1016/J.CEJ.2021.133766>.
- (61) Wang, F.; Ou, R.; Yu, H.; Lu, Y.; Qu, J.; Zhu, S.; Zhang, L.; Huo, M. Photoelectrocatalytic PNP Removal Using C₃N₄ Nanosheets/ α -Fe₂O₃ Nanoarrays Photoanode: Performance, Mechanism and Degradation Pathways. *Appl. Surf. Sci.* **2021**, *565*, 150597. <https://doi.org/10.1016/J.APSUSC.2021.150597>.
- (62) Singla, S.; Basu, S.; Devi, P. Solar Light Responsive 2D/2D BiVO₄/SnS₂ Nanocomposite for Photocatalytic Elimination of Recalcitrant Antibiotics and Photoelectrocatalytic Water Splitting with High Performance. *J. Ind. Eng. Chem.* **2023**, *118*, 119–131. <https://doi.org/10.1016/J.JIEC.2022.10.051>.
- (63) Bharath, G.; Rambabu, K.; Alqassem, B.; Morajkar, P. P.; Abu Haija, M.; Nadda, A. K.; Gupta, V. K.; Banat, F. Fabrication of Gold Nanodots Decorated on 2D Tungsten Sulfide (Au-WS₂) Photoanode for Simultaneous Oxidation of Phenol and Arsenic (III) from Industrial Wastewater. *Chem. Eng. J.* **2023**, *456*, 141062. <https://doi.org/10.1016/J.CEJ.2022.141062>.
- (64) Li, Q.; Ma, X.; Liu, H.; Chen, Z.; Chen, H.; Chu, S. Self-Organized Growth of Two-Dimensional GaTe Nanosheet on ZnO Nanowires for Heterojunctional Water Splitting Applications. *ACS Appl. Mater. Interfaces* **2017**, *9* (22), 18836–18844. https://doi.org/10.1021/ACSAMI.7B04199/ASSET/IMAGES/LARGE/AM-2017-04199J_0008.JPEG.
- (65) Tang, C. bin; Huang, P.; Liu, Z.; Lei, D.; Xue, J. Improved Photoelectrocatalytic Degradation of Methylene Blue by Ti₃C₂T_x/Bi₁₂TiO₂₀ Composite Anodes. *Ceram. Int.* **2022**, *48* (17), 24943–24952. <https://doi.org/10.1016/J.CERAMINT.2022.05.148>.
- (66) Tang, R.; Zhou, S.; Li, C.; Chen, R.; Zhang, L.; Zhang, Z.; Yin, L. Janus-Structured Co-Ti₃C₂ MXene Quantum Dots as a Schottky Catalyst for High-Performance Photoelectrochemical Water Oxidation. *Adv. Funct. Mater.* **2020**, *30* (19), 2000637. <https://doi.org/10.1002/ADFM.202000637>.
- (67) Xu, Y.; Wang, F.; Lei, S.; Wei, Y.; Zhao, D.; Gao, Y.; Ma, X.; Li, S.; Chang, S.; Wang, M.; Jing, H. In Situ Grown Two-Dimensional TiO₂/Ti₃CN MXene Heterojunction Rich in Ti₃⁺ Species for Highly Efficient Photoelectrocatalytic CO₂ Reduction. *Chem. Eng. J.* **2023**, *452*, 139392. <https://doi.org/10.1016/J.CEJ.2022.139392>.
- (68) Xu, Y.; Wang, S.; Yang, J.; Han, B.; Nie, R.; Wang, J.; Wang, J.; Jing, H. In-Situ Grown Nanocrystal TiO₂ on 2D Ti₃C₂ Nanosheets for Artificial Photosynthesis of Chemical Fuels. *Nano Energy* **2018**, *51*, 442–450. <https://doi.org/10.1016/J.NANOEN.2018.06.086>.
- (69) Jia, L.; Tan, X.; Yu, T.; Zhang, Z. Enhanced Photoelectrocatalytic Performance of Temperature-Dependent 2D/1D BiOBr/TiO₂-x Nanotubes. *Mater. Res. Bull.* **2018**, *105*, 322–329. <https://doi.org/10.1016/J.MATERRESBULL.2018.05.005>.
- (70) Wei, P.; Wen, Y.; Lin, K.; Li, X. 2D/3D WO₃/BiVO₄ Heterostructures for Efficient Photoelectrocatalytic Water Splitting. *Int. J. Hydrogen Energy* **2021**, *46* (54), 27506–27515. <https://doi.org/10.1016/J.IJHYDENE.2021.06.007>.
- (71) Gao, H.; Zhai, C.; Fu, N.; Du, Y.; Yu, K.; Zhu, M. Synthesis of Pt Nanoparticles Supported on a Novel 2D Bismuth Tungstate/Lanthanum Titanate Heterojunction for Photoelectrocatalytic Oxidation of Methanol. *J. Colloid Interface Sci.* **2020**, *561*, 338–347. <https://doi.org/10.1016/J.JCIS.2019.10.114>.
- (72) Wang, H.; Qi, F.; Chen, X.; Guo, H.; Cui, W. Enhanced Photoelectrocatalytic Degradation by TiO₂ Nano-Arrays Decorated with Two-Dimensional Ultra-Thin P3HT Nanosheets. *Mater. Lett.* **2021**, *302*, 130432. <https://doi.org/10.1016/J.MATLET.2021.130432>.
- (73) Hu, J.; Sun, M.; Cai, X.; Zhai, C.; Zhang, J.; Zhu, M. Two Dimensional Perovskite La₂Ti₂O₇ Nanosheet as Pt Catalyst Support for Photo-Assisted Methanol Oxidation Reaction. *J. Taiwan Inst. Chem. Eng.* **2017**, *80*, 231–238. <https://doi.org/10.1016/J.JTICE.2017.07.001>.
- (74) Zhang, A.; Yang, L.; Zhang, L. Z-Scheme 2D/3D Hierarchical MoS₂@CoMoS₄ Flower-Shaped Arrays with Enhanced Full Spectrum Light Photoelectrocatalytic Activity for H₂O₂/p-Aminophenol Production and Contaminant Degradation. *J. Mater. Chem. A* **2020**, *8* (48), 25890–25903. <https://doi.org/10.1039/D0TA07796H>.
- (75) Si, K.; Ma, J.; Lu, C.; Zhou, Y.; He, C.; Yang, D.; Wang, X.; Xu, X. A Two-Dimensional MoS₂/WSe₂ van Der Waals Heterostructure for Enhanced Photoelectric Performance. *Appl. Surf. Sci.* **2020**, *507*. <https://doi.org/10.1016/J.APSUSC.2019.145082>.
- (76) Mu, J.; Miao, H.; Liu, E.; Chen, L.; Feng, J.; Han, T.; Gao, Y.; Fan, J.; Hu, X. Using Al₂O₃ Defect Levels to Enhance the Photoelectrocatalytic Activity of SnS₂ Nanosheets. *Ceram. Int.* **2017**, *43* (6), 4992–5001. <https://doi.org/10.1016/J.CERAMINT.2017.01.006>.
- (77) Sherrell, P. C.; Palczynski, P.; Sokolikova, M. S.; Reale, F.; Pesci, F. M.; Och, M.; Mattevi, C. Large-Area CVD MoS₂/WS₂ Heterojunctions as a Photoelectrocatalyst for Salt-Water Oxidation. *ACS Appl. Energy Mater.* **2019**, *2* (8), 5877–5882. https://doi.org/10.1021/ACSAEM.9B01008/ASSET/IMAGES/LARGE/AE-2019-010089_0003.JPEG.
- (78) Hou, Y.; Wen, Z.; Cui, S.; Guo, X.; Chen, J.; Hou, Y.; Wen, Z. H.; Cui, S. M.; Guo, X. R.; Chen, J. H. Constructing 2D Porous Graphitic C₃N₄ Nanosheets/Nitrogen-Doped Graphene/Layered MoS₂ Ternary Nanojunction with Enhanced Photoelectrochemical Activity. *Adv. Mater.* **2013**, *25* (43), 6291–6297. <https://doi.org/10.1002/ADMA.201303116>.
- (79) Mushtaq, M. A.; Arif, M.; Fang, X.; Yasin, G.; Ye, W.; Basharat, M.; Zhou, B.; Yang, S.; Ji, S.; Yan, D. Photoelectrochemical Reduction of N₂ to NH₃ under Ambient Conditions through Hierarchical MoSe₂@g-C₃N₄ Heterojunctions. *J. Mater. Chem. A* **2021**, *9* (5), 2742–2753. <https://doi.org/10.1039/D0TA10620H>.
- (80) Ng, S.; Ghosh, K.; Vyskocil, J.; Pumera, M. Two-Dimensional Vanadium Sulfide Flexible Graphite/Polymer Films for near-Infrared Photoelectrocatalysis and Electrochemical Energy Storage. *Chem. Eng. J.* **2022**, *435*, 135131. <https://doi.org/10.1016/J.CEJ.2022.135131>.
- (81) Shao, G.; Lu, Y.; Hong, J.; Xue, X. X.; Huang, J.; Xu, Z.; Lu, X.; Jin, Y.; Liu, X.; Li, H.; Hu, S.; Suenaga, K.; Han, Z.; Jiang, Y.; Li, S.; Feng, Y.; Pan, A.; Lin, Y. C.; Cao, Y.; Liu, S. Seamlessly Splicing Metallic SnxMo_{1-x}S₂ at MoS₂ Edge for Enhanced Photoelectrocatalytic Performance in Microreactor. *Adv. Sci.* **2020**, *7* (24), 2002172. <https://doi.org/10.1002/ADVS.202002172>.
- (82) Kecsenovity, E.; Endrődi, B.; Tóth, P. S.; Zou, Y.; Dryfe, R. A. W.; Rajeshwar, K.; Janáky, C. Enhanced Photoelectrochemical Performance of Cuprous Oxide/Graphene Nanohybrids. *J. Am. Chem. Soc.* **2017**, *139* (19), 6682–6692. https://doi.org/10.1021/JACS.7B01820/ASSET/IMAGES/LARGE/JA-2017-01820T_0011.JPEG.
- (83) Paul, K. K.; Sreekanth, N.; Biroju, R. K.; Pattison, A. J.; Escalera-López, D.; Guha, A.; Narayanan, T. N.; Rees, N. V.; Theis, W.; Giri, P. K. Strongly Enhanced Visible Light Photoelectrocatalytic Hydrogen Evolution Reaction in an N-Doped MoS₂/TiO₂ (B)

- Heterojunction by Selective Decoration of Platinum Nanoparticles at the MoS₂ Edge Sites. *J. Mater. Chem. A* **2018**, *6* (45), 22681–22696. <https://doi.org/10.1039/C8TA06783J>.
- (84) Zheng, X.; Guo, Z.; Zhang, G.; Li, H.; Zhang, J.; Xu, Q. Building a Lateral/Vertical 1T-2H MoS₂/Au Heterostructure for Enhanced Photoelectrocatalysis and Surface Enhanced Raman Scattering. *J. Mater. Chem. A* **2019**, *7* (34), 19922–19928. <https://doi.org/10.1039/C9TA06091J>.
- (85) Yu, M. S.; Jesudass, S. C.; Surendran, S.; Kim, J. Y.; Sim, U.; Han, M. K. Synergistic Interaction of MoS₂Nanoflakes on La₂Zr₂O₇Nanofibers for Improving Photoelectrochemical Nitrogen Reduction. *ACS Appl. Mater. Interfaces* **2022**, *14* (28), 31889–31899. https://doi.org/10.1021/ACSAMI.2C05653/ASSET/IMAGES/MEDIUM/AM2C05653_M017.GIF.
- (86) Choi, S.; Kim, C.; Lee, J. Y.; Lee, T. H.; Kwon, K. C.; Kang, S.; Lee, S. A.; Choi, K. S.; Suh, J. M.; Hong, K.; Jun, S. E.; Kim, W. K.; Ahn, S. H.; Han, S.; Kim, S. Y.; Lee, C. H.; Jang, H. W. Vertically Aligned MoS₂ Thin Film Catalysts with Fe-Ni Sulfide Nanoparticles by One-Step Sulfurization for Efficient Solar Water Reduction. *Chem. Eng. J.* **2021**, *418*. <https://doi.org/10.1016/J.CEJ.2021.129369>.
- (87) Iqbal, N. Tailoring G-C₃N₄ with Lanthanum and Cobalt Oxides for Enhanced Photoelectrochemical and Photocatalytic Activity. *Catalysts* **2022**, *12* (1), 15. <https://doi.org/10.3390/CATAL12010015/S1>.
- (88) Zhu, C.; Xu, Q.; Liu, W.; Ren, Y. CO₂-Assisted Fabrication of Novel Heterostructures of h-MoO₃/1T-MoS₂ for Enhanced Photoelectrocatalytic Performance. *Appl. Surf. Sci.* **2017**, *425*, 56–62. <https://doi.org/10.1016/J.APSUSC.2017.06.248>.
- (89) Jian, L.; Wang, C.; Li, M.; Yan, J.; Wang, P.; Song, Y.; Wang, G.; Zhang, X.; Liu, X.; Fu, Y.; Ma, H. Constructing Outstanding 1D/2D Co₃O₄/NiMnO₃ Heterostructure to Promote the PEC Efficiency for Water Pollution Remediation. *J. Alloys Compd.* **2023**, *947*, 169411. <https://doi.org/10.1016/J.JALLCOM.2023.169411>.
- (90) Paul, K. K.; Sreekanth, N.; Biroju, R. K.; Narayanan, T. N.; Giri, P. K. Solar Light Driven Photoelectrocatalytic Hydrogen Evolution and Dye Degradation by Metal-Free Few-Layer MoS₂ Nanoflower/TiO₂(B) Nanobelts Heterostructure. *Sol. Energy Mater. Sol. Cells* **2018**, *185*, 364–374. <https://doi.org/10.1016/J.SOLMAT.2018.05.056>.
- (91) Sagara, N.; Kamimura, S.; Tsubota, T.; Ohno, T. Photoelectrochemical CO₂ Reduction by a P-Type Boron-Doped g-C₃N₄ Electrode under Visible Light. *Appl. Catal. B Environ.* **2016**, *192*, 193–198. <https://doi.org/10.1016/J.APCATB.2016.03.055>.
- (92) Yang, M.-Q.; Dan, J.; Pennycook, S. J.; Lu, X.; Zhu, H.; Xu, Q.-H.; Jin Fan, H.; Wei Ho, G. Ultrathin Nickel Boron Oxide Nanosheets Assembled Vertically on Graphene: A New Hybrid 2D Material for Enhanced Photo/Electro-Catalysis †. **2017**, *4*, 885. <https://doi.org/10.1039/c7mh00314e>.
- (93) Abid, N.; Khan, A. M.; Shujait, S.; Chaudhary, K.; Ikram, M.; Imran, M.; Haider, J.; Khan, M.; Khan, Q.; Maqbool, M. Synthesis of Nanomaterials Using Various Top-down and Bottom-up Approaches, Influencing Factors, Advantages, and Disadvantages: A Review. *Adv. Colloid Interface Sci.* **2022**, *300*, 102597. <https://doi.org/10.1016/J.CIS.2021.102597>.
- (94) Zhen, Guo; Li, T. *Fundamentals and Application of Nanomaterials*; Artech House: Norwood, MA 02062, 2009.
- (95) Mehtab, A.; Mao, Y.; M. Alshehri, S.; Ahmad, T. Photo/Electrocatalytic Hydrogen Evolution Using Type-II Cu₂O/g-C₃N₄ Heterostructure: Density Functional Theory Addresses the Improved Charge Transport Efficiency. *J. Colloid Interface Sci.* **2023**, *652*, 1467–1480. <https://doi.org/10.1016/J.CIS.2023.08.144>.
- (96) Cheng, S.; Sun, Z.; Lim, K. H.; Wibowo, A. A.; Zhang, T.; Du, T.; Liu, L.; Nguyen, H. T.; Li, G. K.; Yin, Z.; Kawi, S. Dual-Defective Two-Dimensional/Two-Dimensional Z-Scheme Heterojunctions for CO₂ Reduction. *ACS Catal.* **2023**, *13* (11), 7221–7229. https://doi.org/10.1021/ACSCATAL.3C00219/ASSET/IMAGE/S/LARGE/CS3C00219_0006.JPEG.
- (97) Wang, Q.; Wang, X.; Yu, Z.; Jiang, X.; Chen, J.; Tao, L.; Wang, M.; Shen, Y. Artificial Photosynthesis of Ethanol Using Type-II g-C₃N₄/ZnTe Heterojunction in Photoelectrochemical CO₂ Reduction System. *Nano Energy* **2019**, *60*, 827–835. <https://doi.org/10.1016/J.NANOEN.2019.04.037>.
- (98) Guru, S.; Kumar, S.; Bellamkonda, S.; Gangavarapu, R. R. Synthesis of CuTi-LDH Supported on g-C₃N₄ for Electrochemical and Photoelectrochemical Oxygen Evolution Reactions. *Int. J. Hydrogen Energy* **2021**, *46* (30), 16414–16430. <https://doi.org/10.1016/J.IJHYDENE.2020.08.102>.
- (99) Ma, Y.; Dong, Y. X.; Wang, B.; Ren, S. W.; Cao, J. T.; Liu, Y. M. CdS:Mn-Sensitized 2D/2D Heterostructured g-C₃N₄-MoS₂ with Excellent Photoelectrochemical Performance for Ultrasensitive Immunosensing Platform. *Talanta* **2020**, *207*. <https://doi.org/10.1016/J.TALANTA.2019.120288>.
- (100) Hou, M.; Cui, L.; Su, F.; Dong, X.; Dang, H. Two-Step Calcination Synthesis of Z-Scheme α-Fe₂O₃/Few-Layer g-C₃N₄ Composite with Enhanced Hydrogen Production and Photodegradation under Visible Light. *J. Chinese Chem. Soc.* **2020**, *67* (11), 2050–2061. <https://doi.org/10.1002/JCCS.202000127>.
- (101) Li, M.; Lu, Q.; Liu, M.; Yin, P.; Wu, C.; Li, H.; Zhang, Y.; Yao, S. Photoinduced Charge Separation via the Double-Electron Transfer Mechanism in Nitrogen Vacancies g-C₃N₅/BiOBr for the Photoelectrochemical Nitrogen Reduction. *ACS Appl. Mater. Interfaces* **2020**, *12* (34), 38266–38274. https://doi.org/10.1021/ACSAMI.0C11894/SUPPL_FILE/AM0C11894_SI_001.PDF.
- (102) Jiménez-Arévalo, N.; Flores, E.; Giampietri, A.; Sbroscia, M.; Betti, M. G.; Mariani, C.; Ares, J. R.; Ferrer, I. J.; Leardini, F. Borocarbonitride Layers on Titanium Dioxide Nanoribbons for Efficient Photoelectrocatalytic Water Splitting. *Materials (Basel)*. **2021**, *14* (19), 5490. <https://doi.org/10.3390/MA14195490/S1>.
- (103) Sreedhar, A.; Noh, J. S. Interfacial Engineering Insights of Promising Monolayer 2D Ti₃C₂ MXene Anchored Flake-like ZnO Thin Films for Improved PEC Water Splitting. *J. Electroanal. Chem.* **2021**, *883*. <https://doi.org/10.1016/J.JELECHEM.2021.115044>.
- (104) Li, Y.; Lai, Z.; Huang, Z.; Wang, H.; Zhao, C.; Ruan, G.; Du, F. Fabrication of BiOBr/MoS₂/Graphene Oxide Composites for Efficient Adsorption and Photocatalytic Removal of Tetracycline Antibiotics. *Appl. Surf. Sci.* **2021**, *550*, 149342. <https://doi.org/10.1016/J.APSUSC.2021.149342>.
- (105) Hong, S.; Rhee, C. K.; Sohn, Y. Photoelectrochemical Hydrogen Evolution and CO₂ Reduction over MoS₂/Si and MoSe₂/Si Nanostructures by Combined Photoelectrochemical Deposition and Rapid-Thermal Annealing Process. *Catal. 2019, Vol. 9, Page 494* **2019**, *9* (6), 494. <https://doi.org/10.3390/CATAL9060494>.
- (106) Paulraj, G.; Venkatesh, P. S.; Dharmaraj, P.; Gopalakrishnan, S.; Jegannathan, K. Stable and Highly Efficient MoS₂/Si NWs Hybrid Heterostructure for Photoelectrocatalytic Hydrogen Evolution Reaction. *Int. J. Hydrogen Energy* **2020**, *45* (3), 1793–1801. <https://doi.org/10.1016/J.IJHYDENE.2019.11.051>.
- (107) Seo, D. B.; Dongquoc, V.; Jayarathna, R. A.; Lee, S.; Lee, J. H.; Kim, E. T. Rational Heterojunction Design of 1D WO₃ Nanorods Decorated with Vertical 2D MoS₂ Nanosheets for Enhanced Photoelectrochemical Performance. *J. Alloys Compd.* **2022**, *911*, 165090. <https://doi.org/10.1016/J.JALLCOM.2022.165090>.
- (108) Zheng, Z.; Ng, Y. H.; Tang, Y.; Li, Y.; Chen, W.; Wang, J.; Li, X.; Li, L. Visible-Light-Driven Photoelectrocatalytic Activation of Chloride by Nanoporous MoS₂@BiVO₄ Photoanode for Enhanced Degradation of Bisphenol A. *Chemosphere* **2021**, *263*. <https://doi.org/10.1016/J.CHEMOSPHERE.2020.128279>.
- (109) Sreedhar, A.; Ta, Q. T. H.; Noh, J. S. Rational Engineering of Morphology Modulated Ti-ZnO Thin Films Coupled Monolayer Ti₃C₂ MXene for Efficient Visible Light PEC Water Splitting Activity. *J. Electroanal. Chem.* **2022**, *921*, 116703. <https://doi.org/10.1016/J.JELECHEM.2022.116703>.
- (110) Samanta, B.; Morales-García, Á.; Illas, F.; Goga, N.; Anta, J. A.; Calero, S.; Bieberle-Hütter, A.; Libisch, F.; Muñoz-García, A. B.; Pavone, M.; Casparý Toroker, M. Challenges of Modeling Nanostructured Materials for Photocatalytic Water Splitting. *Chem. Soc. Rev.* **2022**, *51* (9), 3794–3818. <https://doi.org/10.1039/D1CS00648G>.
- (111) Bhandari, S.; Rangarajan, S.; Mavrikakis, M. Combining Computational Modeling with Reaction Kinetics Experiments for

- Elucidating the in Situ Nature of the Active Site in Catalysis. *Acc. Chem. Res.* **2020**, *53* (9), 1893–1904. https://doi.org/10.1021/ACS.ACCOUNTS.0C00340/ASSET/IMAGES/LARGE/AR0C00340_0006.JPEG.
- (112) Hohenberg, P.; Kohn, W. Inhomogeneous Electron Gas. *Phys. Rev.* **1964**, *136* (3B), B864. <https://doi.org/10.1103/PhysRev.136.B864>.
- (113) Kohn, W.; Sham, L. J. Self-Consistent Equations Including Exchange and Correlation Effects. *Phys. Rev.* **1965**, *140* (4A), A1133. <https://doi.org/10.1103/PhysRev.140.A1133>.
- (114) Zhao, Y.; Zhang, S.; Shi, R.; Waterhouse, G. I. N.; Tang, J.; Zhang, T. Two-Dimensional Photocatalyst Design: A Critical Review of Recent Experimental and Computational Advances. *Mater. Today* **2020**, *34*, 78–91. <https://doi.org/10.1016/J.MATTOD.2019.10.022>.
- (115) Zhang, C.; Chen, G.; Si, Y.; Liu, M. Surface Modeling of Photocatalytic Materials for Water Splitting. *Phys. Chem. Chem. Phys.* **2022**, *24* (3), 1237–1261. <https://doi.org/10.1039/D1CP04352H>.
- (116) Di, J.; Jiang, W. Recent Progress of Low-Dimensional Metal Sulfides Photocatalysts for Energy and Environmental Applications. *Mater. Today Catal.* **2023**, *1*, 100001. <https://doi.org/10.1016/J.MTCATA.2023.100001>.
- (117) Li, Y.; Gao, C.; Long, R.; Xiong, Y. Photocatalyst Design Based on Two-Dimensional Materials. *Mater. Today Chem.* **2019**, *11*, 197–216. <https://doi.org/10.1016/J.MTCHEM.2018.11.002>.
- (118) Qin, R.; Zheng, N. Catalysis Selects Its Own Favorite Facets. *Chem* **2019**, *5* (8), 1935–1937. <https://doi.org/10.1016/J.CHEMPR.2019.07.011>.
- (119) Lazar, P.; Otyepková, E.; Banáš, P.; Fargašová, A.; Šafařová, K.; Lapčík, L.; Pechoušek, J.; Zbořil, R.; Otyepka, M. The Nature of High Surface Energy Sites in Graphene and Graphite. *Carbon N. Y.* **2014**, *73*, 448–453. <https://doi.org/10.1016/J.CARBON.2014.03.010>.
- (120) Klimeš, J.; Bowler, D. R.; Michaelides, A. Chemical Accuracy for the van Der Waals Density Functional. *J. Phys. Condens. Matter* **2009**, *22* (2), 022201. <https://doi.org/10.1088/0953-8984/22/2/022201>.
- (121) Lee, K.; Murray, É. D.; Kong, L.; Lundqvist, B. I.; Langreth, D. C. Higher-Accuracy van Der Waals Density Functional. *Phys. Rev. B - Condens. Matter Mater. Phys.* **2010**, *82* (8), 081101. <https://doi.org/10.1103/PHYSREVB.82.081101/FIGURES/2/MEDIUM>.
- (122) Grimme, S. Semiempirical GGA-Type Density Functional Constructed with a Long-Range Dispersion Correction. *J. Comput. Chem.* **2006**, *27* (15), 1787–1799. <https://doi.org/10.1002/JCC.20495>.
- (123) Grimme, S. Accurate Description of van Der Waals Complexes by Density Functional Theory Including Empirical Corrections. *J. Comput. Chem.* **2004**, *25* (12), 1463–1473. <https://doi.org/10.1002/JCC.20078>.
- (124) Che, M. Nobel Prize in Chemistry 1912 to Sabatier: Organic Chemistry or Catalysis? *Catal. Today* **2013**, *218–219*, 162–171. <https://doi.org/10.1016/J.CATTOD.2013.07.006>.
- (125) Trasatti, S. Work Function, Electronegativity, and Electrochemical Behaviour of Metals: III. Electrolytic Hydrogen Evolution in Acid Solutions. *J. Electroanal. Chem. Interfacial Electrochem.* **1972**, *39* (1), 163–184. [https://doi.org/10.1016/S0022-0728\(72\)80485-6](https://doi.org/10.1016/S0022-0728(72)80485-6).
- (126) Quaino, P.; Juarez, F.; Santos, E.; Schmickler, W. Volcano Plots in Hydrogen Electrocatalysis – Uses and Abuses. *Beilstein J. Nanotechnol.* **2014**, *5* (1), 846–854. <https://doi.org/10.3762/BJNANO.5.96>.
- (127) Heenen, H. H.; Gauthier, J. A.; Kristoffersen, H. H.; Ludwig, T.; Chan, K. Solvation at Metal/Water Interfaces: An Ab Initio Molecular Dynamics Benchmark of Common Computational Approaches. *J. Chem. Phys.* **2020**, *152* (14). <https://doi.org/10.1063/1.5144912/197884>.
- (128) Van Duin, A. C. T.; Dasgupta, S.; Lorant, F.; Goddard, W. A. ReaxFF: A Reactive Force Field for Hydrocarbons. *J. Phys. Chem. A* **2001**, *105* (41), 9396–9409. <https://doi.org/10.1021/JP004368U/ASSET/IMAGES/LARGE/JP004368UF00025.JPEG>.
- (129) Hossain, M. D.; Zhang, Q.; Cheng, T.; Goddard, W. A.; Luo, Z. Graphitization of Low-Density Amorphous Carbon for Electrocatalysis Electrodes from ReaxFF Reactive Dynamics. *Carbon N. Y.* **2021**, *183*, 940–947. <https://doi.org/10.1016/J.CARBON.2021.07.080>.
- (130) Cheng, T.; Xiao, H.; Goddard, W. A. Full Atomistic Reaction Mechanism with Kinetics for CO Reduction on Cu(100) from Ab Initio Molecular Dynamics Free-Energy Calculations at 298 K. *Proc. Natl. Acad. Sci. U. S. A.* **2017**, *114* (8), 1795–1800. https://doi.org/10.1073/PNAS.1612106114/SUPPL_FILE/PNAS.201612106SI.PDF.
- (131) Cheng, T.; Xiao, H.; Goddard, W. A. Free-Energy Barriers and Reaction Mechanisms for the Electrochemical Reduction of CO on the Cu(100) Surface, Including Multiple Layers of Explicit Solvent at PH 0. *J. Phys. Chem. Lett.* **2015**, *6* (23), 4767–4773. https://doi.org/10.1021/ACS.JPCLETT.5B02247/ASSET/IMAGES/LARGE/JZ-2015-022473_0003.JPEG.
- (132) Sprik, M.; Ciccotti, G. Free Energy from Constrained Molecular Dynamics. *J. Chem. Phys.* **1998**, *109* (18), 7737–7744. <https://doi.org/10.1063/1.477419>.
- (133) Lim, H. K.; Lee, H.; Kim, H. A Seamless Grid-Based Interface for Mean-Field QM/MM Coupled with Efficient Solvation Free Energy Calculations. *J. Chem. Theory Comput.* **2016**, *12* (10), 5088–5099. https://doi.org/10.1021/ACS.JCTC.6B00469/SUPPL_FILE/CT6B00469_SI_001.PDF.
- (134) Cao, H.; Xia, G. J.; Chen, J. W.; Yan, H. M.; Huang, Z.; Wang, Y. G. Mechanistic Insight into the Oxygen Reduction Reaction on the Mn-N4/C Single-Atom Catalyst: The Role of the Solvent Environment. *J. Phys. Chem. C* **2020**, *124* (13), 7287–7294. https://doi.org/10.1021/ACS.JPC.0C00352/ASSET/IMAGES/LARGE/JP0C00352_0007.JPEG.
- (135) Zhao, X.; Liu, Y. Unveiling the Active Structure of Single Nickel Atom Catalysis: Critical Roles of Charge Capacity and Hydrogen Bonding. *J. Am. Chem. Soc.* **2020**, *142* (12), 5773–5777. https://doi.org/10.1021/JACS.9B13872/ASSET/IMAGES/LARGE/JA9B13872_0003.JPEG.
- (136) Rappé, A. K.; Goddard, W. A. Charge Equilibration for Molecular Dynamics Simulations. *J. Phys. Chem.* **1991**, *95* (8), 3358–3363. https://doi.org/10.1021/J100161A070/ASSET/J100161A070.FP.PNG_V03.
- (137) Lu, K.; He, Y.; Huo, C. F.; Guo, W. P.; Peng, Q.; Yang, Y.; Li, Y. W.; Wen, X. D. Developing ReaxFF to Visit CO Adsorption and Dissociation on Iron Surfaces. *J. Phys. Chem. C* **2018**, *122* (48), 27582–27589. https://doi.org/10.1021/ACS.JPC.8B10427/SUPPL_FILE/JP8B10427_SI_001.TXT.
- (138) Shin, S. J.; Choi, H.; Ringe, S.; Won, D. H.; Oh, H. S.; Kim, D. H.; Lee, T.; Nam, D. H.; Kim, H.; Choi, C. H. A Unifying Mechanism for Cation Effect Modulating C1 and C2 Productions from CO2 Electroreduction. *Nat. Commun.* **2022**, *131* **2022**, 1 (1), 1–10. <https://doi.org/10.1038/s41467-022-33199-8>.
- (139) Wang, M.; Osella, S.; Brescia, R.; Liu, Z.; Gallego, J.; Cattelan, M.; Crisci, M.; Agnoli, S.; Gatti, T. 2D MoS₂/BiOBr van Der Waals Heterojunctions by Liquid-Phase Exfoliation as Photoelectrocatalysts for Hydrogen Evolution. *Nanoscale* **2023**, *15* (2), 522–531. <https://doi.org/10.1039/D2NR04970H>.
- (140) Back, S.; Lim, J.; Kim, N. Y.; Kim, Y. H.; Jung, Y. Single-Atom Catalysts for CO₂ Electroreduction with Significant Activity and Selectivity Improvements. *Chem. Sci.* **2017**, *8* (2), 1090–1096. <https://doi.org/10.1039/C6SC03911A>.
- (141) Perdew, J. P.; Zunger, A. Self-Interaction Correction to Density-Functional Approximations for Many-Electron Systems. *Phys. Rev. B* **1981**, *23* (10), 5048. <https://doi.org/10.1103/PhysRevB.23.5048>.
- (142) Perdew, J. P.; Chevary, J. A.; Vosko, S. H.; Jackson, K. A.; Pederson, M. R.; Singh, D. J.; Fiolhais, C. Atoms, Molecules, Solids, and Surfaces: Applications of the Generalized Gradient Approximation for Exchange and Correlation. *Phys. Rev. B* **1992**, *46* (11), 6671. <https://doi.org/10.1103/PhysRevB.46.6671>.
- (143) Cohen, A. J.; Mori-Sánchez, P.; Yang, W. Insights into Current Limitations of Density Functional Theory. *Science (80-.)* **2008**, *321* (5890), 792–794. https://doi.org/10.1126/SCIENCE.1158722/ASSET/A8819499-1369-4566-926A-0BEA537FD9D6/ASSETS/GRAPHIC/321_792_F2.JPEG.

- (144) Heyd, J.; Peralta, J. E.; Scuseria, G. E.; Martin, R. L. Energy Band Gaps and Lattice Parameters Evaluated with the Heyd-Scuseria-Ernzerhof Screened Hybrid Functional. *J. Chem. Phys.* **2005**, *123* (17), 174101. <https://doi.org/10.1063/1.2085170/917481>.
- (145) Onida, G.; Reining, L.; Rubio, A. Electronic Excitations: Density-Functional versus Many-Body Green's-Function Approaches. *Rev. Mod. Phys.* **2002**, *74* (2), 601. <https://doi.org/10.1103/RevModPhys.74.601>.
- (146) Morales-García, Á.; Viñes, F.; Sousa, C.; Illas, F. Toward a Rigorous Theoretical Description of Photocatalysis Using Realistic Models. *J. Phys. Chem. Lett.* **2023**, *14* (15), 3712–3720. https://doi.org/10.1021/ACS.JPCLETT.3C00359/ASSET/IMAGES/LARGE/JZ3C00359_0004.JPEG.
- (147) Mo, Z.; Di, J.; Yan, P.; Lv, C.; Zhu, X.; Liu, D.; Song, Y.; Liu, C.; Yu, Q.; Li, H.; Lei, Y.; Xu, H.; Yan, Q.; Mo, Z.; Yan, P.; Zhu, X.; Yu, Q.; Li, H.; Lei, Y.; Xu, H.; Di, J.; Lv, C.; Liu, D.; Yan, Q.; Song, Y.; Liu, C. An All-Organic D-A System for Visible-Light-Driven Overall Water Splitting. *Small* **2020**, *16* (48), 2003914. <https://doi.org/10.1002/SMLL.202003914>.
- (148) Henkelman, G.; Arnaldsson, A.; Jónsson, H. A Fast and Robust Algorithm for Bader Decomposition of Charge Density. *Comput. Mater. Sci.* **2006**, *36* (3), 354–360. <https://doi.org/10.1016/J.COMMATSCI.2005.04.010>.
- (149) Nam, Y.; Li, L.; Lee, J. Y.; Prezhdo, O. V. Size and Shape Effects on Charge Recombination Dynamics of TiO₂ Nanoclusters. *J. Phys. Chem. C* **2018**, *122* (9), 5201–5208. https://doi.org/10.1021/ACS.JPC.8B00691/ASSET/IMAGES/LARGE/JP-2018-00691H_0005.JPEG.
- (150) Singh, A. K.; Mathew, K.; Zhuang, H. L.; Hennig, R. G. Computational Screening of 2D Materials for Photocatalysis. *J. Phys. Chem. Lett.* **2015**, *6* (6), 1087–1098. https://doi.org/10.1021/JZ502646D/ASSET/IMAGES/LARGE/JZ-2014-02646D_0008.JPEG.
- (151) Runge, E.; Gross, E. K. U. Density-Functional Theory for Time-Dependent Systems. *Phys. Rev. Lett.* **1984**, *52* (12), 997. <https://doi.org/10.1103/PhysRevLett.52.997>.
- (152) Furche, F.; Ahlrichs, R. Adiabatic Time-Dependent Density Functional Methods for Excited State Properties. *J. Chem. Phys.* **2002**, *117* (16), 7433–7447. <https://doi.org/10.1063/1.1508368>.
- (153) Saalman, U.; Schmidt, R. Non-Adiabatic Quantum Molecular Dynamics: Basic Formalism and Case Study. *Zeitschrift für Phys. D-Atoms Mol. Clust.* **1996**, *38* (2), 153–163. <https://doi.org/10.1007/S004600050077/METRICS>.
- (154) Tully, J. C. Perspective: Nonadiabatic Dynamics Theory. *J. Chem. Phys.* **2012**, *137* (22), 22–301. <https://doi.org/10.1063/1.4757762/194788>.
- (155) Kolesov, G.; Vinichenko, D.; Tritsarlis, G. A.; Friend, C. M.; Kaxiras, E. Anatomy of the Photochemical Reaction: Excited-State Dynamics Reveals the C-H Acidity Mechanism of Methoxy Photo-Oxidation on Titania. *J. Phys. Chem. Lett.* **2015**, *6* (9), 1624–1627. https://doi.org/10.1021/ACS.JPCLETT.5B00429/SUPPL_FILE/JZ5B00429_SI_001.PDF.
- (156) Tully, J. C. Molecular Dynamics with Electronic Transitions. *J. Chem. Phys.* **1990**, *93* (2), 1061–1071. <https://doi.org/10.1063/1.459170>.
- (157) Craig, C. F.; Duncan, W. R.; Prezhdo, O. V. Trajectory Surface Hopping in the Time-Dependent Kohn-Sham Approach for Electron-Nuclear Dynamics. *Phys. Rev. Lett.* **2005**, *95* (16), 163001. <https://doi.org/10.1103/PHYSREVLETT.95.163001/FIGURES/2/MEDIUM>.
- (158) Zheng, Q.; Chu, W.; Zhao, C.; Zhang, L.; Guo, H.; Wang, Y.; Jiang, X.; Zhao, J. Ab Initio Nonadiabatic Molecular Dynamics Investigations on the Excited Carriers in Condensed Matter Systems. *Wiley Interdiscip. Rev. Comput. Mol. Sci.* **2019**, *9* (6), e1411. <https://doi.org/10.1002/WCMS.1411>.
- (159) Niu, X.; Bai, X.; Zhou, Z.; Wang, J. Rational Design and Characterization of Direct Z-Scheme Photocatalyst for Overall Water Splitting from Excited State Dynamics Simulations. *ACS Catal.* **2020**, *10* (3), 1976–1983. https://doi.org/10.1021/ACSCATAL.9B04753/ASSET/IMAGE/MEDIUM/CS9B04753_M003.GIF.
- (160) Akimov, A. V.; Prezhdo, O. V. The PYXAID Program for Non-Adiabatic Molecular Dynamics in Condensed Matter Systems. *J. Chem. Theory Comput.* **2013**, *9* (11), 4959–4972. https://doi.org/10.1021/CT400641N/SUPPL_FILE/CT400641N_SI_001.PDF.
- (161) Wang, D.; Wang, H.; Hu, P. Identifying the Distinct Features of Geometric Structures for Hole Trapping to Generate Radicals on Rutile TiO₂(110) in Photooxidation Using Density Functional Theory Calculations with Hybrid Functional. *Phys. Chem. Chem. Phys.* **2014**, *17* (3), 1549–1555. <https://doi.org/10.1039/C4CP04159C>.
- (162) Car, R.; Parrinello, M. Unified Approach for Molecular Dynamics and Density-Functional Theory. *Phys. Rev. Lett.* **1985**, *55* (22), 2471. <https://doi.org/10.1103/PhysRevLett.55.2471>.
- (163) Salpeter, E. E.; Bethe, H. A. A Relativistic Equation for Bound-State Problems. *Phys. Rev.* **1951**, *84* (6), 1232–1242. <https://doi.org/10.1103/PhysRev.84.1232>.
- (164) Golze, D.; Dvorak, M.; Rinke, P. The GW Compendium: A Practical Guide to Theoretical Photoemission Spectroscopy. *Front. Chem.* **2019**, *7*, 443014. <https://doi.org/10.3389/FCHEM.2019.00377/BIBTEX>.
- (165) Hedin, L. New Method for Calculating the One-Particle Green's Function with Application to the Electron-Gas Problem. *Phys. Rev.* **1965**, *139* (3A), A796. <https://doi.org/10.1103/PhysRev.139.A796>.
- (166) Elliott, P.; Goldson, S.; Canahui, C.; Maitra, N. T. Perspectives on Double-Excitations in TDDFT. *Chem. Phys.* **2011**, *391* (1), 110–119. <https://doi.org/10.1016/j.chemphys.2011.03.020>.
- (167) Parac, M.; Grimme, S. A TDDFT Study of the Lowest Excitation Energies of Polycyclic Aromatic Hydrocarbons. *Chem. Phys.* **2003**, *292* (1), 11–21. [https://doi.org/10.1016/S0301-0104\(03\)00250-7](https://doi.org/10.1016/S0301-0104(03)00250-7).
- (168) Langer, M.; Palonciová, M.; Medved', M.; Pykal, M.; Nachtigallová, D.; Shi, B.; Aquino, A. J. A.; Lischka, H.; Otýepka, M. Progress and Challenges in Understanding of Photoluminescence Properties of Carbon Dots Based on Theoretical Computations. *Applied Materials Today*. Elsevier Ltd March 2021, p 100924. <https://doi.org/10.1016/j.apmt.2020.100924>.
- (169) Dreuw, A.; Head-Gordon, M. Failure of Time-Dependent Density Functional Theory for Long-Range Charge-Transfer Excited States: The Zincbacteriochlorin-Bacteriochlorin and Bacteriochlorophyll-Spheroidene Complexes. *J. Am. Chem. Soc.* **2004**, *126* (12), 4007–4016. https://doi.org/10.1021/JA039556N/SUPPL_FILE/JA039556NS_I20040114_085038.PDF.
- (170) Wang, L.; Akimov, A.; Prezhdo, O. V. Recent Progress in Surface Hopping: 2011–2015. *J. Phys. Chem. Lett.* **2016**, *7* (11), 2100–2112. <https://doi.org/10.1021/ACS.JPCLETT.6B00710>.
- (171) Hörmann, N. G.; Andreussi, O.; Marzari, N. Grand Canonical Simulations of Electrochemical Interfaces in Implicit Solvation Models. *J. Chem. Phys.* **2019**, *150* (4), 41730. <https://doi.org/10.1063/1.5054580/1062335>.
- (172) Zhang, H.; Yu, D.; Ji, Z.; al; Gutiérrez, A.; Gutiérrez, S.; García, G. Grand Canonical Rate Theory for Electrochemical and Electrocatalytic Systems I: General Formulation and Proton-Coupled Electron Transfer Reactions. *J. Electrochem. Soc.* **2020**, *167* (11), 116518. <https://doi.org/10.1149/1945-7111/ABA54B>.
- (173) Hörmann, N. G.; Marzari, N.; Reuter, K. Electrosorption at Metal Surfaces from First Principles. *npj Comput. Mater.* **2020**, *6* (1), 1–10. <https://doi.org/10.1038/s41524-020-00394-4>.
- (174) Nørskov, J. K.; Rossmeisl, J.; Logadottir, A.; Lindqvist, L.; Kitchin, J. R.; Bligaard, T.; Jónsson, H. Origin of the Overpotential for Oxygen Reduction at a Fuel-Cell Cathode. *J. Phys. Chem. B* **2004**, *108* (46), 17886–17892. <https://doi.org/10.1021/JP047349J>.
- (175) Nørskov, J. K.; Bligaard, T.; Logadottir, A.; Kitchin, J. R.; Chen, J. G.; Pandalov, S.; Stimming, U. Trends in the Exchange Current for Hydrogen Evolution. *J. Electrochem. Soc.* **2005**, *152* (3), J23. <https://doi.org/10.1149/1.1856988/XML>.
- (176) Peterson, A. A.; Abild-Pedersen, F.; Studt, F.; Rossmeisl, J.; Nørskov, J. K. How Copper Catalyzes the Electroreduction of Carbon Dioxide into Hydrocarbon Fuels. *Energy Environ. Sci.* **2010**, *3* (9), 1311–1315. <https://doi.org/10.1039/C0EE00071J>.
- (177) Huang, Y.; Nielsen, R. J.; Goddard, W. A. Reaction Mechanism for the Hydrogen Evolution Reaction on the Basal Plane Sulfur Vacancy Site of MoS₂ Using Grand Canonical Potential Kinetics.

- J. Am. Chem. Soc.* **2018**, *140* (48), 16773–16782. https://doi.org/10.1021/JACS.8B10016/ASSET/IMAGES/LARGE/JA-2018-10016M_0008.JPEG.
- (178) Chan, K.; Nørskov, J. K. Electrochemical Barriers Made Simple. *J. Phys. Chem. Lett.* **2015**, *6* (14), 2663–2668. https://doi.org/10.1021/ACS.JPCLETT.5B01043/ASSET/IMAGES/LARGE/JZ-2015-01043W_0005.JPEG.
- (179) Rossmelsl, J.; Qu, Z. W.; Zhu, H.; Kroes, G. J.; Nørskov, J. K. Electrolysis of Water on Oxide Surfaces. *J. Electroanal. Chem.* **2007**, *607* (1–2), 83–89. <https://doi.org/10.1016/J.JELECHEM.2006.11.008>.
- (180) Sundaraman, R.; Goddard, W. A.; Arias, T. A. Grand Canonical Electronic Density-Functional Theory: Algorithms and Applications to Electrochemistry. *J. Chem. Phys.* **2017**, *146* (11), 114104. https://doi.org/10.1063/1.4978411/16754493/114104_1_ACCEPTED_MANUSCRIPT.PDF.
- (181) Oberhofer, H. Electrocatalysis Beyond the Computational Hydrogen Electrode. *Handb. Mater. Model.* **2018**, 1–33. https://doi.org/10.1007/978-3-319-50257-1_9-1.
- (182) Zhao, X.; Levell, Z. H.; Yu, S.; Liu, Y. Atomistic Understanding of Two-Dimensional Electrocatalysts from First Principles. *Chem. Rev.* **2022**, *122* (12), 10675–10709. https://doi.org/10.1021/ACS.CHEMREV.1C00981/ASSET/IMAGES/LARGE/CR1C00981_0028.JPEG.
- (183) Abidi, N.; Lim, K. R. G.; Seh, Z. W.; Steinmann, S. N. Atomistic Modeling of Electrocatalysis: Are We There Yet? *Wiley Interdiscip. Rev. Comput. Mol. Sci.* **2021**, *11* (3), e1499. <https://doi.org/10.1002/WCMS.1499>.
- (184) Chan, K.; Nørskov, J. K. Potential Dependence of Electrochemical Barriers from Ab Initio Calculations. *J. Phys. Chem. Lett.* **2016**, *7* (9), 1686–1690. https://doi.org/10.1021/ACS.JPCLETT.6B00382/ASSET/IMAGES/MEDIUM/JZ-2016-003822_0007.GIF.
- (185) Shi, C.; Chan, K.; Yoo, J. S.; Nørskov, J. K. Barriers of Electrochemical CO₂ Reduction on Transition Metals. *Org. Process Res. Dev.* **2016**, *20* (8), 1424–1430. https://doi.org/10.1021/ACS.OPRD.6B00103/ASSET/IMAGES/LARGE/OP-2016-00103B_0005.JPEG.
- (186) Zhao, X.; Liu, Y. Origin of Selective Production of Hydrogen Peroxide by Electrochemical Oxygen Reduction. *J. Am. Chem. Soc.* **2021**, *143* (25), 9423–9428. https://doi.org/10.1021/JACS.1C02186/ASSET/IMAGES/LARGE/JA1C02186_0004.JPEG.
- (187) Lindgren, P.; Kastlunger, G.; Peterson, A. A. A Challenge to the G ~ 0 Interpretation of Hydrogen Evolution. *ACS Catal.* **2020**, *10* (1), 121–128. https://doi.org/10.1021/ACSCATAL.9B02799/ASSET/IMAGE/S/LARGE/CS9B02799_0005.JPEG.
- (188) Verma, A. M.; Honkala, K.; Melander, M. M. Computational Screening of Doped Graphene Electrodes for Alkaline CO₂ Reduction. *Front. Energy Res.* **2021**, *8*, 606742. <https://doi.org/10.3389/FENRG.2020.606742/BIBTEX>.
- (189) Hossain, M. D.; Liu, Z.; Liu, H.; Tyagi, A.; Rehman, F.; Li, J.; Amjadi, M.; Cai, Y.; Goddard, W. A.; Luo, Z. The Kinetics and Potential Dependence of the Hydrogen Evolution Reaction Optimized for the Basal-Plane Te Vacancy Site of MoTe₂. *Chem Catal.* **2023**, *3* (1), 100489. <https://doi.org/10.1016/J.CHECAT.2022.100489>.
- (190) Hossain, M. D.; Huang, Y.; Yu, T. H.; Goddard, W. A.; Luo, Z. Reaction Mechanism and Kinetics for CO₂ Reduction on Nickel Single Atom Catalysts from Quantum Mechanics. *Nat. Commun.* **2020**, *11* (1), 1–14. <https://doi.org/10.1038/s41467-020-16119-6>.
- (191) Osella, S.; III, W. A. G. CO₂ Reduction to Methane and Ethylene on a Single-Atom Catalyst: A Grand Canonical Quantum Mechanics Study. *J. Am. Chem. Soc.* **2023**. <https://doi.org/10.1021/JACS.3C05650>.
- (192) Kovačić, Ž.; Likozar, B.; Huš, M. Photocatalytic CO₂ Reduction: A Review of Ab Initio Mechanism, Kinetics, and Multiscale Modeling Simulations. *ACS Catal.* **2020**, 14984–15007. https://doi.org/10.1021/ACSCATAL.0C02557/ASSET/IMAGE/S/LARGE/CS0C02557_0007.JPEG.
- (193) Hansen, H. A.; Viswanathan, V.; Nørskov, J. K. Unifying Kinetic and Thermodynamic Analysis of 2 e⁻ and 4 e⁻ Reduction of Oxygen on Metal Surfaces. *J. Phys. Chem. C* **2014**, *118* (13), 6706–6718. https://doi.org/10.1021/JP4100608/SUPPL_FILE/JP4100608_SI_001.PDF.
- (194) Henkelman, G.; Uberuaga, B. P.; Jónsson, H. A Climbing Image Nudged Elastic Band Method for Finding Saddle Points and Minimum Energy Paths. *J. Chem. Phys.* **2000**, *113* (22), 9901–9904. <https://doi.org/10.1063/1.1329672>.
- (195) Henkelman, G.; Jónsson, H. Improved Tangent Estimate in the Nudged Elastic Band Method for Finding Minimum Energy Paths and Saddle Points. *J. Chem. Phys.* **2000**, *113* (22), 9978–9985. <https://doi.org/10.1063/1.1323224>.
- (196) Evans, M. G.; Polanyi, M. Inertia and Driving Force of Chemical Reactions. *Trans. Faraday Soc.* **1938**, *34* (0), 11–24. <https://doi.org/10.1039/TF9383400011>.
- (197) Santen, R. A. V.; Neurock, M.; Shetty, S. G. Reactivity Theory of Transition-Metal Surfaces: A Brønsted-Evans-Polanyi Linear Activation Energy-Free-Energy Analysis. *Chem. Rev.* **2010**, *110* (4), 2005–2048. https://doi.org/10.1021/CR9001808/ASSET/IMAGES/LARGE/CR-2009-001808_0034.JPEG.
- (198) Akhade, S. A.; Nidzyn, R. M.; Rostamikia, G.; Janik, M. J. Using Brønsted-Evans-Polanyi Relations to Predict Electrode Potential-Dependent Activation Energies. *Catal. Today* **2018**, *312*, 82–91. <https://doi.org/10.1016/J.CATTOD.2018.03.048>.
- (199) Cheng, Y. L.; Hsieh, C. T.; Ho, Y. S.; Shen, M. H.; Chao, T. H.; Cheng, M. J. Examination of the Brønsted-Evans-Polanyi Relationship for the Hydrogen Evolution Reaction on Transition Metals Based on Constant Electrode Potential Density Functional Theory. *Phys. Chem. Chem. Phys.* **2022**, *24* (4), 2476–2481. <https://doi.org/10.1039/D1CP05723E>.
- (200) Kroese, D. P.; Brereton, T.; Taimre, T.; Botev, Z. I. Why the Monte Carlo Method Is so Important Today. *Wiley Interdiscip. Rev. Comput. Stat.* **2014**, *6* (6), 386–392. <https://doi.org/10.1002/WICS.1314>.
- (201) Metropolis, N.; Rosenbluth, A. W.; Rosenbluth, M. N.; Teller, A. H.; Teller, E. Equation of State Calculations by Fast Computing Machines. *J. Chem. Phys.* **1953**, *21* (6), 1087–1092. <https://doi.org/10.1063/1.1699114>.
- (202) Nelson, J.; Chandler, R. E. Random Walk Models of Charge Transfer and Transport in Dye Sensitized Systems. *Coord. Chem. Rev.* **2004**, *248* (13–14), 1181–1194. <https://doi.org/10.1016/J.CCR.2004.04.001>.
- (203) Chun, H. J.; Apaja, V.; Clayborne, A.; Honkala, K.; Greeley, J. Atomistic Insights into Nitrogen-Cycle Electrochemistry: A Combined DFT and Kinetic Monte Carlo Analysis of NO Electrochemical Reduction on Pt(100). *ACS Catal.* **2017**, *7* (6), 3869–3882. https://doi.org/10.1021/ACSCATAL.7B00547/ASSET/IMAGE/S/LARGE/CS-2017-005479_0008.JPEG.
- (204) Baranovskii, S. D.; Cordes, H.; Hensel, F.; Leising, G. Charge-Carrier Transport in Disordered Organic Solids. *Phys. Rev. B* **2000**, *62* (12), 7934. <https://doi.org/10.1103/PhysRevB.62.7934>.
- (205) Andersen, M.; Plaisance, C. P.; Reuter, K. Assessment of Mean-Field Microkinetic Models for CO Methanation on Stepped Metal Surfaces Using Accelerated Kinetic Monte Carlo. *J. Chem. Phys.* **2017**, *147* (15), 152705. <https://doi.org/10.1063/1.4989511/196772>.
- (206) Liang, T.; Tian, Y.; Dai, Z.; Lenus, S.; Xie, J. Dual In-Plane/out-of-Plane Ni₂P-BP/MoS₂ Mott-Schottky Heterostructure for Highly Efficient Hydrogen Production. *J. Alloys Compd.* **2023**, *965*, 171416. <https://doi.org/10.1016/J.JALLCOM.2023.171416>.
- (207) Shahrokhi, M.; Raybaud, P.; Le Bahers, T. 2D MoO₃-X_S/MoS₂ van Der Waals Assembly: A Tunable Heterojunction with Attractive Properties for Photocatalysis. *ACS Appl. Mater. Interfaces* **2021**, *13* (30), 36465–36474. https://doi.org/10.1021/ACSAMI.1C08200/ASSET/IMAGES/LARGE/AM1C08200_0008.JPEG.
- (208) Laursen, A. B.; Kegnæs, S.; Dahl, S.; Chorkendorff, I. Molybdenum Sulfides—Efficient and Viable Materials for Electro- and Photoelectrocatalytic Hydrogen Evolution. *Energy Environ. Sci.* **2012**, *5* (2), 5577–5591. <https://doi.org/10.1039/C2EE02618J>.
- (209) Roy, K.; Maitra, S.; Ghosh, D.; Kumar, P.; Devi, P. 2D-Heterostructure Assisted Activation of MoS₂ Basal Plane for

- Enhanced Photoelectrochemical Hydrogen Evolution Reaction. *Chem. Eng. J.* **2022**, *435*, 134963. <https://doi.org/10.1016/J.CEJ.2022.134963>. (220)
- Hong, S.; Rhee, C. K.; Sohn, Y. Photoelectrochemical Hydrogen Evolution and CO₂ Reduction over MoS₂/Si and MoSe₂/Si Nanostructures by Combined Photoelectrochemical Deposition and Rapid-Thermal Annealing Process. *Catal. 2019, Vol. 9, Page 494* **2019**, *9* (6), 494. <https://doi.org/10.3390/CATAL9060494>. (221)
- Li, Z.; Jiang, Z.; Zhou, W.; Chen, M.; Su, M.; Luo, X.; Yu, T.; Yuan, C. MoS₂Nanoribbons with a Prolonged Photoresponse Lifetime for Enhanced Visible Light Photoelectrocatalytic Hydrogen Evolution. *Inorg. Chem.* **2021**, *60* (3), 1991–1997. https://doi.org/10.1021/ACS.INORGCHEM.0C03478/ASSET/IMAGES/LARGE/IC0C03478_0005.JPEG. (222)
- Qu, G.; Zhou, Y.; Wu, T.; Zhao, G.; Li, F.; Kang, Y.; Xu, C. Phosphorized MXene-Phase Molybdenum Carbide as an Earth-Abundant Hydrogen Evolution Electrocatalyst. *ACS Appl. Energy Mater.* **2018**, *1* (12), 7206–7212. https://doi.org/10.1021/ACSAEM.8B01642/ASSET/IMAGES/LARGE/AE-2018-01642G_0005.JPEG. (223)
- Le, T. A.; Bui, Q. V.; Tran, M. Q.; Cho, Y.; Hong, Y.; Kawazoe, Y.; Lee, H. Synergistic Effects of Nitrogen Doping on MXene for Enhancement of Hydrogen Evolution Reaction. *ACS Sustain. Chem. Eng.* **2019**, *7* (19), 16879–16888. https://doi.org/10.1021/ACSSUSCHEMENG.9B04470/ASSET/IMAGES/LARGE/SC9B04470_0006.JPEG. (224)
- Ramalingam, V.; Varadhan, P.; Fu, H.-C.; Kim, H.; Zhang, D.; Chen, S.; Song, L.; Ma, D.; Wang, Y.; Alshareef, H. N.; He, J.-H.; Ramalingam, V.; Varadhan, P.; Fu, H.; He, J.; Kim, H.; Alshareef, H. N.; Zhang, D.; Chen, S.; Song, L.; Ma, D.; Wang, Y. Heteroatom-Mediated Interactions between Ruthenium Single Atoms and an MXene Support for Efficient Hydrogen Evolution. *Adv. Mater.* **2019**, *31* (48), 1903841. <https://doi.org/10.1002/ADMA.201903841>. (225)
- Huang, Z.; Cao, S.; Feng, C.; Li, Y.; Liang, Y.; Li, X.; Mei, H.; Fan, W.; Ben Xu, Yuan, S.; Dai, F.; Lu, X.; Hu, S.; Sun, D. Polydopamine Bridging Strategy Enables Pseudomorphic Transformation of Multi-Component MOFs into Ultrasmall NiSe/WS₂@NC Heterojunctions for Enhanced Alkaline Hydrogen Evolution. *Appl. Catal. B Environ.* **2023**, *334*, 122769. <https://doi.org/10.1016/J.APCATB.2023.122769>. (226)
- Qiao, H.; Li, Z.; Liu, F.; Ma, Q.; Ren, X.; Huang, Z.; Liu, H.; Deng, J.; Zhang, Y.; Liu, Y.; Qi, X.; Zhang, H. Au Nanoparticle Modification Induces Charge-Transfer Channels to Enhance the Electrocatalytic Hydrogen Evolution Reaction of InSe Nanosheets. *ACS Appl. Mater. Interfaces* **2022**, *14* (2), 2908–2917. https://doi.org/10.1021/ACSAMI.1C21421/ASSET/IMAGES/LARGE/AM1C21421_0008.JPEG. (227)
- Biroju, R. K.; Pal, S.; Sharma, R.; Giri, P. K.; Narayanan, T. N. Stacking Sequence Dependent Photo-Electrocatalytic Performance of CVD Grown MoS₂/Graphene van Der Waals Solids. *Nanotechnology* **2017**, *28* (8), 085101. <https://doi.org/10.1088/1361-6528/AA565A>. (228)
- Yang, X.; Cheng, J.; Xu, Y.; Li, H.; Tu, W.; Zhou, J. Heterogeneous Ultra-Thin FeCo-LDH@Co(OH)₂ Nanosheets Facilitated Electrons Transfer for Oxygen Evolution Reaction. *Chem. Eng. J.* **2023**, *472*, 145076. <https://doi.org/10.1016/J.CEJ.2023.145076>. (229)
- Tayyebi, A.; Ogino, N.; Hayashi, T.; Komatsu, N. Size-Controlled MoS₂ Nanosheet through Ball Milling Exfoliation: Parameter Optimization, Structural Characterization and Electrocatalytic Application. *Nanotechnology* **2019**, *31* (7), 075704. <https://doi.org/10.1088/1361-6528/AB5077>. (230)
- Rebarchik, M.; Bhandari, S.; Kropp, T.; Mavrikakis, M. Insights into the Oxygen Evolution Reaction on Graphene-Based Single-Atom Catalysts from First-Principles-Informed Microkinetic Modeling. *ACS Catal.* **2023**, *13* (8), 5225–5235. https://doi.org/10.1021/ACSCATAL.3C00474/SUPPL_FILE/C3C00474_SL_002.ZIP. (231)
- Kumaravel, V.; Bartlett, J.; Pillai, S. C. Photoelectrochemical Conversion of Carbon Dioxide (CO₂) into Fuels and Value-Added Products. *ACS Energy Lett.* **2020**, 486–519. https://doi.org/10.1021/ACSENERGYLETT.9B02585/ASSET/IMAGES/MEDIUM/NZ9B02585_M066.GIF. (232)
- Fu, J.; Jiang, K.; Qiu, X.; Yu, J.; Liu, M. Product Selectivity of Photocatalytic CO₂ Reduction Reactions. *Mater. Today* **2020**, *32*, 222–243. <https://doi.org/10.1016/J.MATTOD.2019.06.009>. (233)
- Ferreira de Brito, J.; Corradini, P. G.; Silva, A. B.; Mascaró, L. H. Reduction of CO₂ by Photoelectrochemical Process Using Non-Oxide Two-Dimensional Nanomaterials – A Review. *ChemElectroChem* **2021**, *8* (22), 4305–4320. <https://doi.org/10.1002/CELC.202101030>. (234)
- Zhu, B.; Zhang, L.; Xu, D.; Cheng, B.; Yu, J. Adsorption Investigation of CO₂ on G-C₃N₄ Surface by DFT Calculation. *J. CO₂ Util.* **2017**, *21*, 327–335. <https://doi.org/10.1016/J.JCOU.2017.07.021>. (235)
- Wang, K.; Li, Q.; Liu, B.; Cheng, B.; Ho, W.; Yu, J. Sulfur-Doped g-C₃N₄ with Enhanced Photocatalytic CO₂-Reduction Performance. *Appl. Catal. B Environ.* **2015**, 176–177, 44–52. <https://doi.org/10.1016/J.APCATB.2015.03.045>. (236)
- Hong, S.; Rhee, C. K.; Sohn, Y. Photoelectrochemical Hydrogen Evolution and CO₂ Reduction over MoS₂/Si and MoSe₂/Si Nanostructures by Combined Photoelectrochemical Deposition and Rapid-Thermal Annealing Process. *Catal. 2019, Vol. 9, Page 494* **2019**, *9* (6), 494. <https://doi.org/10.3390/CATAL9060494>. (237)
- Hu, X.; Yang, H.; Gao, M.; Tian, H.; Li, Y.; Liang, Z.; Jian, X. Insights into the Photoassisted Electrocatalytic Reduction of CO₂ over a Two-Dimensional MoS₂ Nanostructure Loaded on SnO₂ Nanoparticles. *ChemElectroChem* **2019**, *6* (12), 3077–3084. <https://doi.org/10.1002/CELC.201900632>. (238)
- IEA. Ammonia Technology Roadmap; Towards More Sustainable Nitrogen Fertilizer Production. *Int. Energy Agency* **2021**, 163p. (239)
- Cui, X.; Tang, C.; Zhang, Q. A Review of Electrocatalytic Reduction of Dinitrogen to Ammonia under Ambient Conditions. *Adv. Energy Mater.* **2018**, *8* (22), 1800369. <https://doi.org/10.1002/AENM.201800369>. (240)
- Shen, H.; Choi, C.; Masa, J.; Li, X.; Qiu, J.; Jung, Y.; Sun, Z. Electrochemical Ammonia Synthesis: Mechanistic Understanding and Catalyst Design. *Chem* **2021**, *7* (7), 1708–1754. <https://doi.org/10.1016/J.CHEMPR.2021.01.009>. (241)
- Li, M.; Huang, H.; Low, J.; Gao, C.; Long, R.; Xiong, Y.; Li, M.; Huang, H.; Low, J.; Gao, C.; Long, R.; Xiong, Y. Recent Progress on Electrocatalyst and Photocatalyst Design for Nitrogen Reduction. *Small Methods* **2019**, *3* (6), 1800388. <https://doi.org/10.1002/SMTD.201800388>. (242)
- Zhang, L.; Ji, X.; Ren, X.; Ma, Y.; Shi, X.; Tian, Z.; Asiri, A. M.; Chen, L.; Tang, B.; Sun, X.; Zhang, L.; Ji, X.; Ren, X.; Sun, X.; Ma, Y.; Shi, X.; Tang, B.; Tian, Z.; Chen, L.; Asiri, A. M. Electrochemical Ammonia Synthesis via Nitrogen Reduction Reaction on a MoS₂ Catalyst: Theoretical and Experimental Studies. *Adv. Mater.* **2018**, *30* (28), 1800191. <https://doi.org/10.1002/ADMA.201800191>. (243)
- Ye, W.; Arif, M.; Fang, X.; Mushtaq, M. A.; Chen, X.; Yan, D. Efficient Photoelectrochemical Route for the Ambient Reduction of N₂ to NH₃ Based on Nanojunctions Assembled from MoS₂ Nanosheets and TiO₂. *ACS Appl. Mater. Interfaces* **2019**, *11* (32), 28809–28817. https://doi.org/10.1021/ACSAMI.9B06596/ASSET/IMAGES/LARGE/AM9B06596_0005.JPEG. (244)
- Azofra, L. M.; Li, N.; Macfarlane, D. R.; Sun, C. Promising Prospects for 2D D₂–D₄ M₃C₂ Transition Metal Carbides (MXenes) in N₂ Capture and Conversion into Ammonia. *Energy Environ. Sci.* **2016**, *9* (8), 2545–2549. <https://doi.org/10.1039/C6EE01800A>. (245)
- Yan, E.; Balgley, R.; Morla, M. B.; Kwon, S.; Musgrave, C. B.; Brunschwig, B. S.; Goddard, W. A.; Lewis, N. S. Experimental and Theoretical Comparison of Potential-Dependent Methylation on Chemically Exfoliated WS₂ and MoS₂. *ACS Appl. Mater. Interfaces* **2022**, *14* (7), 9744–9753. https://doi.org/10.1021/ACSAMI.1C20949/ASSET/IMAGES/MEDIUM/AM1C20949_M001.GIF. (246)

Insert Table of Contents artwork here

